STARS

University of Central Florida
STARS

Electronic Theses and Dissertations, 2004-2019

2010

Fabrication Of Integrated Optofluidic Circuits In Chalcogenide Glass Using Femtosecond Laser Direct Writing

Troy P. Anderson
University of Central Florida

 Part of the Electromagnetics and Photonics Commons, and the Optics Commons
Find similar works at: https://stars.library.ucf.edu/etd
University of Central Florida Libraries http://library.ucf.edu

This Doctoral Dissertation (Open Access) is brought to you for free and open access by STARS. It has been accepted for inclusion in Electronic Theses and Dissertations, 2004-2019 by an authorized administrator of STARS. For more information, please contact STARS@ucf.edu.

STARS Citation

Anderson, Troy P., "Fabrication Of Integrated Optofluidic Circuits In Chalcogenide Glass Using Femtosecond Laser Direct Writing" (2010). *Electronic Theses and Dissertations, 2004-2019*. 1518.
https://stars.library.ucf.edu/etd/1518

FABRICATION OF INTEGRATED OPTOFLUIDIC CIRCUITS IN CHALCOGENIDE GLASS USING FEMTOSECOND LASER DIRECT WRITING

by
TROY P. ANDERSON
B.S. University of Nebraska – Lincoln, 2004
M.S. University of Central Florida, 2007

A dissertation submitted in partial fulfillment of the requirements
for the degree of Doctor of Philosophy
in the College of Optics
at the University of Central Florida
Orlando, Florida

Spring Term
2010

Major Professor: Martin Richardson

© 2010 Troy Anderson

ABSTRACT

Femtosecond laser direct writing (FLDW) is a versatile process that uses focused femtosecond pulses to modify the physical structure of a material, which can result in a shift of optical properties such as the linear and nonlinear refractive index. If the photon energy of the femtosecond pulses lies below the material bandgap, nonlinear absorption rather than linear absorption becomes the dominant mechanism of energy transfer to the material. In this manner, a focused femtosecond pulse train can be used to fabricate functional features such as optical waveguides, diffractive optical elements, or micro-fluidic elements within the volume of a transparent medium. In this dissertation, the utility of femtosecond laser processing as a fabrication technique of optical and micro-fluidic elements in chalcogenide glasses is explored. The photo-induced modifications of optical and chemical parameters of new germanium-based Chalcogenide glasses in both bulk and thin-film form are characterized for the first time and the impact of material composition and laser fabrication parameters are discussed. The glasses are found to display an increase in volume, a decrease of the linear optical refractive index, and an increase of the nonlinear refractive index when exposed to femtosecond laser pulses. A model based on avalanche ionization and multi-photon ionization is used to describe the highly nonlinear absorption of laser light in the material and correlate the photo-induced modifications to the electron density generated during irradiation. The magnitude of the induced photo-modification is shown to be dependent on laser parameters such as laser dose and repetition rate. The fabrication of microfluidic elements through both direct ablation and the preferential etching of photo-modified regions is also explored. Finally, the integration of both optical elements and fluidic elements fabricated by FLDW into a single substrate is discussed.

TABLE OF CONTENTS

LIST OF FIGURES

LIST OF TABLES

CHAPTER 1: INTRODUCTION

Optofluidics is a rapidly developing class of devices in which optical components and fluidic elements are integrated on a single chip using the same components and fabrication techniques. The synthesis of optics and fluidic technology in this manner provides a flexible and powerful platform for advanced *Lab-on-a-chip* or μ-TAS (micro-total analysis) devices [1-4] towards a myriad of applications including cell sorting, chemical analysis, drug synthesis, medical applications, and detection of biological agents [5-21]. Compared to traditional bench-top systems, integrated systems on the micron scale provide several key advantages:

- Specificity: The use of channels and reservoirs with dimensions on the order of microns isolates small sample volumes or sorting of single cells to provide targeted analysis.
- Micro-scale Fluid Dynamics: Fluid flow is laminar as opposed to turbulent as in macro-scale systems, enabling precise control over the mixing of fluids in micro-systems.
- Portability: Small package sizes and integrated functional elements enable complex functionality outside laboratory environments. The fabrication of opto-fluidic sensors allows for field-deployable devices.

To date, the most prevalent fabrication technique for *Lab-on-a-chip* devices is through soft lithography in a flexible polymer such as poly(dimethylsiloxane) (or PDMS) on a glass or silicon substrate [9, 10, 22-26]. A master mold in the desired pattern is filled with PDMS and a curing solution and cured by heat treatment. The resulting PDMS structure, which may have a combination of fluidic channels or optical components (e.g. a waveguide with periodic structures

to form a DFB laser cavity), is then bonded using an oxygen plasma treatment to the stiff substrate material. In this way, both the PDMS and the underlying substrate can be individually fabricated before bonding to create a complex device. The micro-channels for fluid or gas transport are typically rectangular in shape with dimensions on the scale of hundreds of microns in height and width to centimeters in length. This soft lithographic approach has the advantage of reusable molds for easy duplication and can be scaled for high volume production. Furthermore, PDMS provides high optical transparency for visible wavelengths.

However, soft lithography in PDMS is not the ideal solution as it suffers from limited mechanical rigidity and difficulty in fabricating complex 3D structures. The limited mechanical rigidity is caused by two factors. First, the PDMS polymer itself is pliable and becomes distorted under mechanical stress. Second, as the final device is almost always created out of several materials, the strength of this bond will directly impact the maximum pressure and flow rate of an analyte material through the device. While some research groups have used this flexibility to an advantage to mechanically tune the wavelength of a DFB laser for example[27], this property will significantly impact the lifetime of such opto-fluidic devices when used in the field. Because portability is one of the key driving factors for the creation of these integrated devices, this drawback is potentially a fatal flaw in the ultimate usability of the technology. The limitations on potential device geometries due to a lithographic approach are also significant. Although it may be possible to fabricate reasonably complex features through a multi-step lithographic process, this approach is limited.

Femtosecond laser direct writing (FLDW) is a powerful technique for the fabrication of opto-fluidic devices through the modification of optical and physical properties of a substrate material. An intense femtosecond laser pulse is focused into the volume of a material with negligible linear absorption for the laser wavelength. Owing to the ultrashort pulse duration, the irradiance can be made sufficiently high in the focal volume to induce a nonlinear absorption of the laser light and thus interact with the material. These ultrashort pulses interact primarily with the electrons in a material before thermal diffusion can occur, resulting in a highly localized interaction and precision when micro-structuring a material. A schematic of the fabrication process is given in Figure 1.1.

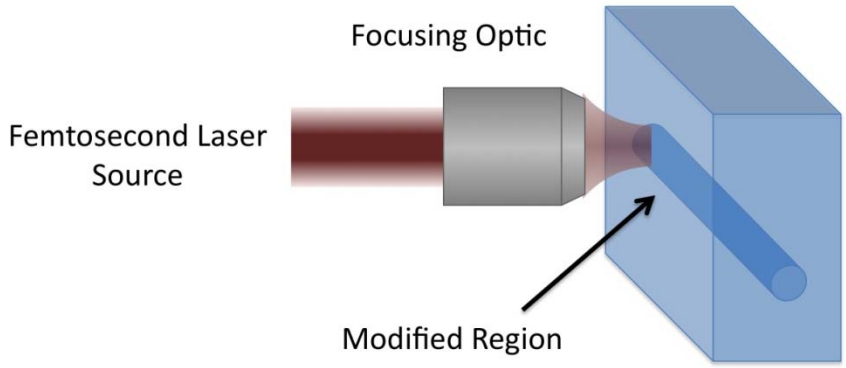

Figure 1.1: Schematic of Femtosecond Direct Laser Writing (FLDW) setup for laser machining

By confining the nonlinear absorption of laser light to the focal region of the laser, the physical size of the modified region is generally on the order of the focal volume of the laser, which is given by the focused spot size of the light through the focusing element in the transverse direction and the confocal parameter (twice the Rayleigh length) in the longitudinal direction as given by

$$Z_R = \frac{2\pi n \omega_0^2}{\lambda} \quad (1)$$

where n is the refractive index of the material, ω_0 is the radius of the focused spot size, and λ is the vacuum wavelength of the laser light. The use of nonlinear absorption in a transparent material bypasses the effects of linear absorption and enables the controlled photo-modification of the entire sample volume of the sample, with the only limitation being the working distance of the focusing element. This allows for the fabrication of complex three-dimensional devices unrealizable through other fabrication methods [28-32]. Devices fabricated through FLDW will be mechanically robust since all the components are directly fabricated in a single piece stable glass material with no joining sites. Additionally, such a device will be more resilient than current multi-material devices to temperature fluctuations that could potentially exist when deployed in the field as there will be no mismatch in thermal expansion or optical refractive index change throughout the device as a function of temperature.

It has been well established that femtosecond laser direct writing can be used to induce photo-modification of material properties in a wide variety of materials including silica [33-39], phosphate glass[40-42], telluride glass [43, 44], crystals[45-50], and chalcogenide glass[51-58]. Associated with a drive to new materials is a fundamental need to understand the photo-structural modification in these materials in response to femtosecond laser irradiation in order to choose appropriate solvents to selectively attack the molecular structure of irradiated regions and thus optimize the fabrication process. Our group has been heavily involved in characterizing this photo-response for many materials including chalcogenides [51, 54, 59-64], oxides[34, 65, 66], and polymers[28]. Of particular interest is the development of this technology for chalcogenide

glasses. Expanding the technology to chalcogenides would enable functionality at infrared wavelengths, which would be particularly useful for the detection of organic agents, many of which have optical absorption bands in the IR. Chalcogenide glasses are highly photo-sensitive [67-69] that makes them particularly suited for femtosecond laser processing. Our prior research into the physical mechanisms of photosensitivity of a wide variety of chalcogenide glasses in response to various irradiation conditions as well as our capability to custom fabricate glass ourselves places us in a unique position in the field.

The aim of this thesis is to advance the state of the art of femtosecond laser materials processing in infrared materials by exploring the photo-induced modification of the optical and chemical properties of Chalcogenide glasses in various forms and compositions towards the fabrication of optical and micro-fluidic structures. The photo-modification of practical properties of the glass including the photo-expansion as well as the linear and nonlinear refractive indices of new germanium-based compositions are explored with an emphasis not only on the values but also the physical structural modifications associated with them. Several studies describe the effect of glass composition or initial bond structure on the ability of the glass to respond to femtosecond laser irradiation. The light-matter interaction is explored through models of the free electron density generated during a femtosecond laser pulse as well as through the use of both low and high repetition rate laser sources to study thermal effects. The application of femtosecond laser processing towards the fabrication of micro-fluidic elements is discussed for the first time to our knowledge with a similar emphasis on optimizing the fabricated features through an understanding of the light-matter interaction and the role of induced thermal effects.

An overview of the state of the art of the use of femtosecond laser processing towards the fabrication of micro-fluidic channels is described. Much of the work to date has been conducted in silicate or crystalline materials and has focused on a two step process of preferential wet chemical etching of photo-modified regions. Chapter 3 provides a theoretical picture of femtosecond laser processing of transparent media including a description of the transfer of energy from the laser to the material through nonlinear absorption as well as the different responses of the absorbed energy. Depending on the nature of the irradiation conditions, it is possible to fabricate a wide array of features in a material ranging from ablated voids to subtle modifications of the optical properties. This is followed by a description of experimental techniques used throughout the thesis to measure the photo-expansion, refractive index, and molecular structure of both bulk and thin-film glasses. The femtosecond laser processing of bulk Chalcogenide glasses is presented in chapter 5. The photo-modification of several germanium-based chalcogenide glass families is studied as a function of material composition as well as an array of laser conditions including repetition rate, laser irradiance, and the number of pulses per focal spot. Chapter 6 expands explores the femtosecond laser photo-modification of thin film Chalcogenide glasses in the same fashion as for the bulk glasses. Thin films are commonly used for integrated optical applications and it is shown that the femtosecond laser photo-response is highly dependent on the bond structure of the glass matrix, which is affected by both the film deposition technique as well as the thermal history of the glass. The use of femtosecond laser processing towards the fabrication of an evanescent-wave opto-fluidic sensor is discussed in chapter 7. The evanescent field of light propagating through an optical waveguide can be exploited as a means to couple optics and fluids integrated into a chip-based device and is the

foundational principle behind many integrated optofluidic sensors. The use of direct ablation as well as preferential etching of photo-modified regions is discussed. Finally, the use of femtosecond laser machining to fabricate both optical and fluidic elements in a single substrate towards opto-fluidic detection is discussed. The results of the work are summarized in chapter 8 and future directions for the fabrication of optofluidic elements in Chalcogenide glasses are suggested.

CHAPTER 2: MICROFLUIDICS BY FEMTOSECOND LASER PROCESSING: STATE OF THE ART

Femtosecond laser processing (FLP) can be used to fabricate microfluidic channels or reservoirs in transparent materials through direct ablation [70], water-assisted ablation[71, 72], or a two-step process whereby wet chemical etching preferentially removes femtosecond laser photo-modified material [73]. To date, the use of FLP for the fabrication microfluidic elements has only been demonstrated in a select few materials including silica, quartz, and sapphire [74-76].

2.1. Microfluidics in Fused Silica by FLP

A surface microchannel can be fabricated by direct ablation of the glass. This technique does not require post-processing and material removal can be easily managed by multiple laser passes or flowing air across the surface during fabrication. As a demonstration, Sun, et al fabricated a curved channel 7μm wide and 16μm deep in borosilicate glass using an 800nm Ti:Sapphire laser operating at a 1kHz repetition rate [70]. The channel was scanned 25 times to remove all of the debris and was then filled with a liquid. The fluidic structure was then used to form a liquid waveguide by filling the channel with liquids with a refractive index higher than silica and propagating 632.8nm light from a He-Ne laser through the liquid. An image of multimode (a) and single mode (b) light emerging from the end facet of the waveguide filled with fluid of refractive index 1.628 (a) and 1.527 (b) are shown in Figure 2.1.

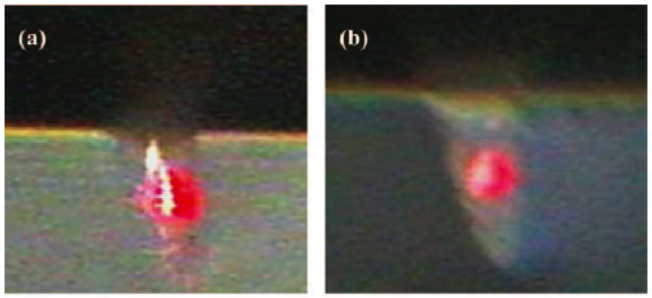

Figure 2.1: Cross section of multimode (a) and a single mode (b) liquid core waveguides in borosilicate glass formed by direct ablation. The refractive index of the liquid was 1.628 in (a) and 1.527 in (b). From Ref [70]

The use of direct ablation in air for the fabrication of fluidic structures is limited to the fabrication of surface features since generated debris inhibits the formation of hollow structures below the surface. However, by immersing the sample in water during ablation, debris can be removed through the formation of bubbles during processing[71, 72, 77, 78]. Using this technique, the laser is first focused on the surface and then moved deeper into the material to create a channel. Once a channel into the bulk of the material has been formed, other elements such as reservoirs can be fabricated. Figure 2.2 shows two examples of this fabrication technique in silica glass: a bent microchannel with a diameter of ~7μm [71] and two stacked reservoirs connected by a channel [72].

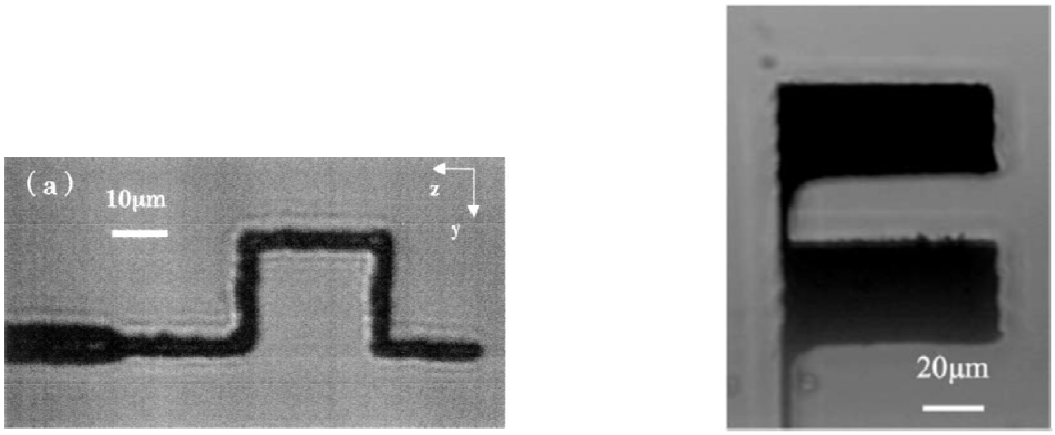

(a) (b)

Figure 2.2: Demonstration of bent channel (a) [71] and serial reservoirs (b) [72] fabricated through water-assisted direct femtosecond ablation.

This fabrication method has been shown to produce features up to a 1mm in length. However, the surface roughness of the channels is on the order of microns as shown in the SEM image of the corner of a buried reservoir (Figure 2.3).

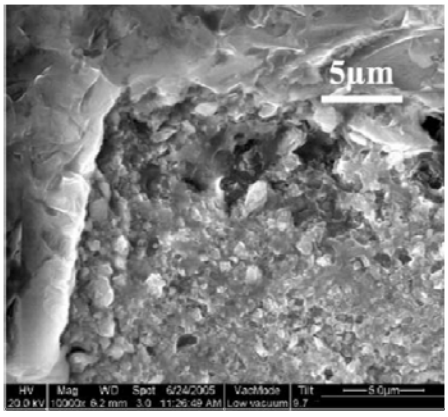

Figure 2.3: SEM image of the corner of a reservoir buried within silica glass indicating micron-sized roughness of the fabricated feature. From Ref [72].

The FLP technique that can produce the smoothest microfluidic features is the preferential etching of laser-modified material. A femtosecond laser with a fluence at or just below the threshold for void formation is used to alter the physical or chemical structure of the transparent

material in the desired pattern. The sample is then immersed in a liquid solvent that preferentially etches the photo-modified region at a higher rate than the untouched material. Oxide glasses tend to react strongly to acidic solutions and thus hydrofluoric acid (HF) is used for the selective etching of microchannels [73]. By avoiding direct ablation, this approach aims to fabricate smooth buried structures by attacking the surface on a molecular level. The primary concern for the optimization of this fabrication technique, then, is to maximize the difference in etch rates between the laser modified material and the unexposed material.

Critical to the optimization of the etch rate of photo-modified regions is an understanding of the chemical and physical modifications of the glass induced by femtosecond laser processing. Below the threshold for ablation or void formation, femtosecond laser irradiation induces an increase in the optical refractive index linked to densification of the material and the formation of color centers[34, 79, 80]. This densification is the result of a decrease of the maximum bond angle distribution in Si-O-Si molecules from 143° to 138° [81] as measured through X-ray scattering and Raman spectroscopy. In addition, femtosecond laser irradiation with fluences near the ablation threshold has been shown to induce the formation of periodic nanostructures in the focal region of the laser with a period on the order of $\lambda/2n$ [37, 82-86]. These structures are oriented perpendicular to the polarization of the writing beam and are comprised of alternating regions of relatively high and low density regions created by a distribution of oxygen [87] in silica glass. The physical mechanism responsible for the formation of these structures is debated and two competing theories are under investigation: an excitation of electron plasma waves that interferes with the incident field [87] and the growth of nano-sheets in the material beginning from material inhomogeneities[84]. A description of these theories of the formation of the

nanostructures is described in section 3.3.2. SEM images of such structures within the volume of fused silica are shown in Figure 2.4. [88] The angle between the beam polarization and the translation direction of the sample, θ, is 90° in (a) and (d), 45° in (b), and 0° in (c). After laser irradiation, the samples were polished to expose the irradiated regions and etched in a 0.5% HF solution for 20 min where the regions of higher density were preferentially etched.

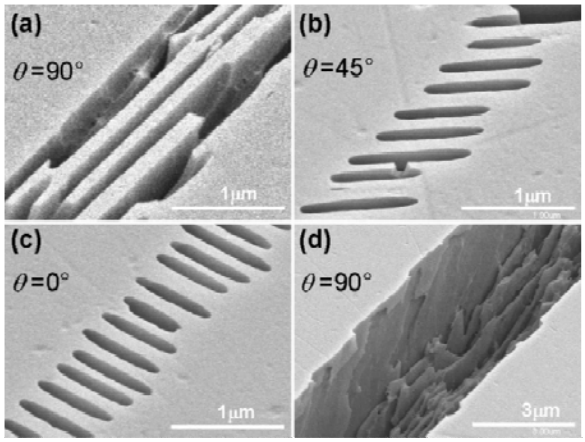

Figure 2.4: SEM images of a single track of fused silica irradiated with 100kHz, 800nm femtosecond pulses with a pulse energy of 300nJ (a-c) and 900nJ (d). The polarization angle relative to the translation direction, θ, is 90° (a and d), 45° (b), and 0° (c). The structures were revealed by polishing the sample to expose the irradiated region and etching in a 0.5% aqueous solution of HF for 20 min. From Ref [88]

This periodic density structure can be exploited for the formation of high-aspect ratio microchannels. When the polarization of the beam is perpendicular to the direction of translation (Figure 2.4a), planes of alternating relatively high and low density material lie along the length of the channel. When the sample is immersed in the solvent, the high density planes are etched out faster than the low density planes allowing for efficient penetration of the acid into the channel.

In addition to the formation of nanostructures in the material, the formation of nanocracks induced by laser fluences above the damage threshold serves to further increase the aspect ratio of fabricated structures [12, 74, 89]. The difference in the structures for making optical waveguides and microchannels is revealed in the optical microscope images presented in Figure 2.5 [74].

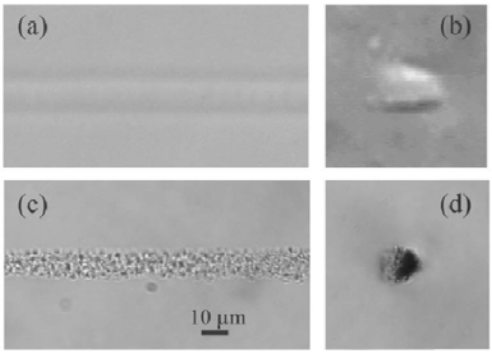

Figure 2.5: Optical microscope images of top (a) and end (b) views of an optical waveguide written with a 20X objective and the top (c) and end (d) views of a microchannel before etching written with a 50X objective From [74]

The figure shows a smooth, gradual change in the refractive index for optical waveguide structures and a rough, damaged track for microchannels that allows for better flow of HF through the track during etching.

The use of an ultrasonic bath during etching has also been shown to increase the aspect ratio of microchannels by as much as a factor of two by facilitating the removal of debris from the channel and moving fresh acid to the channel. This is demonstrated in Figure 2.6 where the third and sixth channels from the top were fabricated with exactly the same parameters except the third channel was etched in still HF while the sixth was placed in an ultrasonic bath during etching [74].

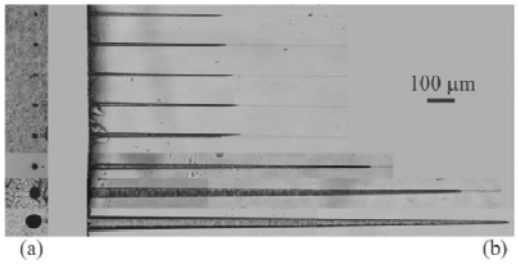

Figure 2.6: Microchannels fabricated in silica glass with different writing parameters. The third and sixth channels were fabricated with the same laser conditions and etched in the same concentration. The sixth channel was etched in an ultrasonic bath, while the third was not, effectively doubling the aspect ratio. From Ref [74]

Femtosecond laser processing can be used to fabricate complex 3D structures within the volume of silica glass. Figure 2.7 shows depicts a series of connected perpendicular microchannels fabricated ~30µm below the surface of fused silica [73].

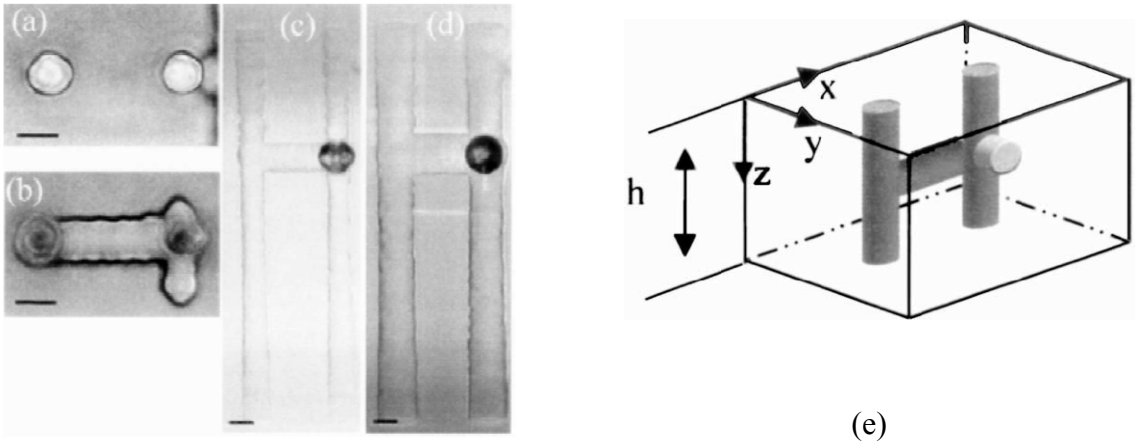

Figure 2.7: Optical transmission images of a microfluidic structure in fused silica after laser irradiation and 2h of development in a 5% HF solution: (a) top view of the entrance plane, (b) top view of the horizontal structures at a depth of 30µm, (c) side view, and (d) side view after 3h of development. The scale bar represents 7µm. A 3D schematic of the structures is shown in (e) for reference. From Ref [73]

This structure was fabricated by 800nm, 120fs pulses with a repetition rate of 1kHz and a laser fluence ~4 times the laser damage threshold. After irradiation, the sample was immersed in a 5% HF solution for 3 hours. Because the pulse energy was significantly higher than the damage threshold, the induced microcracks allowed for rapid exposure of the structure to the HF acid through capillary forces and thus enabled the fabrication of a high aspect ratio structure. The fabricated microchannels had a diameter of 10-12μm and had a surface roughness of ~1μm.

The laser parameters needed to modify the physical and chemical properties of fused silica are of considerable interest for the optimization of the microchannel fabrication process. Table 2.1 lists the laser irradiation parameters and the etching conditions for the fabrication of microchannels.Nearly all of the demonstrations have used an 800nm Ti:Sapphire laser operating at 1kHz for the material modification phase and a weak solution <5% of aqueous HF for the etching phase. Furthermore, nearly all of them have pulse durations at or above the damage threshold, thus exploiting the induced microcracks to provide higher surface area in the modified regions during the etching phase. The striking similarity between the conditions used by all of the groups suggests that the process is relatively optimized for this laser type and etchant combination in this material.

Table 2.1: Laser parameters for microchannel fabrication

Description	Wavelength (nm)	Pulse energy	Rep. Rate	Pulse Duration	Numerical Aperture	HF Concentration	Etch Time	Reference
3D buried reservoir in silica with channels to surface for etching	800	75nJ	1kHz		100X	2%HF	2h	[90]
Fluidic Channels on the surface of slide glass	800	1uJ	1kHz	40fs	0.46NA	None	None	[91]
Buried channels 75-210nm below the surface	1045	100-180nJ	1MHz		0.55	1-5%HF	45min	[92]
Buried channels in silica 100-300nm below the surface	800nm	500uJ	1kHz	150fs	0.3 or 0.6NA	20%HF	3hrs	[89]
Microchannels and evaluation of nanostructures in oxide glass	800nm	2.5uJ	10-250kHz	40-500fs	0.45 or .65	0.5%HF or 2.5%HF	3-20min	[93]
Buried channels with circular cross sections (200um below the surface)	790nm		1kHz		0.3 or 0.6	10-15%HF		[74]
Buried microchannels and nano-scale gratings	800nm		100kHz	40fs	0.65NA	2.5%HF		[88]
3D buried channels in silica	800nm	14-56TW/cm2	1kHz		100X	5%HF	3hrs	[73]
Ultrafast optofluidic gain switch	800nm	4uJ	1kHz	150fs		20%HF	3hrs	[94]
Fluorescence and electrophoresis by FLDW	800nm	2-5uJ	1kHz	150fs	0.3	Channels Pre-fabricated by other method		[13]

2.2. Microfluidics in Crystals by FLP

Crystalline materials are also potential substrate materials for integrated optofluidic circuits owing to their high intrinsic hardness, stability, and chemical resistance. Although progress has been made, the technique is not as well developed as for silica glass. In silicon, for example, 5μm diameter microchannels have been fabricated through direct ablation using a 250kHz, 800nm femtosecond laser focused by a 0.15NA microscope objective. The formation of such small structures with a large NA objective and above band-gap irradiation is curious, but is believed to be due to a combination of linear and nonlinear absorption processes leading to a microexplosion[95].

Microchannels have also been fabricated in both quartz and sapphire through selective etching of femtosecond laser photo-modified regions. In this technique, the primary physical mechanism of change in crystals is primarily an amorphization of the matrix within the focal volume. This amorphous region is then susceptible to solvents, whereas the un-irradiated crystal remains highly resistant. Taking advantage of an almost 300:1 etch contrast ratio between photo-modified and untouched quartz, a winding microchannel 200μm long was written 50μm below the surface of a bulk sample of quartz (Figure 2.8)[75].

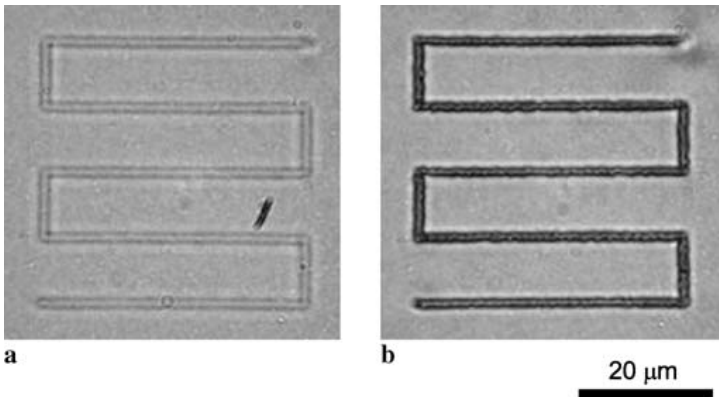

Figure 2.8: Microchannel in quartz buried 50μm beneath the surface with one inlet to the surface. From Ref [75]

This channel was written with ~25nJ pulses at 1kHz from an amplified Ti:Sapphire system and etched in a 5%HF solution for 12 hours. Special care had to be taken to align the crystal axes as the etch rate of quartz is known to be higher for the z-direction.

Sapphire is the hardest and most chemically inert oxide and is thus an ideal substrate for buried fluidic channels. The ratio of the etch rate of irradiated material to un-irradiated material is nearly 10^4, which is sufficiently high that the un-irradiated regions are negligibly affected by etching solvents[96]. The fabrication of both channels and reservoir structures within the volume bulk sapphire have been demonstrated by photo-modification and wet etching in solutions of either hydrofluoric acid or potassium hydroxide. [96] [76, 97-100]. However, although the dissolution contrast is extraordinarily high, features fabricated thus far are not ideal. Removing large volumes of material is difficult as the processing window for proper amorphization is small. As an example, Matsu, et al fabricated "ship-in-a-bottle" rotators in both silica[90] and sapphire[98] using this method. The design of the rotator is shown in Figure 2.9 and consists of a freely rotating fan structure within a reservoir buried within the volume of the

material. Through the application of laser trapping of the rotator, this device can be used as a fluid mixer.

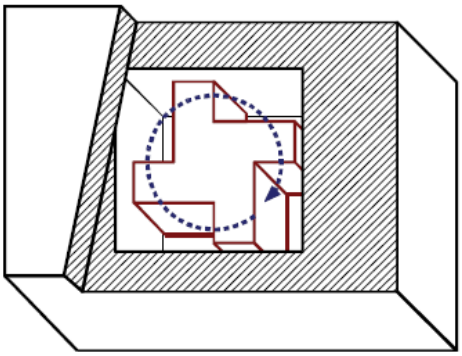

Figure 2.9: Design of a "ship-in-a-bottle" rotator consisting of a freely moving rotator within a buried reservoir. The dotted line represents the direction of motion of the rotator. From Ref [98]

For the device fabricated in sapphire, the rotator did not completely detach from the walls of the reservoir despite the high dissolution contrast. Rather, a mesh structure was formed due to insufficient overlap between adjacent pulses. In silica, this was not an issue and the device functioned as intended. Further work indicated that a reservoir could be completely etched out in HF heated to 120°C, but the surface quality of the fabricated features was compromised indicating an inherent tradeoff between complete amorphization of large areas and the fabrication of low-roughness features.

CHAPTER 3: FEMTOSECOND LASER PROCESSING OF TRANSPARENT MEDIA

The mechanism through which femtosecond laser pulses modify a transparent material can be described by two phases (see Figure 3.1): (1) the excitation of electrons in the material, and (2) the subsequent transfer of energy from the electrons to the lattice[101-103]. A transparent material is considered to have a bandgap energy (E_g) higher than the photon energy ($h\nu$) of the femtosecond laser such that linear absorption is negligible.

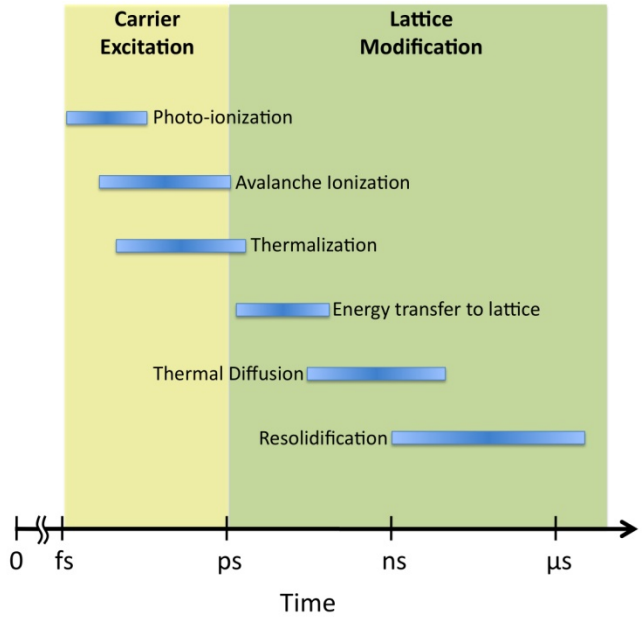

Figure 3.1: Timescale of electron and lattice processes associated with femtosecond laser interaction with a transparent material.

In the first phase, the laser pulse transfers energy to electrons through nonlinear ionization in the form of direct photo-ionization and avalanche ionization, which results in the generation of an free carrier plasma[104]. After the pulse, thermal equilibrium of the plasma is reached by a redistribution of electrons and holes in the valence and conduction bands. This "thermalization"

process occurs on a timescale of hundreds of femtoseconds[102]. In the second phase of the interaction, occurring after about a picosecond, the excited free carrier plasma cools by transferring kinetic energy to the lattice. The increased kinetic energy of the lattice may modify the bond structure of the material and lead to melting or vaporization if the temperature of the lattice exceeds the melting or boiling point of the material. After a nanosecond, the lattice cools by thermal diffusion and resolidifies, a process that can last for microseconds[101, 102]. As the temperature of the lattice cools below the glass transition temperature (T_g), rapid quenching may result in a bond structure different from the initial configuration. In addition, structural modification may occur through non-thermal weakening of the lattice, even when the temperature within the focal region does not reach the melting point. The creation of the free carrier plasma through the absorption of laser photons removes electrons from their bonding orbitals, which results in an increased mobility of the atoms in the lattice.

A unique advantage of femtosecond laser processing relative to longer pulse processing is that the two phases of the (the absorption of laser light and the transfer of energy from the free carrier plasma to the lattice) are decoupled. Since the electron-phonon interactions that transfer kinetic energy to the atoms in the lattice occur on a picosecond timescale, the laser pulse is finished before the lattice begins to heat. This results in minimal thermal heating of material outside of the laser focal region and thus high spatial precision in the micromachining process [105, 106].

3.1. Nonlinear Absorption

3.1.1. Photo-ionization

Photo-ionization is the direct excitation of an electron from the valence band to the conduction of a material. This can occur through multiphoton ionization (MPI) or tunneling ionization. For MPI, bound electrons are ionized through a simultaneous absorption of multiple sub-bandgap-energy photons to reach the ionization energy (E_g). This is shown schematically in Figure 3.2.

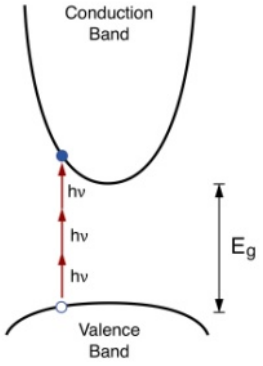

Figure 3.2: Schematic of multiphoton ionization (MPI) in which multiple photons are simultaneously absorbed to ionize an electron.

The number of simultaneously absorbed photons required is the smallest number (n) that fulfills the relation

$$n \cdot h\nu \geq E_g \tag{2}$$

where $h\nu$ is the photon energy [107].

This process produces carrier electrons with an ionization rate of:

$$\frac{dN}{dt} = \sigma_k I^k \tag{3}$$

where N is the number of free electrons, k is the number of photons participating in MPI, σ_k is the k-photon absorption coefficient, and I is the laser intensity [107]. This process is related $I(t)^k$ and is thus most efficient during the peak of the laser pulse.

If the electric field is sufficiently strong to partially suppress the coulomb potential barrier of the electron, the electron can be directly ionized through quantum tunneling[108-110]. An adiabatic parameter, often termed the Keldysh parameter, is generally used to determine the relative contributions of multiphoton ionization and tunneling ionization during laser processing[110, 111]:

$$\gamma = \frac{\omega}{e}\left[\frac{mcn\epsilon_0 E_g}{I}\right]^{1/2} \tag{4}$$

where ω is the laser frequency, I is the intensity of the laser, E_g is the bandgap of the material, m and e are the reduced mass and charge of the electron, c is the speed of light in vacuum, ϵ_0 is the permittivity of free space, and n is the refractive index of the material.

For values of $\gamma < 1.5$, tunneling ionization is the dominant mechanism, whereas multiphoton ionization dominates for $\gamma > 1.5$ [111]. There lies a small range of laser irradiation conditions with $\gamma \approx 1.5$ during which both processes are simultaneously in effect, but this range is narrow and simulations show an abrupt transition between MPI and tunneling ionization[112]. The Keldysh parameters for the experiments in this dissertation range from 3-9 such that multiphoton ionization is the dominant mechanism for direct photo-ionization and equation (3) can be used to

describe the contribution of photo-ionization to the generated free carriers during laser irradiation.

3.1.2. Electron-Avalanche Ionization

Electron-avalanche ionization is a process in which free electrons in the material gain additional energy from the laser pulse through free carrier absorption and impact ionize surrounding atoms to create additional free electrons. A free electron in the conduction band of the material with an energy greater than the bandgap energy $E_0 \geq E_g$ can gain kinetic energy through the absorption of photons from the laser pulse. When the energy of an electron reaches twice the ionization energy of the material, it can ionize a nearby electron in the lattice, resulting in two free electrons in the conduction band of the material [105, 111, 113, 114]. This process is shown schematically in Figure 3.3 and is described by the equation:

$$E = E_0 + nh\nu \geq 2E_g \tag{5}$$

where n is the number and ν is the frequency of the absorbed photons.

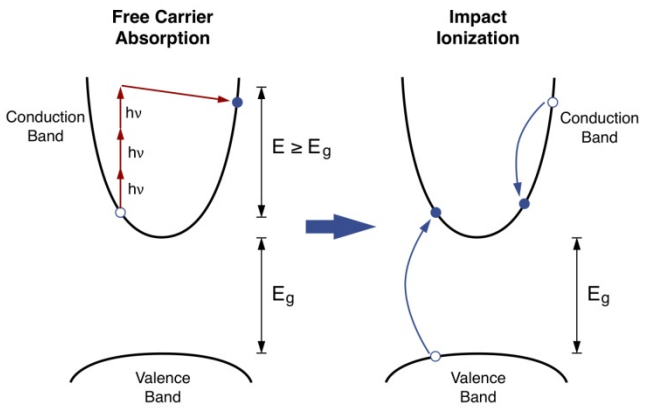

Figure 3.3: Schematics of free carrier absorption and impact ionization processes that lead to electron avalanche ionization

The time scale of this process is on the order of 1 fs [114]. As long as the laser pulse is present, this process repeats and creates an avalanche of free electrons as described by the following rate equation according to Stuart *et al* [105]:

$$\frac{dN}{dt} = \eta I N \tag{6}$$

where η is the avalanche ionization coefficient, I is the laser intensity, and N is the free electron density.

3.1.3. Model of the Generated Electron Density

Electron-avalanche ionization and direct photo-ionization each contribute to the generation of free electrons during laser irradiation. Direct photo-ionization generates free electrons in the material at the beginning of the laser pulse. As the free electron density grows, the contribution of generated electrons through avalanche ionization increases over the duration of the pulse [115]. For pulses less than 150fs, direct photo-ionization is the dominant mechanism as the

avalanche process does not have sufficient time to significantly contribute to the free electron density[116]. Avalanche ionization becomes increasingly significant for pulses of several hundred femtoseconds and is the dominant mechanism for pulses longer than the picosecond timescale [113]. The direct photo-ionization of electrons with femtosecond pulses also plays a critical role in making femtosecond laser processing a deterministic process. When the laser intensity is not high enough to directly ionize electrons, the seed electrons for avalanche ionization arise from thermal ionization of shallow traps due to defects or impurities in the material, which is on the order of 10^8 cm^{-3} for most transparent materials [114]. This corresponds to approximately one free electron within the focal volume of a 0.2NA objective lens, making the photo-response of the material highly sensitive to the local concentration of impurities [105, 107, 114, 117-121].

The total free electron density generated by femtosecond laser irradiation is written as a combination of the rates of avalanche and multiphoton ionization described in equations (3) and (6) along with linear absorption.

$$\frac{\partial N}{\partial t} = \eta I(t) N + \sigma_n I(t)^n \qquad (7)$$

Zoubir *et al* used this model to directly compare the induced electron density to the induced refractive index change in arsenic trisulfide [51]. The writing laser was a 25MHz 800nm Ti:Sapphire oscillator with ~30fs pulses. With 30fs pulses, multiphoton absorption dominates and thus avalanche absorption was neglected. The fit of the data, including a parameter for the saturation of the number of electrons available to participate in the ionization mechanism, is shown in Figure 3.4. In fact, there exists a direct correlation between the induced optical

changes and the induced electron density due to nonlinear ionization. Thus, controlling the nonlinear ionization through irradiation parameters provides a means of control over the modification of the optical and structural properties of the material.

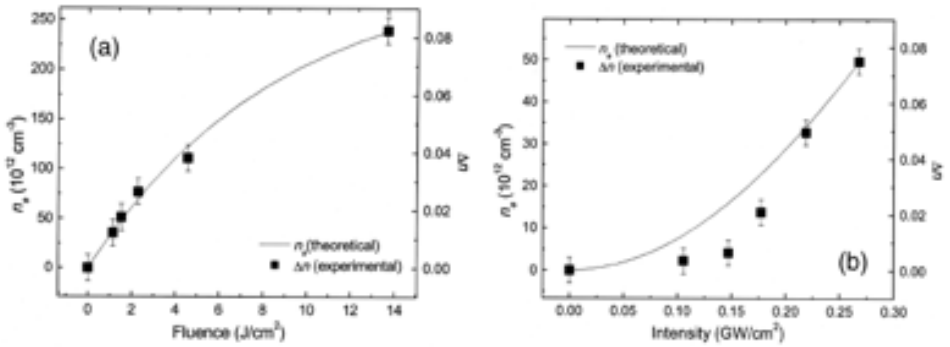

Figure 3.4: Measured Δn and calculated electron density versus (a) the integrated fluence (pulse intensity was set to 0.25GW/cm^2) and (b) the pulse intensity. (From Ref [51])

3.2. Effect of Laser Repetition Rate

The repetition rate of the femtosecond laser pulses during processing affects the degree of cumulative heating of the material by successive laser pulses. As seen in Figure 3.1, thermal diffusion and resolidification of the lattice occur on the timescale of nanoseconds to microseconds after a femtsosecond laser pulse. For low repetition rate processing where the separation between successive laser pulses is longer than this timescale, each pulse interacts with a "cold" lattice that has cooled and resolified after dissipating the energy from the previous pulse (see Figure 3.5(a)).

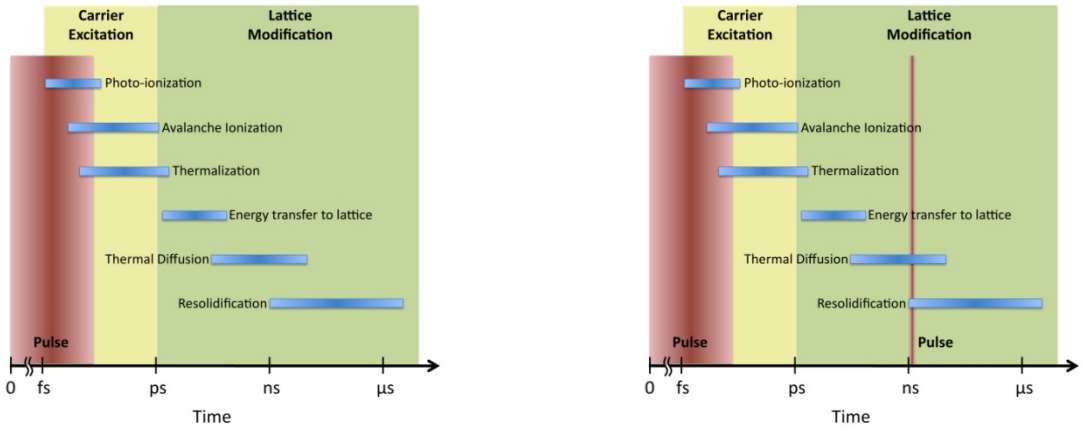

Figure 3.5: Timescale of femtosecond laser processing without (a) and with (b) cumulative thermal effects

If the time between successive pulses is such that the lattice has not reached thermal equilibrium (see Figure 3.5(b)), the lattice temperature builds up over many laser pulses and the lattice does not completely reach thermal equilibrium and resolidify until the train of pulses is finished. The presence of cumulative heating during high repetition rate laser processing influences the irradiance per pulse necessary to modify the lattice. Figure 3.6 depicts the ablation threshold of bulk $As_{36}Sb_6S_{58}$ as a function of the separation between successive laser pulses. The laser source was a 1043nm Yb:YAG fiber laser that produced ~400fs pulses at repetition rates varying from 100kHz to 4MHz (µJewel, IMRA Corp.). The exposure time was 500ms. The laser light was focused onto the surface of the sample using a 0.25NA microscope objective.

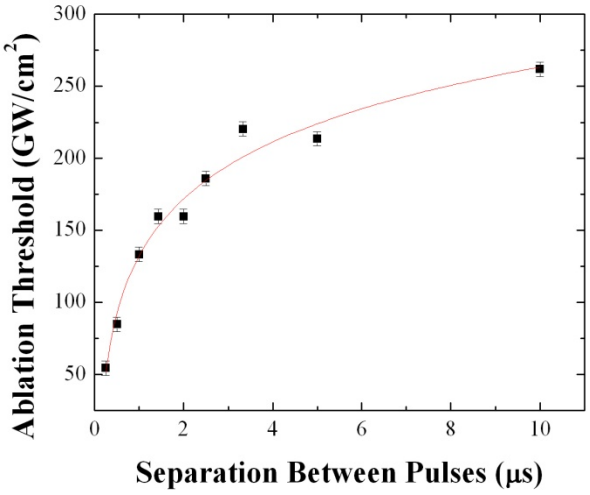

Figure 3.6: Ablation threshold of bulk $As_{36}Sb_6S_{58}$ as a function of the separation between pulses.

The ablation threshold of the glass is used to probe the timescale of lattice effects (thermal diffusion and resolidification) in this arsenic-based chalcogenide glass. The threshold decreases logarithmically with decreasing separation between pulses over the entire range available with this laser, indicating that some degree of cumulative effects are present with repetition rates as low as 100kHz. However, a significant change in the slope of the data occurs around 2μs. The effect of heat accumulation is relatively small (~3% change in ablation threshold per microsecond) for pulse separations greater than about 2μs. When the separation between pulses drops below 2μs, the effect of heat accumulation becomes significant and the irradiance necessary to induce ablation dramatically decreases and the rate of change of the ablation threshold per microsecond of pulse separation rapidly rises above 100%. Thus, thermal diffusion and resolidification of the lattice after are complete about 2μs after a femtosecond laser pulse and the use of lasers with repetition rates higher than ~500kHz will induce significant cumulative effects during laser processing.

The ability to perform precise thermal processing within the volume of a material is a unique to femtosecond laser processing. The use of femtosecond laser pulses enables 3D processing through the absorption of focused sub-bandgap light by nonlinear absorption and the use of high repetition rates induces the thermal effects. In this high repetition rate processing regime, the focal volume of the laser acts as a heat source within the material and the size of the volume of melted material increases with increased exposure [54, 122, 123]. This technique has been utilized for the fabrication of large features and waveguides described throughout this dissertation.

3.3. Material Response Mechanisms

This section describes the physical mechanisms associated with the response of the lattice to the transfer of energy from the hot plasma formed by the absorption of femtosecond laser light.

The response of amorphous materials to femtosecond pulses can be broken down into three regimes depending on the irradiation conditions: void formation, birefringent refractive index modifications, and isotropic refractive index modifications. The following subsections describe each of these cases. The fabrication of microfluidic channels often exploits the birefringent index modification or nanograting structures and high-quality low-loss waveguides are generally formed through an isotropic refractive index change.

3.3.1. Isotropic Index Change

Femtosecond laser processing of glass at low irradiance levels just above the modification threshold induces an isotropic modification of the glass density and optical refractive index and

is the regime most used to fabricate waveguides and other photonic structures such as diffractive optical elements (DOEs). Both the magnitude and the sign of the induced refractive index modification are highly dependent on the material composition and will be affected by the molecular bonds present in the material, the degree of structural order of the lattice, the thermodynamic history of the glass (quenching and annealing), and the relationship between fictive temperature and refractive index of the glass. The physical mechanisms by which the hot plasma generated by the absorption of laser energy modify the lattice can be electronic (an interaction between the hot electron plasma and the molecular bonds in the lattice), thermal (increasing the kinetic energy or temperature of the lattice), or a combination of the two. Electronic interactions are commonly seen in silicate glasses and result in the formation of color centers and non-bridging oxygen hole centers (NBOHCs)[34, 124-126]. Thermal effects occur as a result of heating the lattice above the melting point followed by rapid quenching. The rapid requenching of the glass modifies the fictive temperature of the laser-modified region, which is the temperature at which the structure of the molten liquid glass freezes during quenching. The fictive temperature increases with increased quenching rates and is thus generally increased in the laser modified region relative to the surrounding lattice. In fused silica, an increase in fictive temperature results in an increase in the refractive index, which is consistent with the positive refractive index modification induced by femtosecond laser processing[124]. The opposite has been shown to be true for a commercial phosphate glass, IOG-1 from Schott, which displays a decrease in refractive index for increasing fictive temperatures and a corresponding decrease in the refractive index and density upon femtosecond laser irradiation [41]. The enthalpy of the glass associated with the thermodynamic history of the glass also influences the induced

modifications. It has been shown that in underconstrained Ge-As-Se chalcogenide glass films, photo-contraction was observed for rapidly quenched samples whereas photo-expansion was seen for well-annealed samples [69]. Similarly, the degree of compactness of the lattice will influence the effect of laser processing. Because laser irradiation induces photo-expansion in highly ordered ionic crystals, a measure of the ratio of the density of the glass to the density of the crystalline form of a composition provides a relative measure of the compactness of a glass and can provide insight as to whether a glass will undergo photo-expansion or photo-contraction during processing [67].

A waveguide fabricated in this regime in the volume of As_2S_3 glass is shown in Figure 3.7. The waveguide was fabricated using a ~400 femtosecond pulse laser with a wavelength of 1043nm, a pulse energy of 0.5nJ, and a repetition rate of 1.5MHz (μJewel, IMRA Corp.). The laser was focused using a 0.65NA microscope objective and the sample was translated at 5mm/s through the laser focal volume. Figure 3.7(a) is a DIC microscope image of the waveguide from the top and Figure 3.7(b) is an image of the end facet of the waveguide showing the guiding of 632nm laser light through the structure. A thorough analysis of such structures fabricated in Chalcogenide glasses and their applications to optofluidic structures are described in detail in subsequent chapters.

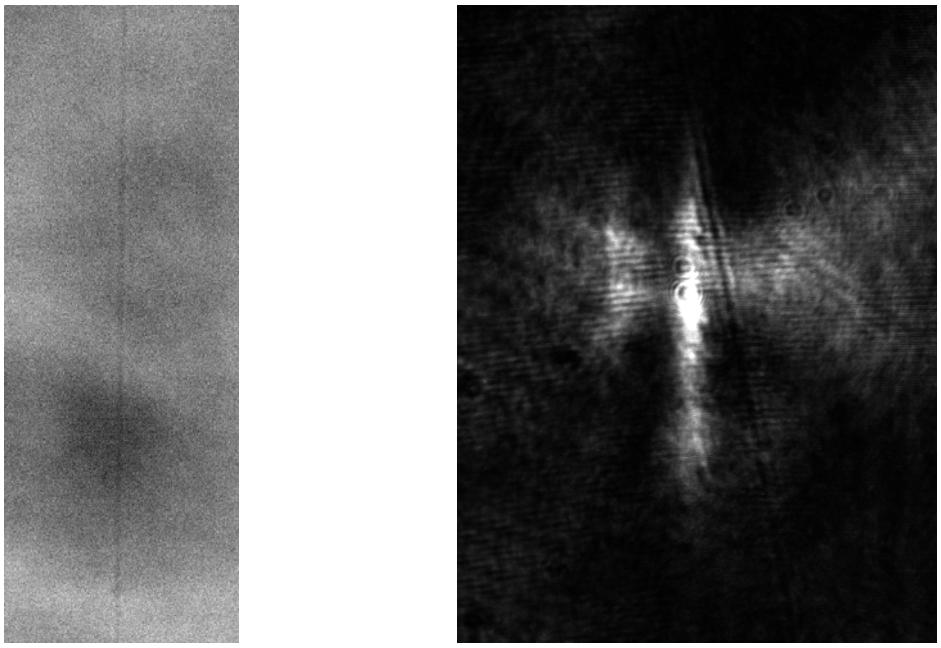

(a) (b)

Figure 3.7: An optical microscope image of a waveguide fabricated in bulk As_2S_3 Chalcogenide glass from the top (a) and of the end facet showing the propagation of 632nm light through the waveguiding structure (b).

3.3.2. Birefringent Index Modification

The second material response regime is characterized by a birefringent refractive index modification. This occurs when the pulse energy is too low for void creation, but the peak power is sufficiently high to induce nonlinear propagation effects such as self-focusing [127]. The birefringence is caused by the formation of a periodic structure of alternating refractive index that forms perpendicular to the laser polarization with a period of roughly where is the wavelength of the writing laser and *n* is the refractive index of the glass. [45, 87, 128-132]. A demonstration of the fabrication of a periodic nanostructure in fused silica by our group using this processing regime is shown in Figure 3.8 [133].

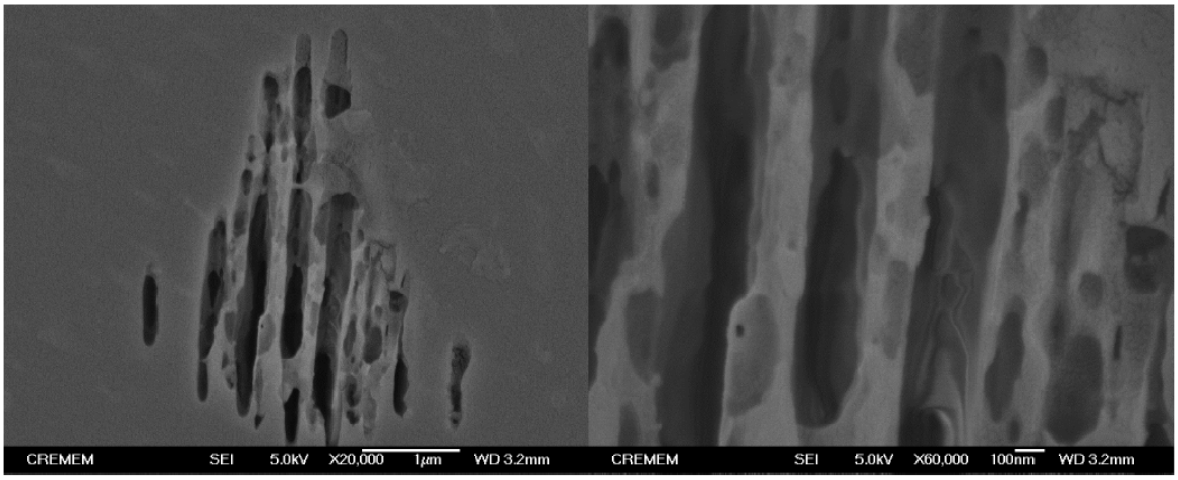

Figure 3.8: SEM image of periodic nanostructure formed beneath the surface of fused silica by femtosecond laser irradiation. The sample was ground and polished to expose the photo-modified region and immersed in a 1%HF solution for 20 minutes to reveal the refractive index profile (from Ref [133]).

The laser used for the modification was a 1043nm Yb:YAG fiber laser (μJewel, IMRA Corp.) that produced ~350fs pulses at a 200kHz repetition rate. A 0.5NA microscope objective was used to focus the laser into the volume of the glass. The pulse energy was 0.7μJ and the spot was irradiated with ~3000 pulses. The periodic structure consists of alternating oxygen-rich and oxygen-deficient regions [87]. In order to view the regions of varying density below the surface of the glass, the sample was ground and polished to expose the laser-irradiated region and then etched in a 1%HF aqueous solution for 20 minutes. Thus, the surface morphology reflected the refractive index profile of the exposed area. The measured period is $360nm \approx \lambda/2n$.

The study of the physical mechanisms leading to the formation of these nanogratings is still under investigation. Shimotsuma *et al* postulated that after a high free electron density is formed through multiphoton absorption during the initial part of the pulse, further absorption of light by the plasma will excite longitudinal plasma waves that interfere with the laser along the direction

of polarization, which would lead to a nanograting perpendicular to the direction of polarization [87]. Bhardwaj *et al*, however, claim that simulations of the plasma temperature ($T_e \sim 10^7$k) and density (1.75×10^{21} cm^{-3}) predicted by this model requires 11μJ pulses whereas the gratings can be formed with as little as 200nJ of energy per pulse [130]. They propose a model based on inhomogeneous breakdown and nanoplasmonics. In this model, randomly distributed nanoplasmas develop into nanosheets over thousands of laser shots. The nanoplasmas arise from inhomogeneous breakdown around defects such as color centers, even in already modified areas. These nanoplasmas naturally form nanosheets arranged with the normal parallel with the laser polarization due to local field enhancements. The long-range order that is maintained as the sample is translated develops from a memory arising from color centers and preferential mode selection similar to plasma based planar metal waveguides. Neither model has been definitively proven at this time.

3.3.3. Void Formation

In the extreme limit of high pulse energies, the shock-like transfer of energy from the plasma to the material lattice results in catastrophic bond breaking and ablation. If the plasma is formed on the surface of the material, this results in the ejection of material and the creation of a crater. Much of the early research in this field was focused on ablative processes with micromachining as the primary application of interest [105-107, 114, 117, 134]. Femtosecond laser processing in this regime has been used for a wide variety of applications including the ablation of metal [106, 135], ultrahard materials [136], non-thermal structuring of biological tissue[137, 138], efficient deep hole drilling [139], photonic crystal fabrication [140], and the creation of surface relief

diffraction gratings in glasses [52]. An example of surface ablation of bulk $As_{42}S_{58}$ Chalcogenide glass towards the fabrication of micro-fluidic channels is shown in Figure 3.9. This ablated feature was formed using 60 femtosecond laser pulses with a Gaussian spatial profile at a wavelength of 800nm, a pulse energy of 0.3nJ, and a repetition rate of 26MHz. The translation speed of the sample through the focal point of the laser was 2mm/s.

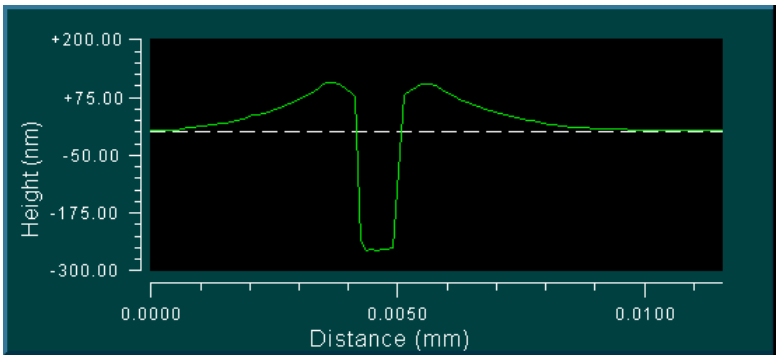

Figure 3.9: Surface Profile of a surface micro-fluidic trench fabricated in bulk As42S58 glass using femtosecond laser irradiation.

In this photo-sensitive glass, the transition between photo-modification of the material and ablation is clearly seen. Only the central region of the Gaussian beam with the highest fluence ablate the material, whereas the wings of the pulse have a lower fluence and cause a photo-expansion associated with an isotropic index change.

If the laser is focused into the bulk of a transparent material, ablation cannot occur, but the high temperatures and pressures created by the plasma eject material from the focal point, resulting in a less dense or even hollow void surrounded by a dense shell. Arrays of voids within the volume of a material such as the 5μm spherical voids pictured in Figure 3.10, fabricated using 120 femtosecond pulses with a wavelength of 800nm pulses and a pulse energy of 1μJ focused by a

1.25NA microscope objective, can be used for applications such as 3D data storage with storage densities up to 0.4GB/cm^3.

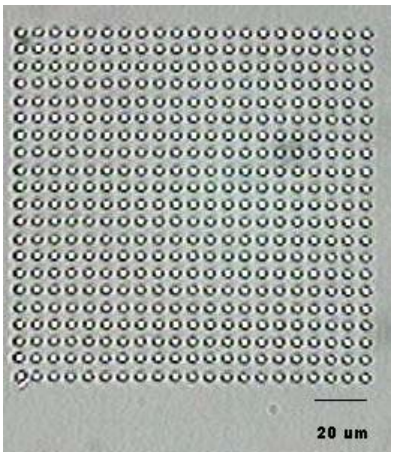

Figure 3.10: Optical microscope image of voids created in the volume of borosilicate glass through femtosecond laser direct writing.

Watanabe *et al* showed that such voids were in the melting phase of the glass and that existing voids could be moved and even merged using a second focused beam [141].

Further increasing the laser energy above the damage threshold of a material results in more catastrophic effects. Schaffer *et al* investigated the formation of voids at pulse energies about 10 times the threshold for damage in borosilicate glass (Corning 0211)[122]. The affected zone had a conical shape that was much larger than the focal region. With such high energies, a plasma can be formed by the leading edge of the pulse before the focal region. This distorts the absorption of the rest of the high intensity pulse and the resulting damage region has a conical shape. This larger photo-modified area decreases the spatial precision of the fabrication technique and reduces the possible storage density.

3.4. Description of Femtosecond Laser Sources

Several femtosecond laser sources are used for experiments described throughout this dissertation in order to study the various material response mechanisms described in the previous section. The following sections describe the laser systems used in the high and low repetition rate irradiation regimes. Repetition rates on the order of MHz are considered to be high repetition rates for the interests of this dissertation and are used to induce thermal heating in the material of interest. Repetition rates on the order of kHz were used for the low repetition rate irradiation experiments described in this dissertation.

3.4.1. Laser Oscillators

Home-built Ti:Sapphire laser oscillators were used as the primary irradiation sources for the characterization of novel chalcogenide glasses to high repetition rate 800nm laser irradiation in this dissertation. A schematic of the home-built Ti:Sapphire laser oscillator is shown in Figure 3.11.

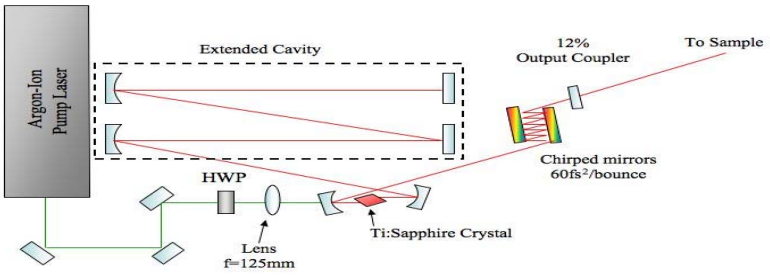

Figure 3.11: Schematic of a home-built Ti:Sapphire laser oscillator used for high repetition rate irradiation.

This laser system consisted of a 4-mm Ti:Sapphire crystal pumped by either an Argon-Ion laser (Spectra Physics) as described in the figure or an ELS Versadisk solid state laser. A photograph of the pump laser and the Ti:Sapphire crystal is shown in Figure 3.12.

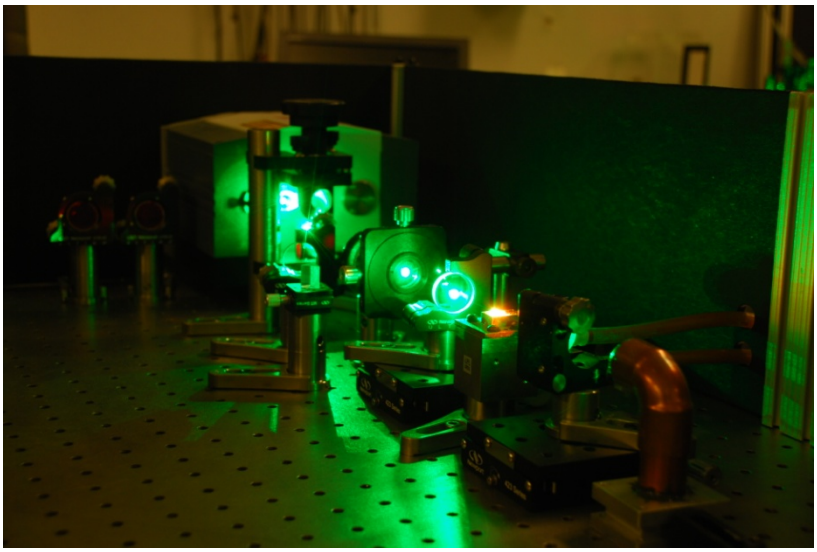

Figure 3.12: Photograph of the pump and cavity of a home-built Ti:Sapphire laser oscillator.

The laser also features an extended-cavity design that enabled control over the laser pulse energy through the modification of the cavity length. The cavity length was controlled using dielectric mirrors arranged in a 1:1 telescope in order to preserve the cavity q and maintain stability. The repetition rate of the oscillator is dependent on the time required for a pulse to travel a round-trip through the cavity and is given through the relation

$$f = \frac{c}{2L} \tag{8}$$

with c as the speed of light and L as the length of the cavity. From this, the pulse energy of the laser, E_p, can be described by:

$$E_p = \frac{P_{avg}}{f} \tag{9}$$

where P_{avg} is the average output power of the laser. The repetition rate of the laser was set to 35MHz and 26MHz in this manner (compared to a ~80MHz repetition rate for non-extended cavities), which provided maximum pulse energies of 8nJ and 11nJ, respectively. Control of the repetition rate was critical as the ablation threshold of the chalcogenide glasses of interest is in this order of magnitude as the maximum pulse energies obtained with this extended cavity laser. The dispersion of the light pulses traveling through the cavity was compensated using a set of intra-cavity chirped mirrors. The dispersion compensation of these mirrors was 60fs per bounce and the dispersion in the cavity was controlled by varying the number of bounces between two mirrors as demonstrated in Figure 3.13.

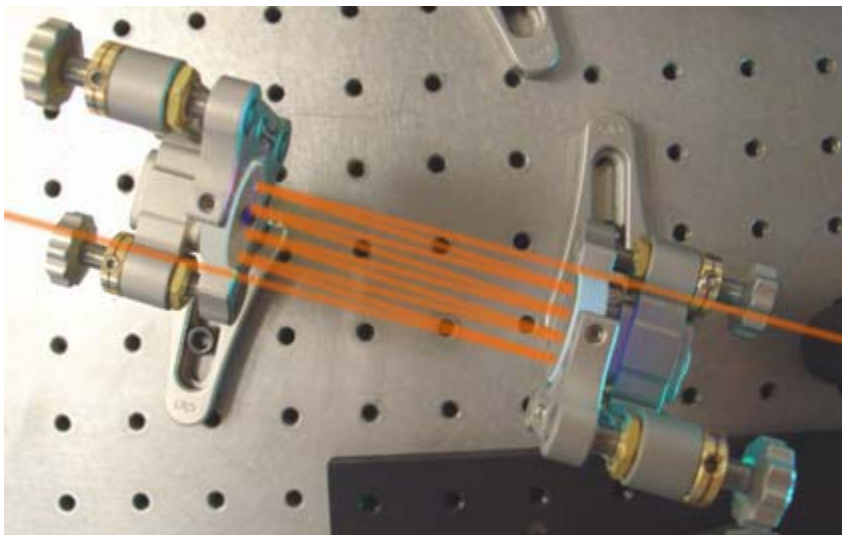

Figure 3.13: Photograph of a set of chirped mirrors used for dispersion compensation. The orange line represents the path of the beam through the mirror combination. From Ref [53].

After dispersion compensation, the pulse length of the laser was ~60fs for both the 35 and 26MHz repetition rate configurations.

In addition to the home-built oscillator, a commercial Ti:Sapphire laser oscillator (KMLabs) was used for several experiments. This laser had a repetition rate of 80MHz and a maximum pulse energy of 3nJ. The pulse length of this laser was set to be ~120fs using a pair of prisms for dispersion compensation. This pulse length was chosen as this laser also served as the seed laser for an amplified laser system (Spitfire, Spectra Physics) described in the next section. This laser was sometimes used for high repetition rate irradiation instead of the home-built systems to compare the high and low repetition rate irradiation regimes with two lasers with similar pulse characteristics (the oscillator seed and the amplified pulse).

3.4.2. CPA-Type Amplified Laser System

The primary laser source used for this type of irradiation was a Spitfire system from Spectra Physics. This laser uses a chirped pulse amplification technique in a Ti:Sapphire regenerative amplifier configuration to produce a train of 1kHz laser pulses at 800nm. In this technique, the seed pulse is positively chirped using a gold diffraction grating before passing into the amplifier in order to decrease the laser intensity, thereby reducing nonlinear effects in the crystal and preventing damage to the crystal or other cavity optics. The amplified pulse is then recompressed using a second diffraction grating. The seed laser for the system is the KML Ti:Sapphire described in the previous section. Together, this system produces 1kHz repetition rate pulses with ~120fs pulse duration and a maximum pulse energy of 1mJ. Because the ablation threshold for chalcogenide glasses is on the order of nJ, the irradiance of the beam is

reduced through ~4% reflections on glass plates. A photograph of the system including the oscillator and the irradiation optics is shown in Figure 3.14.

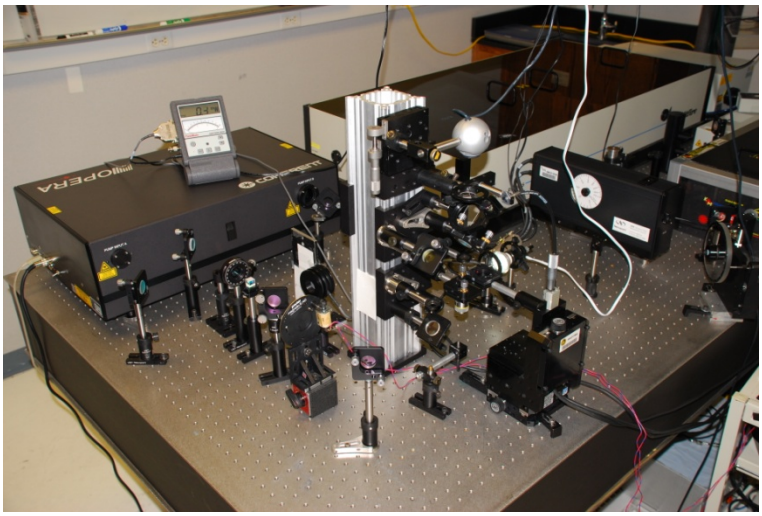

Figure 3.14: Photograph of the Spectra Physics Spitfire amplified Ti:Sapphire laser system used for low repetition rate irradiation

3.4.3. Variable Repetition Rate System

A FCPA μ-Jewel from IMRA Corporation is used to provide 1043nm pulses at a repetition rate that can be adjusted from 100kHz to 5MHz. This fiber CPA system uses a Yb:YAG fiber as the gain medium and an external bulk grating compressor that can be adjusted to optimize the pulse duration for each repetition rate. The pulse duration of the laser ranges from 350fs to 450fs, depending on the repetition rate. This laser is used in this dissertation primarily for the fabrication of micro-fluidic elements in chalcogenide glasses as described in CHAPTER 7. The variable repetition rate in one laser system provided a convenient method for the investigation of the impact of thermal effects on the fabrication of fluidic structures. Although the wavelength of this laser differed from the 800nm Ti:Sapphire wavelength of the other lasers described in this

section, the bandgap of the materials was sufficiently low (<600nm) that nonlinear absorption of the laser light was the primary means of transferring laser energy to the material and the type of photo-induced modifications was the same for both wavelengths. A photograph of this laser system along with the irradiation optics is shown in Figure 3.15.

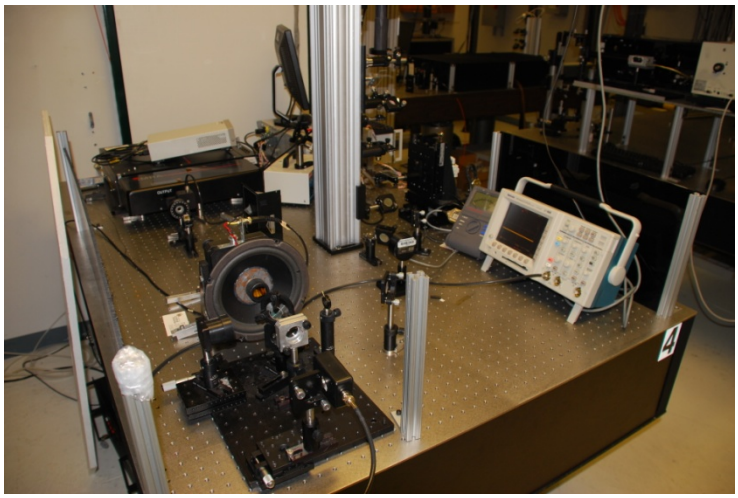

Figure 3.15: Photograph of the IMRA μ-Jewel FCPA laser irradiation facility including a home-built autocorrelator and laser irradiation optics.

3.5. Femtosecond Laser Irradiation Setup

All of the femtosecond laser irradiation experiments described in this dissertation were performed a common an optical irradiation setup, regardless of the laser source used. A schematic of this setup is shown in Figure 3.16.

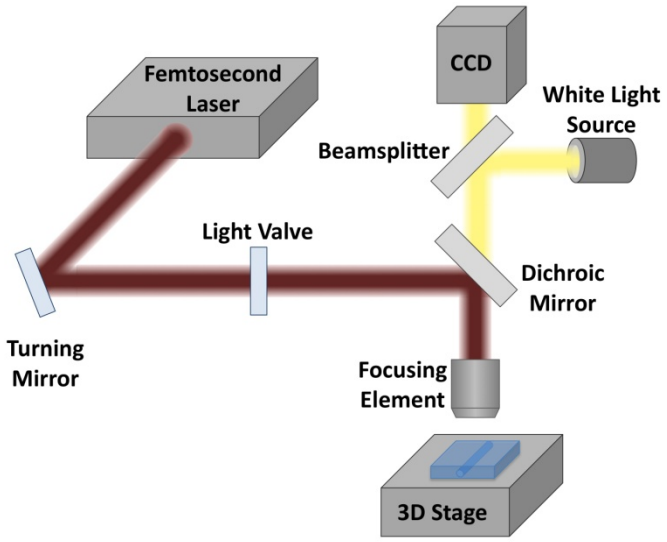

Figure 3.16: Schematic of the femtosecond laser irradiation setup

The sample under test was placed on a 3D translation stage, which could be controlled and programmed by an external computer. Two different stages were used for the experiments: the Newport VP25X and the Aerotech ALS130. Both of these stages provided large travel ranges with sub-micron resolution. The femtosecond laser source was directed onto the sample in a vertical geometry through focusing element. The focusing element was generally a microscope objective and the numerical aperture was chosen for each experiment according to the degree of spatial resolution and working depth desired. The exposure on the sample was controlled by a mechanical shutter, which was also controlled by the external computer such that the exposure of the material could be coordinated with the movements of the translation stage. The laser irradiance was controlled through a light valve consisting of a half-wave plate and a polarizing beam splitter. The focal volume was imaged using the focusing element and a second lens onto a CCD camera such that the irradiation could be monitored in real time. Many of these irradiation

optics were mounted on a vertical tower in order to enable vertical processing and minimize the experimental space.

CHAPTER 4: TECHNIQUES FOR THE ANALYSIS OF FEMTOSECOND LASER MODIFIED REGIONS

This chapter provides a description of the methods to measure the modification of physical geometry, optical refractive index, and the bonds present in the glass matrix induced by femtosecond laser processing. These measurements give insight into the physical mechanisms associated with laser induced modifications in transparent media and allow for the optimization of the femtosecond laser direct write process in the new chalcogenide glass compositions described in this thesis for the first time.

4.1. Surface Geometry: Surface Profile

A measurement of the surface profile of the irradiated region and the surrounding area provides information on how absorbed laser energy affects the material shape as well as the material density. For ablative machining, the surface profile is used to measure the shape of the ablated region, the surface roughness, and the sharpness of the features. The measurement of a surface profile also provides useful information on induced photo-expansion or photo-contraction for non-ablative structuring at laser fluences below the ablation threshold. In this case, measurement of either a photo-expansion or a photo-contraction induced by surface irradiation indicates a decrease or increase in density, respectively. The magnitude of this density modification can then be found by calculating the mass of material within the focal volume and dividing by the volume after irradiation taking into account the photo-expansion or contraction or by the equation:

$$\Delta\rho = \rho_0 \left(\frac{V_0}{V_1} - 1\right) \tag{10}$$

where ρ_0 is the original material density, V_0 is the volume of irradiated material determined by the focusing conditions, and V_1 is the final volume of the irradiated material including the photo-expansion or contraction.

Surface profiles can be taken by either physical contact or contactless methods including atomic force microscopy (AFM), scanning electron microscopy (SEM), or reflection interferometry. Each technique is capable of nanometer-scale resolution of the sample surface profile. Atomic force microscopy is carried out by scanning a nanometer-sized tip across the surface of the sample and measuring the deflection of the tip as it passes along the sample surface. The tip can either be in direct contact with the sample (contact mode) can oscillate near the surface (non-contact mode). The scan speeds of AFM are generally on the order of hundreds of micrometers per second and thus AFM is the slowest of the three methods. Scanning electron microscopy is performed by placing the sample in an evacuated vacuum chamber and sweeping a beam of focused electrons with up to several keV energy across the sample. These electrons then interact with the material through elastic or inelastic scattering. A measurement of the electrons emitted as a result of inelastic scattering is the secondary electron signal and has the highest resolution for surface profile measurements. In order to prevent the buildup of electrostatic charge on the sample, the surface sample must be conductive and grounded. Nonconductive samples are coated with a conductive material such as gold. Reflection interferometry is an optical method in which the sample is placed in an interferometer such that light reflected from the sample surface is interfered with light reflected off a calibrated flat surface. Variations of the optical surface are

translated to a phase shift on an interferogram, which is imaged onto a CCD camera. This technique does not require any sample preparation and can provide surface profiles in within seconds once aligned. However, this method requires optically reflective materials to achieve a sufficient reflection from the sample surface.

Throughout this dissertation, the surface profiles of irradiated glasses are measured by reflection interferometry; specifically, Scanning White Light Interferometry (SWLI) with a Zygo NewView 6300 3D Optical Profiler. The depth resolution of the instrument is 0.1nm through the SWLI technique. This method was used as chalcogenide glasses are sufficiently reflective and the Zygo provides a highly customizable environment for adjusting the field of view and magnification through various combinations of microscope objectives and optical telescopes. In addition, the samples did not require a metal coating and were thus often used for multiple experiments. When using the Zygo, the sample of interest is placed in one arm of a white light interferometer where light reflecting off of the surface of the sample is joined with light from a reference arm to form an interference pattern on a CCD camera. A schematic of the interferometer is shown in Figure 4.1.

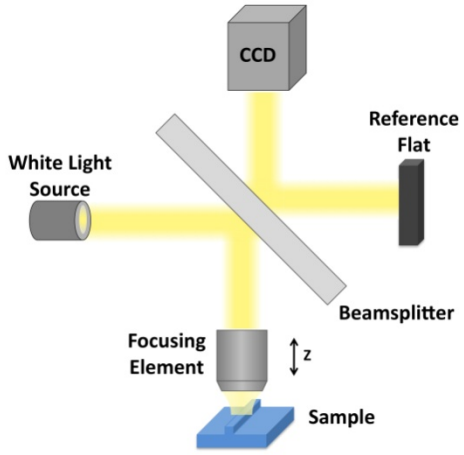

Figure 4.1: Conceptual schematic of white light reflection interferometer for surface profile measurement.

The SWLI measurement is taken by physically scanning the head holding the microscope objective, capturing the images of the interferograms on the CCD as a function of the objective position, and post-processing the images. Spatial resolution is achieved by focusing the white light from the source onto the sample using a microscope objective that also images the sample onto the CCD camera.

4.2. Measurement of Laser-Induced Refractive Index Modifications

4.2.1. Interferometric Methods

A reflection interferometer identical to the one used for surface profile measurements (see Figure 4.1) was used to measure the laser-induced refractive index modifications of thin film chalcogenide glass. A schematic of the sample is shown in Figure 4.2.

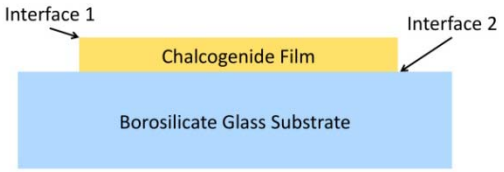

Figure 4.2: Schematic of thin film geometry. Interface 1 lies between the thin film and the surrounding atmosphere and interface 2 lies between the chalcogenide film and the borosilicate substrate.

Light reflected from the interface between the film and the glass substrate (see interface 2 in Figure 4.2) is used to create the interference pattern. In this way, variations of both the refractive index and the thickness of the film are manifested as phase shifts in the constructed interference pattern. The relative phase shift between a laser-irradiated region and un-irradiated material is described by:

$$\frac{\Delta\phi}{2\pi} = \frac{2(n_{irr}d_{irr} - n_0 d_0)}{\lambda} \tag{11}$$

where the subscript *irr* indicates the irradiated material, the subscript *0* indicates un-irradiated material, λ is the wavelength of the light source, n is the refractive index, and d is the film thickness. The factor of 2 on the right side of the equation indicates that the light passes through the film twice. The induced refractive index shift of the irradiated material can be isolated by separate measurements of the film refractive index, thickness, and surface profile before and after irradiation (see section 4.1).

An example interferogram showing the fringe shift associated with a waveguide written in $As_{36}Sb_6S_{58}$ film and imaged onto a CCD camera is shown in Figure 4.3.

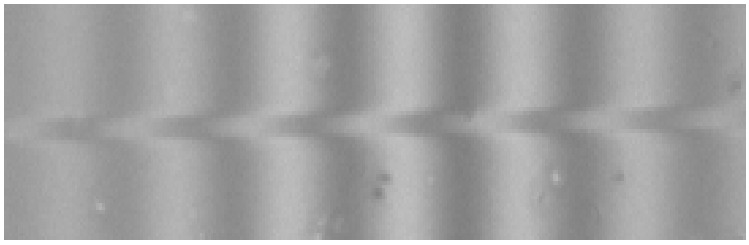

Figure 4.3: Interference pattern showing the photo-induced modification of the optical phase corresponding to a waveguide in thin film $As_{36}Sb_6S_{58}$.

The phase shift, $\Delta\phi/2\pi$, is measured as the ratio of the spatial shift of the interference fringes (in # of pixels) to the period of the fringes (in # of pixels). This is accomplished over the entire image through Fourier Frequency Analysis (FFA)[142-145]. In an interferogram, the intensity of the image can described by the following equation[142]:

$$g(x,y) = a(x,y) + b(x,y)\cos[2\pi f_0 x + \phi(x,y)] \tag{12}$$

where $a(x,y)$ and $b(x,y)$ are unwanted intensity artifacts caused by nonuniform light distribution, f_0, is the spatial frequency of the interference fringes, and $\phi(x,y)$ is the phase signal of interest. The purpose of the FFA algorithm is to isolate this phase signal. It is convenient to rewrite equation (12) as:

$$g(x,y) = a(x,y) + c(x,y)e^{2\pi i f_0 x} + c^* e^{-2\pi i f_0 x} \tag{13}$$

where $c(x,y) = (1/2)b(x,y)e^{i\phi(x,y)}$. Applying a fast fourier transform (FFT) results in:

$$G(f_x, f_y) = \mathcal{F}\{g(x,y)\} = A(f_x, f_y) + C(f_x - f_0, f_y) + C^*(f_x + f_0, f_y) \tag{14}$$

This signal consists of a DC component and two carrier signals located at $\pm f_0$ (see Figure 4.4).

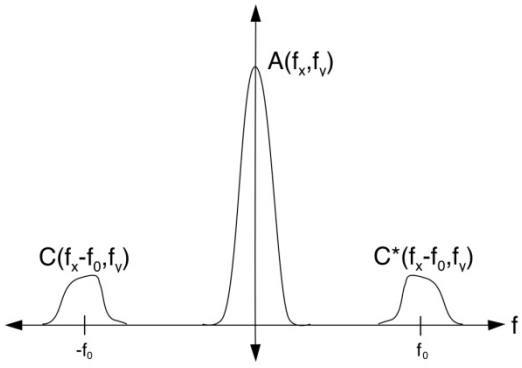

Figure 4.4: Fourier spectra of an interferogram with a DC component and two carrier signals.

The phase information, $\phi(x,y)$, is obtained by isolating one of the two carrier signals, removing the f_0 frequency offset, and taking the angle of inverse FFT.

$$\mathcal{F}^{-1}\{C(f_x,f_y)\} = c(x,y) = \frac{1}{2}b(x,y)e^{i\phi(x,y)} \tag{15}$$

This phase information can then be inserted into equation (11) to determine a spatial profile of laser-induced refractive index modifications. This reflection interferometry technique was used in this dissertation to determine the relative shift of the refractive index induced by femtosecond laser irradiation in several different chalcogenide glass compositions as a function of laser irradiation conditions.

4.2.2. Swanepoel Analysis: Combination Analysis for Thin Films

Swanepoel described a method for determining the refractive index and thickness of a thin film on a substrate material through an analysis of the interference fringes on the transmission spectrum of the films[146]. The application of this method on both laser-irradiated and un-

irradiated sections of a thin film describes the impact of laser irradiation on the film. As an example, Figure 4.5 shows the differing transmission spectra of a $Ge_{28}Sb_7S_{78}$ thin film before and after irradiation by 800nm femtosecond light with a fluence of 94.3 TW/cm^2. The measurement of the spectrum was taken with a Cary 500 from Varian.

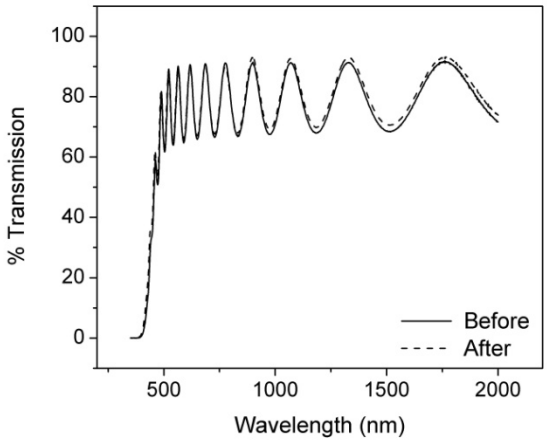

Figure 4.5: Transmission spectra of a $Ge_{23}Sb_7S_{78}$ film before and after femtosecond laser irradiation indicating a modification of the interference fringes.

Considering a thin film on a thick substrate (see Figure 4.2) where n is the refractive index of the film, d is the thickness of the film, and s is the refractive index of the substrate, interference fringes in the transmission spectrum are described by:

$$2nd = m\lambda \tag{16}$$

where λ is the wavelength of light and m is an integer for maxima and a half integer for minima. The envelope containing the maxima of the fringes is given by the transmission spectrum of the substrate in the absence of the film:

$$T_s = \frac{(1-R)^2}{1-R^2} \tag{17}$$

with $R = [(s-1)/(s+1)]^2$.

The envelope function containing the minima of the interference fringes can be written as:

$$T_m = \frac{4n^2 s}{n^4 + n^2(s^2+1) + s} \tag{18}$$

where n is the refractive index of the thin film and s is the refractive index of the substrate on which the film is mounted. This can be arranged to solve for n as:

$$n = \sqrt{M + \sqrt{M^2 - s^2}} \tag{19}$$

with

$$M = \frac{2s}{T_m} - \frac{s^2+1}{2} \tag{20}$$

The power of this technique is that it provides a measurement of the refractive index of the sample across a wide wavelength range and describes the material bandgap. The implementation of this method necessitates a large photo-modified region (on the order of 1mm^2) in order to obtain a measurable signal through a spectrometer. Therefore, it is used as a complimentary method along with the interferometric method described in the previous section, which has excellent spatial resolution but lacks wavelength resolution.

4.2.3. Numerical Aperture Technique

The numerical aperture (NA) of a step-index optical waveguide or fiber (see Figure 4.6), which is related to the maximum angle at which guided exits the output facet of the waveguide, is related only to the refractive indices of the core and cladding of the waveguide. Therefore, if the laser-induced refractive index modification in a transparent medium is a positive shift (a requirement for the guiding of light), then the magnitude of the refractive index modification can be calculated by fabricating an optical waveguide in the sample and measuring the numerical aperture.

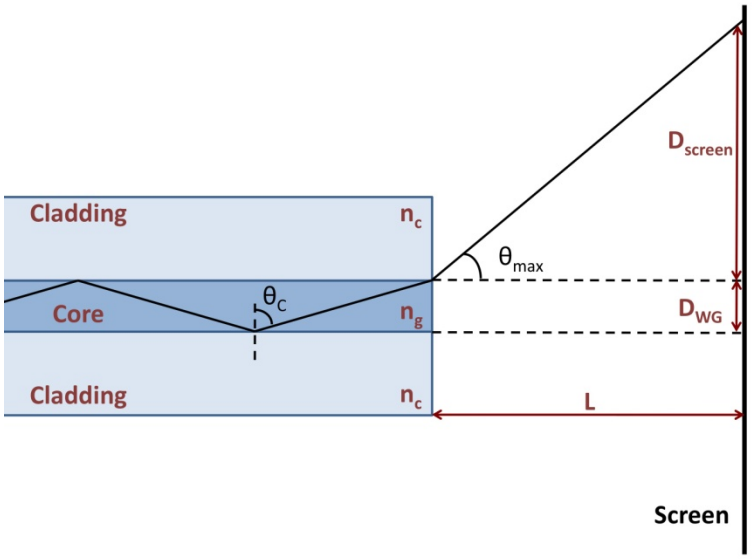

Figure 4.6: Measurement of the numerical aperture of a waveguide.

The half-angle of the emitted cone of light in the far field is measured as:

$$\theta_{\max} = \arctan\left(\frac{D_{screen} - \left(\frac{D_{WG}}{2}\right)}{L}\right) \approx \arctan\left(\frac{D_{screen}}{L}\right). \quad (21)$$

The error associated with the approximation that neglects the size of the waveguide is generally within the error of the measurement since D_{screen} is usually on the order of centimeters and D_{WG} is on the order of micrometers.

The numerical aperture is related to the refractive indices by the relation

$$NA = \sin(\theta_{\max}) = \sqrt{n_g^2 - n_c^2}. \tag{22}$$

The numerical aperture technique for the calculation of laser-induced refractive indices can be applied to both bulk and thin-film samples as long as the induced refractive index is positive and optically smooth input and output facets to the waveguide are available. However, this technique does not provide any spatial resolution of the refractive index profile.

4.2.4. Diffraction Grating Technique

The magnitude of the refractive index modification in a glass induced by femtosecond laser irradiation can be measured by fabricating a series of parallel lines that act as a transmissive diffraction grating and measuring the diffraction efficiency. A schematic of the measurement setup is shown in Figure 4.7.

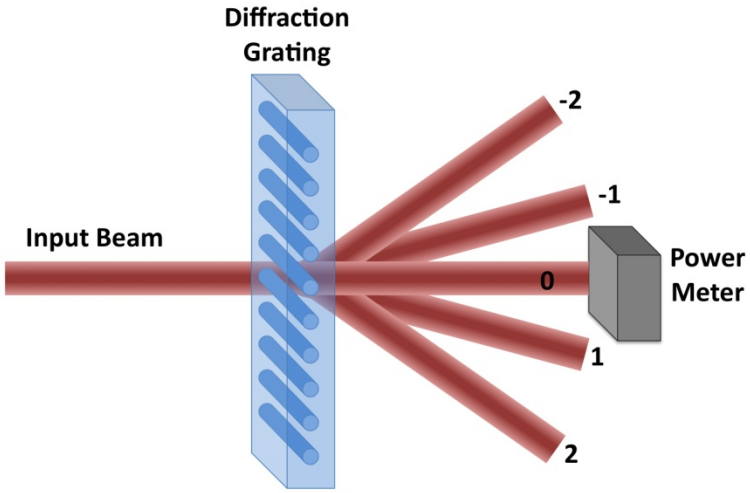

Figure 4.7: Schematic of the measurement of the diffraction efficiency of a laser-fabricated diffraction grating for the measurement of the refractive index.

The first-order diffraction efficiency of the transmission grating, which is the ratio of the power of the first diffracted order to the input power, is related to the refractive index modulation by the formula:

$$\eta_1 = \left(\frac{\Delta n \pi d}{\lambda}\right)^2 + \left(\frac{\Delta \alpha d}{4}\right)^2 \tag{23}$$

where Δn is the periodic refractive index modification, $\Delta \alpha$ is the periodic absorption coefficient modification, and d is the depth of the grating. If the laser-induced modification is isotropic as described in section 3.3.1 and $\Delta \alpha \approx 0$ (no color center formation), then the structure is a phase grating and the second term in equation (23) can be ignored.

This method for the measurement of the diffraction efficiency provides the magnitude of the refractive index modification but does not provide information about the spatial profile of the induced modification or whether it is positive or negative. The measurement technique can be applied to both thin films and bulk materials, but is primarily used for the measurement of sub-surface refractive index modifications where other techniques such as the interferometric and Swanepoel methods described in this chapter do not apply.

4.2.5. Comparison of Methods

Table 4.1 provides a comparison of the capabilities of the refractive index measurements described in this chapter. The measurement techniques are evaluated on whether or not they measure the magnitude and sign of the index modification, if the technique provides spatial resolution of the features, and if the technique can be applied to glasses in bulk or thin film form. No one method is suitable for all tasks and it is often advantageous to apply several methods in combination.

Table 4.1: Comparison of the capabilities of different methods to measure the magnitude and sign of an induced refractive index modification, whether it provides spatial resolution, and whether it is suitable for use on bulk or thin film glass.

Method	Magnitude	Sign	Spatial Resolution	Suitable for Bulk Glass	Suitable for Thin Films
Interferometric	✓	✓	✓		✓
Swanepoel	✓	✓			✓
Numerical Aperture	✓	Must be positive		✓	✓
Diffraction Grating	✓			✓	✓

4.3. Structural Modifications: Raman Spectroscopy

Raman spectroscopy is used throughout this dissertation to investigate the molecular bonds present in the glass matrix by observing their vibrational modes. As chemical bonds between various elements have well-defined vibrational modes, this technique provides a "fingerprint" of the bonds present in the material. A comparison of the Raman spectra of a glass before and after laser irradiation thus provides insight into the modification of the glass matrix as a result of femtosecond laser irradiation. This information can then be used to explain the variations in other observable properties of the glass such as the photo-expansion and refractive index.

Raman scattering is an inelastic process in which the photon energy of the scattered photon is offset by the energy of the excited vibrational mode. An energy band diagram of Raman scattering is shown in Figure 4.8. The pump laser excites the molecules of the material into a virtual energy state. The molecules then relax into vibrational modes and emit a photon as depicted in the figure. Generally, a narrow linewidth laser is used as an excitation source in order to excite all of the molecules to an equal virtual state.

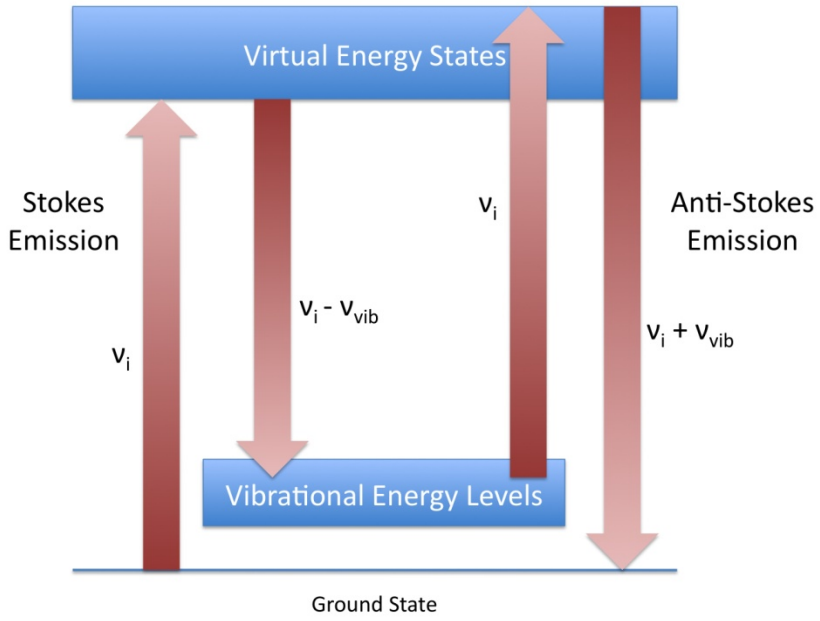

Figure 4.8: Energy band diagram of Raman scattering

The incident pump light interacts with the vibrational modes of the molecules by inducing a dipole, which is expressed as:

$$p = \alpha E_0 \cos(2\pi \nu_i t) \tag{24}$$

where α is the polarizability of the molecule and $E_0 \cos(2\pi \nu_i t)$ is the incident electric field with a frequency ν_i [147]. The polarization of a vibrating molecule is given by

$$\alpha = \alpha_0 + \left(\frac{\partial \alpha}{\partial r}\right) \Delta r \cdot \cos(2\pi \nu_{vib} t) = \alpha_0 + \alpha_{vib} \cos(2\pi \nu_{vib} t) \tag{25}$$

with α_0 the polarizability at equilibrium, Δr is the displacement, and ν_{vib} is the vibrational frequency of the molecule. Combining equations (24) and (25) results in the expression for the dipole of the molecule:

$$p = \alpha_0 E_0 \cos(2\pi \nu_i t) + \frac{\alpha_{vib} E_0}{2} [\cos(2\pi(\nu_i + \nu_{vib})t) + \cos(2\pi(\nu_i - \nu_{vib})t)] \quad (26)$$

The first term describes elastic Rayleigh scattering and the second describes Raman scattering. The Raman term consists of two terms with frequencies, $\nu_i + \nu_{vib}$ and $\nu_i - \nu_{vib}$, which are termed the Anti-Stokes and Stokes signals, respectively. These signals are often written in terms of wavenumbers, which is expressed by:

$$\overline{\nu_{vib}} = \frac{1}{\lambda_{exc}} - \frac{1}{\lambda_{Raman}} \quad (27)$$

The magnitude of the Raman signal is dependent on the vibrational polarizability $\alpha_{vib} = \frac{\partial \alpha}{\partial r} \Delta r$. The term $\frac{\partial \alpha}{\partial r}$ relates to the molecule's change in polarizability during vibration and is a requirement for a Raman scattering signal. Vibrational modes for which this term is nonzero are termed *Raman Active*. Three common Raman-active vibrational modes are symmetric stretching, asymmetric stretching, and bending [148]. Schematics of these modes for linear and nonlinear triatomic molecules are shown in Figure 4.9.

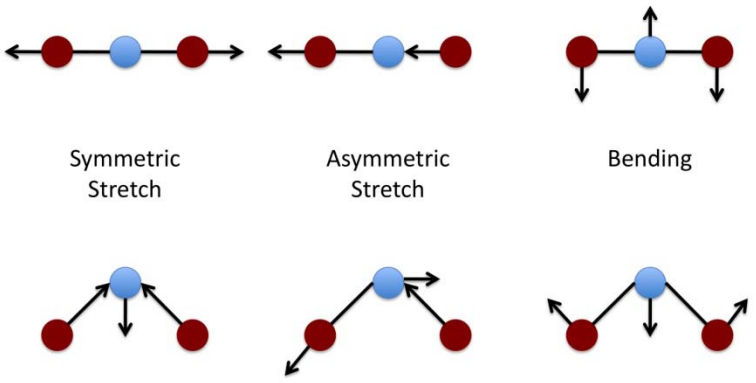

Figure 4.9: Examples of Raman-Active vibrational modes for linear and nonlinear triatomic molecules.

The experimental setup of the Micro-Raman setup used throughout this experiment is shown in Figure 4.10. In micro-Raman spectroscopy, the excitation laser is focused using a microscope objective in order to achieve high spatial resolution of the measurement. The emitted Raman spectrum is then collected with the same objective lens that is used to focus the beam. A notch filter is used to block the excitation laser wavelength and pass the Raman spectrum to the spectrometer.

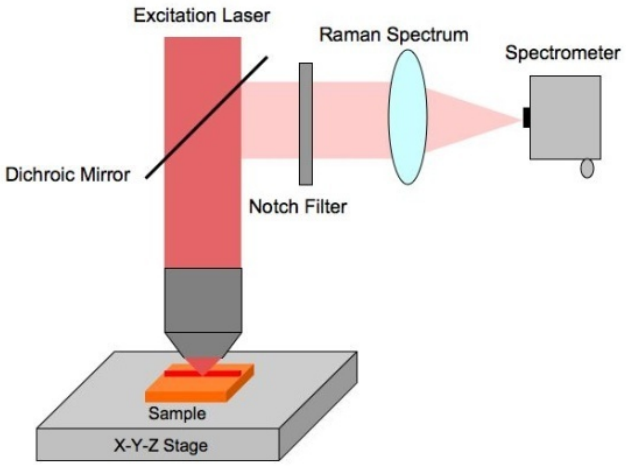

Figure 4.10: Experimental setup for micro-Raman spectroscopy

Throughout this dissertation, Micro-Raman spectroscopy is used to investigate the physical mechanisms associated with the photo-induced modification of chalcogenide glasses. The Raman spectrum of a glass is a composite of the Raman signals from all of the Raman-active vibrational modes present in the glass. In order to analyze and interpret a spectrum, the spectrum is deconvolved into the individual bands located at different vibrational frequencies, which are then correlated to molecular bonds. An example of the deconvolution of a Raman spectrum is shown in Figure 4.11 (from Ref [61]). The glass composition is bulk $Ge_{23}Sb_7S_{70}$. The red line is the measured Raman spectrum and the black peaks are the constituent Raman bands that correspond to Raman signals from vibrational modes in the glass. This spectrum and all of the Raman spectra in this dissertation were deconvolved and correlated to the constituent molecules by Dr. Petit and collaborators at Clemson University. The effect of laser irradiation on the structure of the glass is measured by comparing the Raman spectra of a glass before and after irradiation and noting the changes in the intensity of the Raman bands in the signal.

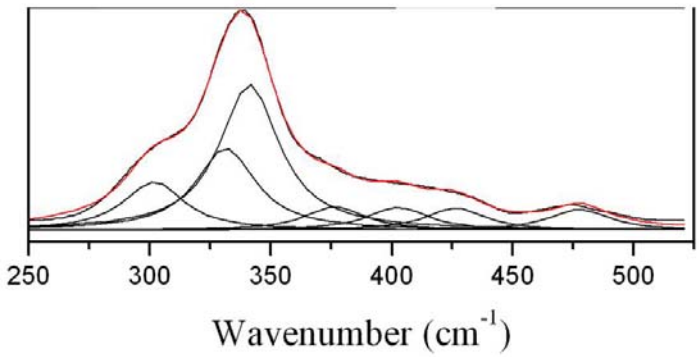

Figure 4.11: Raman spectrum of bulk $Ge_{23}Sb_7S_{70}$ chalcogenide glass deconvolved into the constituent Raman bands associated with molecules in the glass. (From Ref [61])

CHAPTER 5: FEMTOSECOND LASER DIRECT WRITING OF BULK CHALCOGENIDE GLASSES

Initial investigations of non-ablative femtosecond laser processing in glasses revealed that the induced photo-response was dependent on the composition of the glass [35, 36]. This chapter presents the characterization of the photo-response of the bulk forms of two chalcogenide glass families to femtosecond laser irradiation. The glass families, $Ge_{23}Sb_7S_{(70-X)}Se_X$, and $Ge_{18}Ga_5Sb_7S_{(70-X)}Se_X$, are comprised of germanium as the primary glass former with an excess of sulfur and selenium as the chalcogen atoms and a small concentration of antimony to prevent against crystallization. They are of interest as substrate materials for photonics applications including opto-fluidic sensors, active waveguiding elements, and integrated diffractive optical elements that operate in the infrared region of the spectrum. Compared to arsenic-based chalcogenide glasses, such as the well-studied arsenic trisulfide (As_2S_3), germanium-based chalcogenide glasses have a more rigid glass matrix (germanium is a four-coordinated network former) as well as increased melting and transition temperatures [149]. This is the first time that these compositions have been characterized for their photo-response to sub-bandgap femtosecond laser irradiation.

In each of the glass families, the photo-response of the glass is characterized as a function of the relative concentration of the chalcogen atoms: sulfur and selenium. This ratio affects the optical nonlinearity as well as the molecular structure of the glass matrix. Three aspects of the photo-response are characterized, including the photo-expansion, refractive index modification, and the modification of the molecular bonds. This chapter deals specifically with the bulk form of the glass, which is of specific interest for the fabrication of 3D integrated structures within the

volume of the material using femtosecond laser processing.

5.1. Femtosecond Laser Sources

Two femtosecond lasers with different repetition rates were used for the irradiation of bulk Chalcogenide glasses. As described in section 3.2, the relationship between the repetition rate of the laser and the thermal diffusion time of a material is important in determining the role of heat accumulation during processing. The characterization of the response of the chalcogenide glass families in this section in both processing regimes serves to broaden the understanding of the photo-response of these glasses and determine the range of material modification possible using this technique.

The low and high repetition rate pulses were created by the 1kHz CPA-type Ti:sapphire laser (Spitfire, Spectra physics) and the homemade extended-cavity Ti:sapphire oscillator with a repetition rate reduced to 35MHz, respectively. Each of these lasers is discussed in section 3.4.

5.2. Glass Family: $Ge_{23}Sb_7S_{70-x}Se_x$

Germanium-based chalcogenide glasses are of interest as a substrate material as they are known to be highly photosensitive, stable, and exhibit high optical nonlinearities. In addition, selenium-rich chalcogenide glasses are also known for high optical nonlinearities due to the presence of homopolar Se-Se bonds. The investigation of the femtosecond laser photo-response of this family of glasses both broadens the understanding of the influence of linear and nonlinear refractive index on the photosensitivity of the glasses as well as establishes this material family

as a candidate for the fabrication of photonic elements in highly nonlinear materials through femtosecond laser direct writing. Bulk glasses of the system $Ge_{0.23}Sb_{0.07}S_{0.70-x}Se_x$ with x = 0, 0.05, 0.10, 0.20, 0.50 and 0.70 were prepared by collaborators Dr. Richardson and her team at Clemson University from high-purity elements (Ge Aldrich 99.999%, Sb Alpha 99.9%, S Cerac 99.999% and Se Cerac 99.999%)[61]. Elemental dispersive spectroscopy (EDS) was used to verify the elemental compositions of the prepared glasses within the accuracy of the measurement (±2%).

5.2.1. Ablation Threshold

The ablation threshold is defined in this dissertation to be the laser irradiance at which laser irradiation focused on the surface of the sample induces a micro-explosion and ejection of material. It should be noted that the surface ablation threshold of a material is generally lower than the bulk threshold due to surface states caused by contaminants or impurities [150]. However, it is used in this dissertation in order to provide a relative measure of the bond strengths of the glass as a function of composition, to serve as a practical limit for the fabrication of surface structures, and also as a direct comparison between the response of a material in both bulk and thin film forms.

The ablation threshold is investigated by analyzing the response of the material with respect to the energy dose transferred to the material by the laser. The laser is focused onto the surface of the sample using a 10X microscope objective and a mechanical shutter is used to control the exposure time (equivalently, the number of pulses on the sample spot). Using the translation stage, a grid of irradiated points is created in which the number of pulses is varied along one axis

and the laser intensity is varied along the other. In this way, the dependence of the response of the material is characterized as a function of both irradiance and number of pulses. For convenience, this grid is hereafter referred to as a "threshold map".

The threshold map of the x=0 glass in the system using the MHz and kHz repetition rate lasers are shown in Figure 5.1 and Figure 5.2, respectively. Two different techniques are used to analyze the laser irradiated regions of the threshold map: optical microscopy and optical surface profiling. Optical microscopy reveals modifications in refractive index as a discoloration (see Figure 5.1) and optical surface profiling reveals any modification of the density resulting in photo-expansion or photo-contraction (see Figure 5.2). For both techniques, ablation is seen as a black spot in the image caused by the high scattering associated with the loss of material.

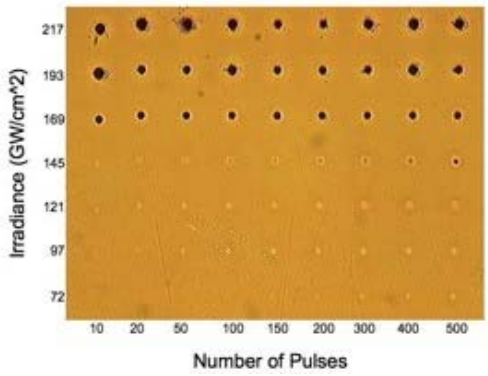

Figure 5.1: Ablation threshold map of bulk $Ge_{0.23}Sb_{0.07}S_{0.70}$ using 80 MHz repetition rate pulses. The image was taken with an optical microscope with 100x magnification [61]

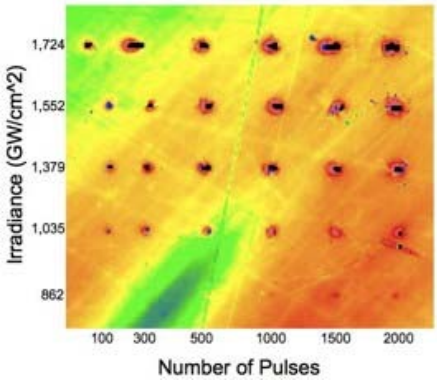

Figure 5.2: Ablation threshold map of bulk $Ge_{23}S_7S_{70}$ using 1 kHz repetition rate pulses taken with a Zygo NewView surface profiler

Two distinct material response regimes are observed: catastrophic ablation resulting in the ejection of material when the irradiance is larger than a certain threshold (termed the ablation threshold) and structural modification at irradiance levels below this threshold. The ablation

threshold has a much stronger dependence on the laser irradiance than the number of pulses incident per spot, which is seen by the invariance of the threshold as the number of pulses is varied by over an order of magnitude. This validates that highly intensity-dependent direct photo-ionization mechanisms discussed in section 3.1 play a dominant role in the absorption of the laser energy and is consistent with the photo-response of arsenic trisulfide, another chalcogenide glass with a bandgap in the visible[51, 54]. The ablation threshold is measured to be~169 GW/cm^2 using 80MHz repetition rate pulses, but is ~1,035 GW/cm^2 when irradiated with 1kHz repetition rate pulses. This factor of ~6.5 between thresholds of the two irradiation regimes indicates that the ablative process is sensitive to cumulative effects induced by high repetition rate radiation. Using kHz irradiation, the energy absorbed by a single pulse must be high enough to induce ablation, whereas the use of high repetition rate pulses induces cumulative thermal effects that induce ablation at relatively lower irradiance values.

The ablation thresholds were determined in this manner for the entire family of glasses as a function of the selenium content in the glass (see Figure 5.3) with the MHz laser as the irradiation source.

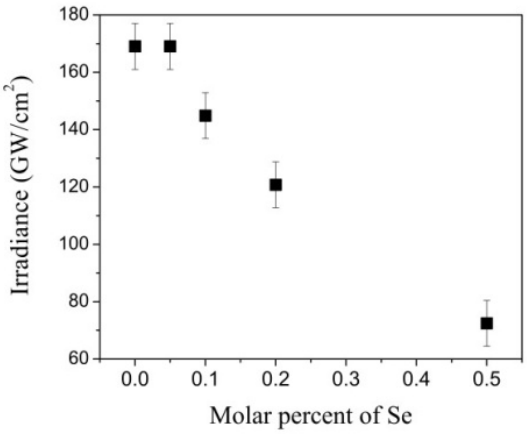

Figure 5.3: Ablation thresholds of $Ge_{0.23}Sb_{0.07}S_{0.7-x}Se_x$ glass family exposed to MHz irradiation as a function of the molar percent of Se [61]

The progressive incorporation of selenium in the germanate sulfide network has a strong impact on the ablation threshold, which shows a decrease in ablation by a factor of ~2 when half of the sulfur content is replaced by selenium. Relative to sulfur, selenium in the glass matrix occupies more space within the glass matrix due to a larger electron cloud and has a lower ionization threshold, which reduces the average bond strengths within the material and leads to a reduction in the laser energy needed to induce ablation [61]. This is seen as a redshift of the optical bandgap of the glasses with increasing selenium content as shown in Figure 5.4. This behavior parallels the response of the As-S-Se glass system [53, 151].

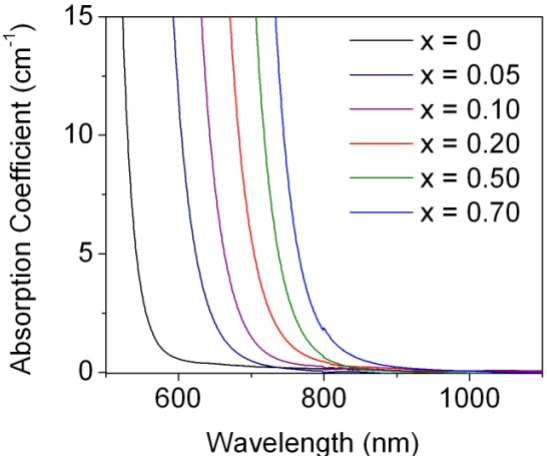

Figure 5.4: Absorption spectra of the $Ge_{0.23}Sb_{0.07}S_{0.7-x}Se_x$ glass family

This redshift of the absorption bandgap affects the value of the linear absorption coefficient at 800nm (see Figure 5.5), which in turn affects the absorption of laser light during irradiation. The generation of free electrons through linear absorption can be modeled by the following rate equation:

$$\frac{dn_e}{dt} = \frac{P(t)(1 - e^{-\alpha z_0})}{h\nu \cdot Az_0} \tag{28}$$

where n_e is the free electron density, $P(t)$ is the power of the laser pulse, α is the linear absorption coefficient, z_0 is the depth of focus (Rayleigh length) in the material, A is the area of the laser focal spot, and ν is the laser frequency. Using this equation combined with the ablation thresholds in Figure 5.3 and the absorption coefficients in Figure 5.5, the free electron density associated with linear absorption leading to ablation was calculated for each material (see Figure 5.6).

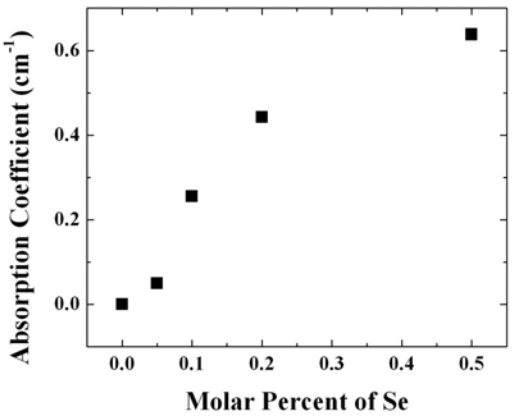

Figure 5.5: Linear absorption coefficient of the $Ge_{0.23}Sb_{0.07}S_{0.7-x}Se_x$ glass family at 800nm.

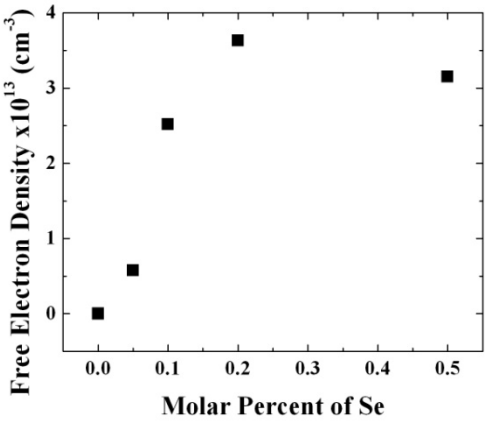

Figure 5.6: Free electron density associated with ablation of the $Ge_{0.23}Sb_{0.07}S_{0.7-x}Se_x$ glass family generated by linear absorption.

The free electron density associated with linear absorption generated during ablation increases with increasing selenium content in the glass. Ablation occurs when the electron density increases to the point where the plasma frequency matches the laser frequency, resulting in high absorption by the plasma[105, 111, 115, 152]. For 800nm light, the critical density is $\sim 10^{21} cm^{-3}$. Because linear absorption is more efficient at generating free electrons than nonlinear mechanisms, the laser irradiance necessary to induce ablation is reduced as the molar percentage of selenium in the glass increases. The observation that the free electron density associated with linear absorption decreases for x=0.5 relative to x=0.2 indicates that the presence of selenium in the glass matrix also increases the nonlinear absorption coefficients of the glass, which reduces the influence of linear absorption.

5.2.2. Photo-expansion

The photo-response of the glasses in this family to irradiance levels below the ablation threshold was characterized by measuring the surface profile of an irradiated area. Photo-expansion has been observed as the result of both continuous-wave and pulsed laser irradiation of arsenic-based chalcogenide glasses [51, 53, 67, 68, 153]. To investigate this phenomenon in this glass family, several 100μm by 100μm square irradiated regions of varying dose (total laser energy per volume) were photo-written on the surface of each sample. The squares were formed by writing a series of parallel lines spaced 2μm apart and the dose was controlled by changing that translation speed of the sample in the range of 10-100μm/s. Chan *et al* used this same technique to create large irradiated regions in fused silica [124]. The laser intensity was set to ~10% below the ablation threshold for each sample in order to obtain comparable results for the samples with varying ablation thresholds. The Zygo NewView 3D Optical Profiler was then used to measure the surface profiles of the photo-written structures. This process was performed using both the MHz and kHz lasers.

No measurable change in surface morphology was seen for irradiation under the ablation threshold with the kHz laser. However, irradiation with the MHz laser induced a dose-dependent photo-expansion of the sulfur-rich compositions on the order of hundreds of nanometers for the glasses with high sulfur content (see Figure 5.7 and Figure 5.8). This dependence of the photo-expansion on the high repetition rate laser suggests that the mechanism for density modification is related to a localized melting and rapid resolidification of the material in which the low density structure of the glass associated with the melting phase is locked in to the glass as it cools as was

proposed by Chan *et al* [154]. As irradiation with 1kHz repetition rate pulses does not induce significant melting of the glass, photo-expansion is not induced.

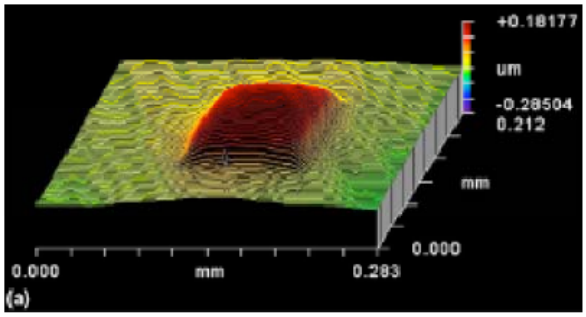

Figure 5.7: Image of photo-expansion for x=10 sample under MHz irradiation (taken with the Zygo NewView 6300 White Light Interferometer) [61]

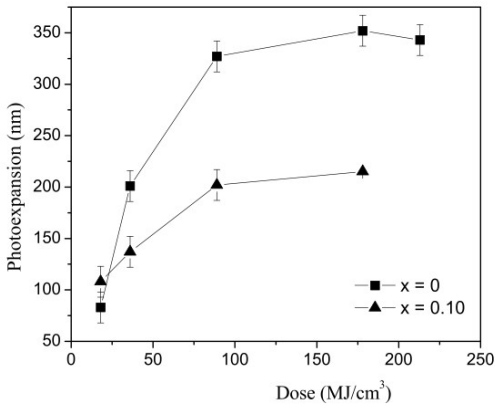

Figure 5.8: Photo-expansion of irradiated squares for x=0 and x=10 glass samples under MHz irradiation. [61]

MHz repetition rate pulses did not induce photo-expansion for all compositions in the glass family, however. The largest photo-expansion, up to 350nm, was seen for the x=0 composition that did not contain any selenium. The incorporation of selenium reduced the induced photo-expansion. The glass with 10% selenium exhibited a maximum photo-expansion of 200nm and no photo-expansion was observed for glasses with more than 20% selenium. The physical mechanisms associated with the photo-expansion are discussed in the next section.

Where photo-expansion is observed, the magnitude increases with increasing dose until a saturation point is reached. The pure sulfide glass exhibits higher photo-expansion than the glass containing selenium. The cause of the saturation is thought to be due to a saturation of the number of electrons available to participate in the ionization processes as seen in arsenic

trisulfide [51]. Additionally, the induced structure itself may distort the focus leading to a reduction of intensity of subsequent pulses and thus saturating the effect. This mechanism was proposed by Schaffer *et al* to explain a saturation of the melt radius of defects in borosilicate glasses induced by MHz irradiation [51].

5.2.3. Micro-Raman Spectroscopy

Micro-Raman spectroscopy was used to characterize the photo-response of the glasses to femtosecond laser irradiation on the molecular scale and explain the physical mechanisms associated with the photo-expansion of the glass. The Raman spectra presented in this section were measured and analyzed by Dr. Richardson and collaborators at Clemson University [61]. The experimental setup is described in section 0. The excitation wavelength was 752nm, which was chosen to be far enough in the IR for minimal absorption and material modification during the measurement.

5.2.3.1 Composition: $Ge_{0.23}Sb_{0.07}S_{0.70}$

Micro-Raman spectra were taken on the 100μm square photo-expanded areas described in the previous section. Figure 5.9 shows the spectra for the pure sulfide glass, the composition with the largest photo-expansion, as a function of laser dose.

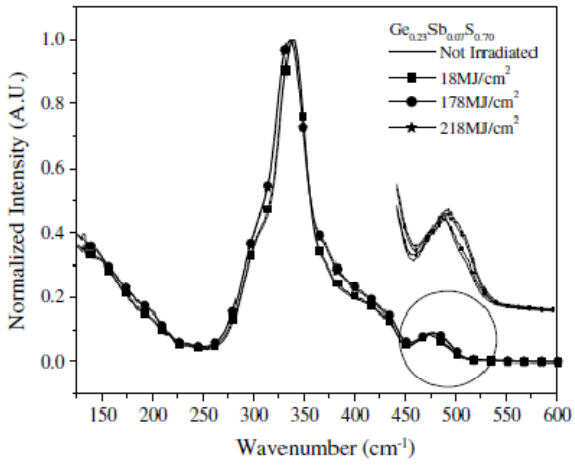

Figure 5.9: Micro-Raman spectra of $Ge_{23}Sb_7S_{70}$ glass as a function of laser dose.[61]

Laser irradiation causes the main Raman band to broaden and shift to lower wavenumbers. The smaller band around 425cm^{-1} also increases slightly as the irradiation dose increases. These large bands forming the spectra are comprised of the overlapping Raman signals of the molecules in the glass matrix. A deconvolution of these spectra (see section 0) by Dr. Petit and collaborators at Clemson University reveals the relative variations of the primary Raman bands associated with the spectra (see Table 5.1).

Table 5.1: Relative strengths of five Raman bands in $Ge_{23}Sb_7S_{70}$ as a function of laser dose.

Dose (MJ/cm^3)	Band at 300 cm^{-1}	Band at 330 cm^{-1}	Band at 340 cm^{-1}	Band at 375 cm^{-1}	Band at 400 cm^{-1}	Band at 425 cm^{-1}
0	13	26	44	6	6	5
18	14	28	40	7	6	5
178	15	38	26	10	6	5
218	15	39	25	10	6	5

Irradiation with increasing dose is seen to produce a decrease of the band at 340cm^{-1} and a corresponding increase of bands at 330cm^{-1} and 375cm^{-1}, which suggests a modification of the

connectivity of the GeS_4 tetrahedra, which include mainly corner shared units, to include units with S-S chains. This can be described as:

$$GeS_4 + GeS_4 \rightarrow \text{-Ge-S-S-Ge-}$$

where the –Ge-S-S-Ge- units are also referred to as $GeS_{4/2}$. In addition, the increase of the band at 475cm^{-1} seen in the figure can be described by some GeS_4 units connecting through edge sharing sulfur bonds:

$$GeS_4 + GeS_4 \rightarrow Ge_2S_{6/2} + S_2$$

Thus, femtosecond laser irradiation induces a structural reorganization of the glass bond-structure characterized by the modification of the bonding forms of GeS_4 tetrahedra, resulting in an increase in the number of $GeS_{4/2}$ and $Ge_2S_{6/2}$ units with increasing laser dose. Irradiation does not induce the formation of homopolar Ge-Ge bonds, which would be seen as a Raman band at 260cm^{-1}. This indicates a distinction from the photo-response of another commonly studied Chalcogenide glass, As_2S_3, which is characterized by the formation of homopolar bonds [54].

5.2.3.2 Composition:$Ge_{0.23}Sb_{0.07}S_{0.60}Se_{0.10}$

A similar process was repeated with the X=10 glass, which contains 10% selenium in the place of sulfur. The Micro-Raman spectra as a function of laser dose are shown in Figure 5.10.

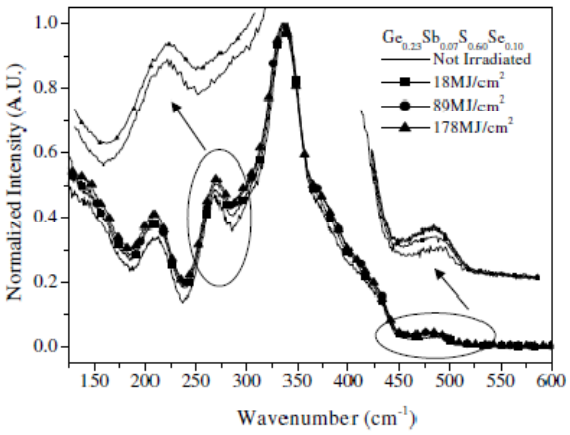

Figure 5.10: Micro-Raman spectra of $Ge_{23}Sb_7S_{60}Se_{10}$ glass as a function of laser dose. [61]

The presence of selenium in the glass significantly alters the Raman spectrum of the glass for both irradiated and un-irradiated regions. Specifically, several bands exist in the range of 200-270cm^{-1} that are not present in the X=0 glass that does not contain selenium. This is due to the presence of $GeSe_4$ tetrahedral units at 200cm^{-1}, Se chains and rings around 260cm^{-1} as well as other mixed units. Additionally, the bands at 375cm^{-1} and 425cm^{-1} is larger, which indicates a larger number of edge-sharing Ge/S units.

Upon irradiation, many of the same modifications as seen in the X=0 glass occur (see Figure 5.9), including a decrease of the Raman band at 340cm^{-1}, the corresponding increase of bands at 330cm^{-1} and 375cm^{-1}, and an increase of the band at 475cm^{-1}. However, the magnitude of these induced shifts is lower in the selenium-containing glass. The most significant shifts are in the 200-270cm^{-1} range containing the Se-rich species.

5.2.4. Effect of Selenium on the Photo-Response

It is thought that the presence of selenium, a relatively large atom with a weaker ionization potential, in the glass network results in a more open structure that is more susceptible to subtle bond distortions rather than the complete breaking and reformation of bonds. This results in a decreased magnitude of the photo-response of the glass relative to the selenium-free (x=0) glass, which was observed in Figure 5.8 as decreased photo-expansion. The incorporation of higher concentrations of selenium into the glass resulted in even more subtle changes in the bond structures upon irradiation and no observable photo-expansion.

Specifically important to this dissertation is the impact of these Raman observations on the photo-response of these glasses to femtosecond laser irradiation. The incorporation of selenium into this chalcogenide glass family creates a more optically nonlinear glass, which could potentially be exploited for optical switching or soliton propagation applications. However, as has been shown here, the incorporation of selenium also significantly reduces the ability for femtosecond laser pulses to create substantial modifications of the bond structure of the glass, making it unsuitable as a substrate material for the fabrication of photonic or fluidic circuits using femtosecond laser direct writing. The base material of this family, $Ge_{23}Sb_7S_{70}$, did display a large photo-expansion and a significant modification in the glass matrix according to Raman spectroscopy and is a suitable candidate for use with femtosecond laser processing.

5.3. Glass Family: $Ge_{18}Ga_5Sb_7S_{70-x}Se_x$

In a method similar to that described in section 5.2, the photo-response of the glass family $Ge_{18}Ga_5Sb_7S_{70-x}Se_x$ to femtosecond laser irradiation was characterized. This glass matrix with the addition of gallium is a potential candidate for active waveguides and waveguide laser applications involving the incorporation of active elements such as erbium into the glass matrix. It is the intent of this study to determine the effect of the incorporation of 5% gallium in the place of germanium on the photo-response of this glass family to femtosecond laser irradiation. .

5.3.1. Ablation Threshold

The surface ablation threshold of the glass family was measured as a function of both the laser irradiance and the number of pulses by irradiating a series of laser spots with varying laser parameters and measuring the surface profile of the irradiated regions with a Zygo NewView 6300 3D Optical Profiler. Ablation was identified by a crater indicating ejected material. Similar to the $Ge_{23}Sb_7S_{70-X}Se_X$ glass family, the ablation threshold was significantly more sensitive to changes in irradiance rather than the number of pulses in both MHz and kHz repetition rate irradiation regimes. In fact, there was a distinctly observable sharp transition between catastrophic ablation and sub-ablation photo-modification as a function of irradiance, whereas the number of pulses did not have any observable impact on the ablation threshold within several orders of magnitude considered here: 10-2000 pulses for 1kHz irradiation and $3.5x10^5$ – $175x10^6$ pulses for 35MHz. Plots of the dependence of this ablation threshold as a function of the molar percentage of selenium content are shown in Figure 5.11 for 1kHz (a) and 35MHz (b) laser repetition rates, respectively.

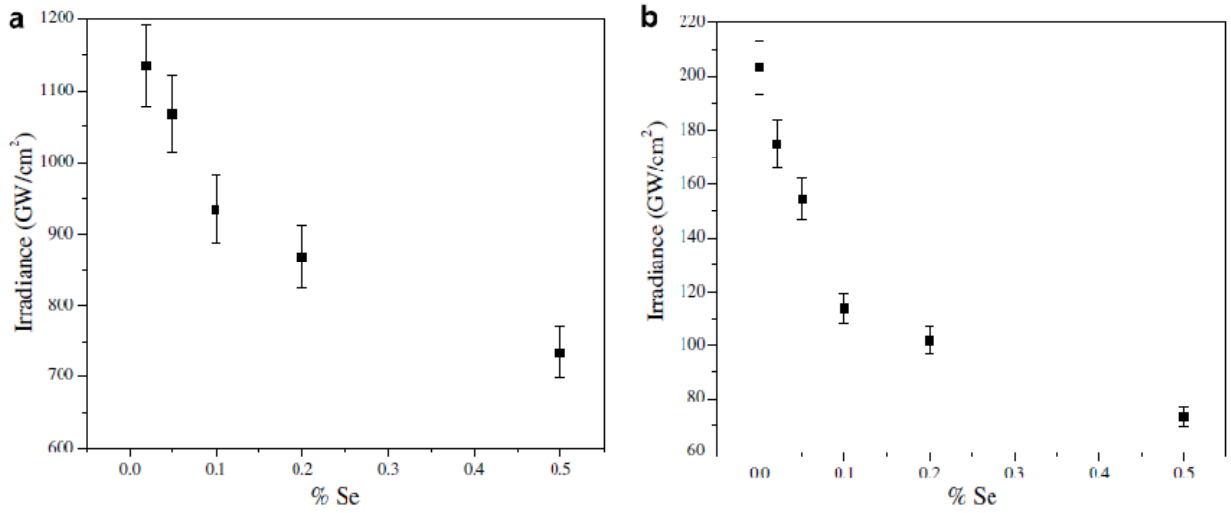

Figure 5.11: Ablation Threshold of GeGaSbS Glass using kHz (a) and MHz (b) irradiation [62]

The ablation threshold of this glass family is larger (~10% and ~20% for the kHz and MHz lasers, respectively) than the ablation threshold for the gallium-free glass discussed in section 5.2, suggesting that the bond dissociation energy for these glasses is increased through the incorporation of gallium. Otherwise, the photo-responses of these glass families are similar. The ablation threshold were roughly an order of magnitude lower for 35MHz irradiation relative to 1kHz irradiation under otherwise identical irradiation conditions, which confirms the presence of cumulative thermal effects that reduce the energy per pulse required to induce ablation for high repetition rate processing. The substitution of selenium for sulfur into the glass matrix results in a progressive decrease of the ablation threshold of the glass regardless of the laser repetition rate. In fact, the substitution of 50% selenium in place of sulfur leads to a reduction of the kHz ablation threshold by 35% and the MHz ablation threshold by 58%. The relatively large dependence of the MHz ablation threshold on the sulfur/selenium ratio suggests that the incorporation of selenium increases the susceptibility of the glass to thermal effects associated

with high repetition rate irradiation. Associated with the reduction of the ablation threshold is a progressive redshift of the optical bandgap of the glass family with increasing selenium content. Using the approach described in section 5.2.1, the portion of the free electron density associated with ablation that is generated by linear absorption was calculated for each of the glasses and is shown in Figure 5.12 for kHz (a) and MHz (b) irradiation.

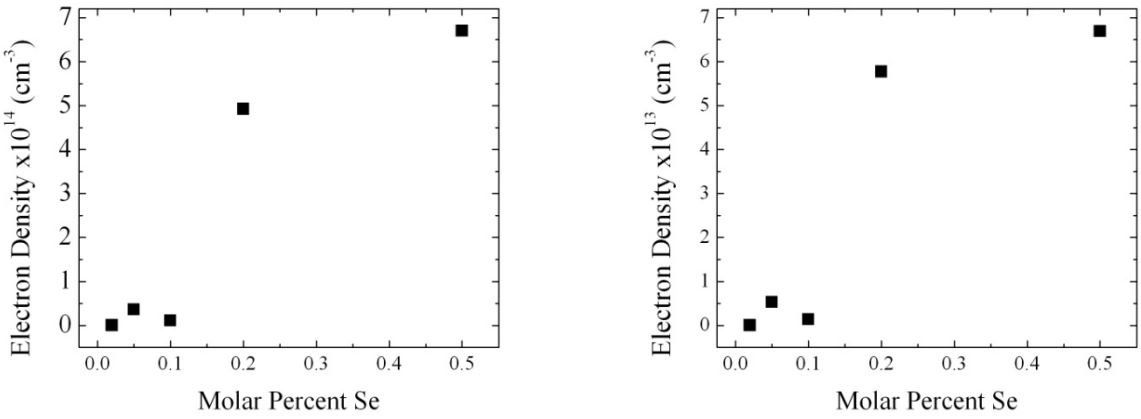

(a) (b)

Figure 5.12: Free electron density associated with linear absorption for 1kHz (a) and 35MHz (b) repetition rate laser ablation.

An increase of the linear absorption coefficient at 800nm with increasing selenium content leads to an increased proportion of the free electron density created by this process. Although the magnitude of the electron density generated through linear absorption is several orders of magnitude smaller than the critical electron density associated with ablation (~10^{21} cm^{-3}), the number of electrons produced by nonlinear mechanisms is reduced and the total irradiance of the beam required to initiate ablation is reduced.

5.3.2. Photo-expansion

The photo-expansion of the glass family as a function of laser dose on the sample was measured using the Zygo NewView 6300 Optical Profiler. The irradiation procedure was the same as described in section 5.2.2. The femtosecond laser was focused onto the surface of the glass using a 0.25NA (10X) microscope objective lens and 100µm x 100µm squares were fabricated by writing a series of parallel lines separated by 2µm. The laser irradiance was set to ~90% of the ablation threshold for each glass so that the relative photo-expansion of the glasses as a function of composition could be compared. The dose was controlled through the translation speed and four squares with speeds of 10, 20, 50, and 100µm/s were fabricated on each sample. The resulting photo-expansion for the X=0 and X=2 glass compositions are compared to $Ge_{23}Sb_7S_{70}$ in Figure 5.13.

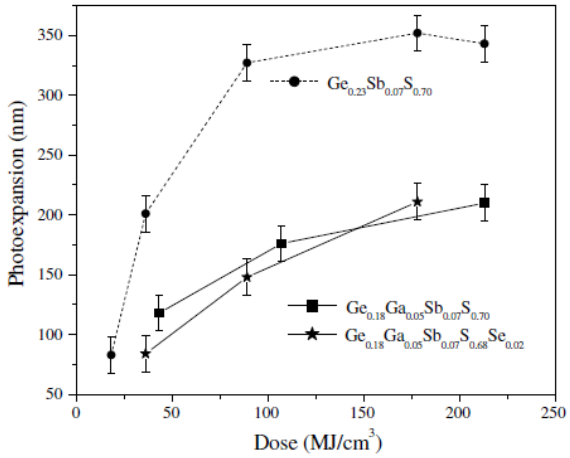

Figure 5.13:Photoexpansion of GeGaSbS Glasses as a function of laser dose [62]

The incorporation of 5% gallium into the glass matrix in the place of germanium does not affect the trend of the photo-modification of the glass to femtosecond laser irradiation. The glass

exhibits a photo-expansion that increases with increasing dose and saturates at around 200nm at a dose of 176MJ/cm^2. However, the incorporation of gallium decreased the magnitude of the photo-expansion~43% relative to $Ge_{23}Sb_7S_{70}$. It is thought that the presence of gallium in the glass matrix results in the formation of GaS_4 tetrahedral units that inhibit the reformation of bonding structures in the glass that gives rise to photo-expansion. This will be discussed further in the next section.

5.3.3. Micro-Raman Spectroscopy

Micro-Raman spectroscopy was used to further understand the mechanisms of photosensitivity of these glasses. The Micro-Raman spectra presented here were measured and analyzed by Dr. Richardson and collaborators at Clemson University [62]. In this dissertation, the material changes that are induced by femtosecond laser irradiation and the resulting impact of these changes on the usability of this glass system as a substrate material for femtosecond laser direct write processing are of interest and will be discussed.

The Micro-Raman spectra of the X=0 glass (the selenium-free glass) as a function of the femtosecond laser dose is presented in

Figure 5.14.

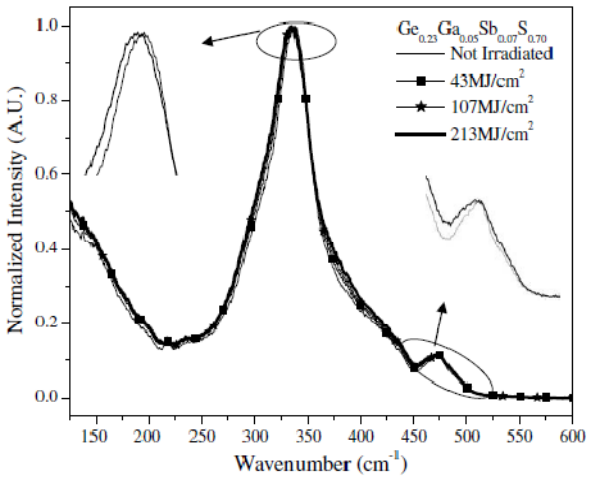

Figure 5.14:Micro-Raman spectra of x=0 glass as a function of laser dose. [62]

Femtosecond laser irradiation is shown to modify the Raman structure of the glass by inducing a shift of the main peak to lower wavenumbers accompanied by a slight broadening of this main band. This is similar to the response of the gallium-free glass described in section 5.2.3 and is attributed to an increase of the connectivity between GeS_4 tetrahedral units and a corresponding increase of homopolar S-S bonds in rings. The absence of a new peak at 260cm^{-1} indicates that laser irradiation does not induce the formation of any homopolar Ge-Ge bonds, unlike arsenic-based glasses. It should be noted that any Raman bands associated with Ga-based units will be very similar to the Ge-based units [155]. Since there is only a small fraction (5%) of gallium in the glass, it is assumed that the primary features in the Raman spectra of these glasses are due to the Ge-based units and the effect of gallium incorporation will be seen in the relative magnitude of the laser-induced changes. Comparing the spectra in

Figure 5.14 to that of the Ga-free glass in Figure 5.9, the incorporation of gallium into the glass matrix reduces the magnitude of these photo-induced changes. It is thought that the gallium in

the network is found primarily in GaS_4 units. The presence of these units constrains the ability of the Ge-based units to connect through S-S bridges and results in a reduced ability of the glass matrix to reorganize upon the absorption of laser energy during irradiation, which explains the reduction of the photo-expansion observed in gallium-containing glasses relative to gallium-free glasses. The further incorporation of selenium into the glass, which would make a more optically nonlinear and functionally useful glass, further reduces the photosensitivity of the glass to femtosecond laser irradiation. The Micro-Raman spectra of the composition containing 2% selenium as a function of laser dose are depicted in Figure 5.15.

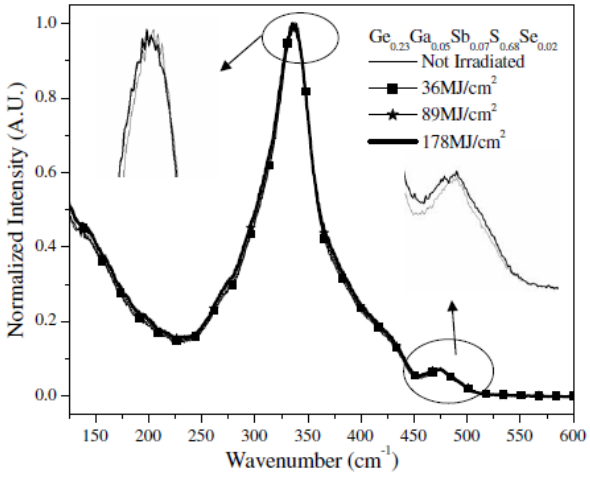

Figure 5.15:Micro-Raman spectra of x=0.02 glass as a function of laser dose [62]

Although the main band shifts to lower wavenumbers and becomes broader, the magnitude of the changes are quite small for this glass composition. It should be noted, however, that the magnitude of these changes are indeed above the noise level and the irradiated areas can be repeatedly differentiated from un-irradiated areas in measurements taken all across the sample. The presence of selenium atoms in low concentration results in a short Se-Se chains that along

with the gallium-based units restrict the connection of the primary GeS_4 units. Thus, the structural response of the glass matrix to laser irradiation is largely in the form of bond distortions rather than the more radical bond breaking and reorganization associated with photo-expansion in the Ga- and Se-free glass, $Ge_{23}Sb_7S_{70}$. The incorporation of increased amounts of selenium into this relatively open glass network continues this trend and results in a low photosensivity to laser irradiation.

5.4. Summary

In this chapter, the effect of compositional variations on germanium-based chalcogenide glasses was discussed. These experiments mark the first reports of the femtosecond laser photo-response of these glass compositions and serves to expand the understanding of the capabilities for the femtosecond laser processing of chalcogenide materials. The glasses are all in the bulk form because bulk glasses are of primary interest for 3D devices fabricated through femtosecond laser processing. Furthermore, these germanium-based glass compositions are of interest for photonic and opto-fluidic structures with applications in the IR due to their high stability, IR transparency, and compositional configurability.

The first glass family, $Ge_{23}Sb_7S_{70-X}Se_X$, focuses on the effect of the ratio of two chalcogen atoms in the glass matrix. This ratio is important as it controls the magnitude of the optical nonlinearity of the glass. The ratio of chalcogen elements also affected the response of the glass to femtosecond laser irradiation. A calculation of the free electron density generated in the focal volume during processing indicated that although nonlinear absorption is the predominant means

of energy transfer from the laser, a progressive red-shift of the optical bandgap with increasing selenium content leads to increased linear absorption and a subsequent reduction of the ablation threshold. Furthermore, it was seen that the selenium-free glass displays the strongest photo-response as measured by the magnitude of the laser-induced photo-expansion of the glass surface. Through Micro-Raman spectroscopy, it was determined that the photo-response derives from a modification of the bond structure from isolated GeS_4 units to a more connected glass network. The presence of selenium in the network disrupts the ability of the glass network to restructure in response to laser irradiation, resulting in a decreased photo-sensitivity. Thus, the gain of optical nonlinearity is countered by an decreased ability to use femtosecond laser processing to fabricate photonic elements in the glass.

The second glass family, $Ge_{18}Ga_5Sb_7S_{70-X}Se_X$, explores the effect of the addition of a small percentage of gallium in place of germanium. The motivation behind this composition variation is to open the glass network to enhance its capacity for dopants such as erbium, which would allow for the fabrication of active optical structures. In terms of the sensitivity of the glass to femtosecond laser irradiation, the presence of gallium disrupts the glass matrix in much the same way that selenium does, which results in a decreased photosensitivity. However, as long as the concentration of selenium is below ~20%, femtosecond laser processing is feasible.

In addition to characterizing the effect of the composition on the photo-response, the effect of the repetition rate of the femtosecond laser was studied. The glasses were exposed to both low repetition rate (1kHz) and high repetition rate (35MHz) laser sources. As described in section 3.2, the separation in time between successive laser pulses relative to the response time

of the lattice to absorbed laser energy determines the degree of cumulative heating effects during processing. It was shown here that these chalcogenide glass compositions are sensitive to cumulative thermal effects during processing. Irradiation of the glasses with the 1kHz repetition rate laser source resulted in little or no photo-expansion of the material and a higher irradiance necessary to induce ablation. A dose-dependent photo-expansion of up to hundreds of nanometers characterized the photo-response of the glasses to 35MHz irradiation.

CHAPTER 6: FEMTOSECOND LASER DIRECT WRITING OF CHALCOGENIDE GLASS FILMS

Thin film chalcogenide glasses are a versatile platform for the fabrication of integrated photonic devices such as nonlinear optical switches and opto-fluidic lab-on-a-chip detection systems. The use of thin films for integrated devices enables multiple fabrication techniques to be employed for the creation of novel devices. In addition to lithographic processing techniques, laser processing is uniquely suited for the controlled modification of optical properties of chalcogenide glass and can be employed to fabricate optical as well as fluidic elements. In this chapter, the photo-response of chalcogenide thin films to femtosecond laser irradiation is characterized in terms of photo-expansion, the optical refractive index shift, and the modification of the molecular bond structure. Several different film compositions are considered including two thin-film forms of a germanium-based composition described in CHAPTER 5 as well as arsenic-based compositions. These studies serve two purposes: (1) to extend the understanding of the physical mechanisms associated with the laser modification of various chalcogenide glasses, and (2) to select an appropriate composition to be used for studies of the use of femtosecond laser processing to fabricate micro-fluidic elements in chalcogenide glasses, which is discussed in CHAPTER 7.

6.1. $Ge_{23}Sb_7S_{70}$ Films

This section describes femtosecond laser induced modifications of the optical and physical properties of thin-film $Ge_{23}Sb_7S_{70}$ chalcogenide glass. The bulk form of this same composition was studied extensively in CHAPTER 5 and was shown to exhibit a high photosensitivity to

femtosecond laser light. Two films, one created by thermal evaporation (TE) and one created by pulsed laser deposition (PLD), are described throughout this section. The study of two films of the same composition created by two different methods provides insight into the influence of thermal history and initial bond configuration on the photosensitivity of the glass.

6.1.1. Film Deposition

Chalcogenide glass thin films from parent bulk glasses of composition $Ge_{23}Sb_7S_{70}$ were deposited using thermal evaporation (TE) and pulsed laser deposition (PLD) techniques. The bulk glasses used as targets for the film deposition were prepared from high purity elements (Ge: Aldrich 99.999%, Sb: Alpha 99.9% and S: Cerac 99.999%) by Dr. Richardson and her team at Clemson University. The deposition of the investigated films was carried out using two samples of the same parent glass composition as targets. The TE film was fabricated by Drs. Kimerling and Agarwal and collaborators at MIT. Thermal evaporation was performed at a base pressure of 10^{-6} Torr at a deposition rate of 2nm/min using glass powder ground from bulk glass (see Figure 6.1).

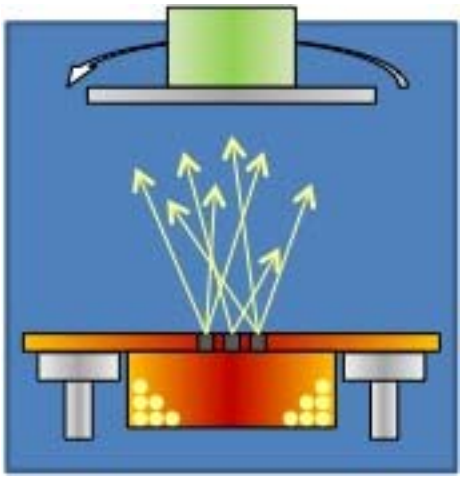

Figure 6.1: Schematic of the thermal evaporation process for fabricating a glass thin film.

The PLD film was fabricated by Dr. Luther-Davies and collaborators at the Australian National University. The laser source was a 355nm Nd:YVO_4 laser with 12ps pulses at a 28MHz repetition rate. The targets were polished bulk glass at least 2 cm in diameter and 3 mm in thickness and the maximum laser intensity on target was ~10^{10} W/cm^2. A schematic of the process is shown in Figure 6.2.

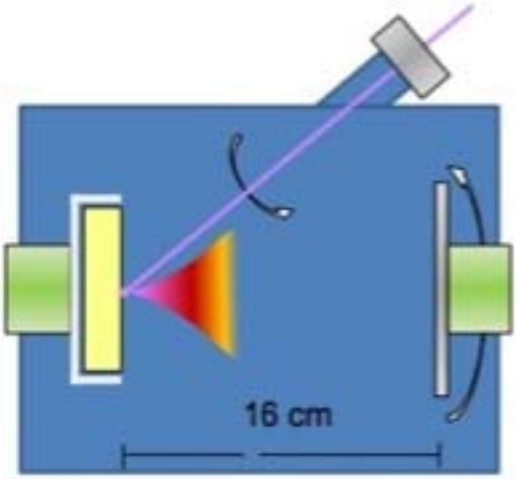

Figure 6.2: Schematic of the pulsed laser deposition process

The TE and PLD films were deposited onto glass microscope slide substrates and had thicknesses of (1.4±0.1) μm and (1.0±0.1) μm, respectively. The thicknesses of the films were measured using a scanning electron microscope (SEM) and confirmed with Zygo 3D Optical Profiler. The films did not display any evidence of crystallization or phase separation. The films did not undergo an immediate post-deposition annealing, but all exposure studies were carried out months after film deposition where extensive film relaxation was confirmed to have occurred.

6.1.2. Femtosecond Laser Sources

The photosensitivity of the two glass films in response to both kHz and MHz repetition rate pulses were studied in order to determine the role of thermal accumulation effects on the processing of the films. The Spectra Physics Spitfire system with a 1kHz repetition rate that was described in section 3.4.2 was used and the KMLabs oscillator with a repetition rate of 80MHz described in section 3.4.1 was used. The oscillator also served as the seed laser for the amplified system and thus had similar pulse characteristics, allowing for accurate comparison of the two irradiation regimes. The laser pulse energies used in this experiment were on the order of nanojoules for the MHz laser and microjoules for the kHz laser. A 0.25NA microscope objective was used to focus the laser light onto the samples, which were mounted on a computer-controlled 3D translation stage (VP-25XA, Newport).

6.1.3. Differences Between the TE and PLD Films

The fabrication of optical structures in transparent media such as glasses using femtosecond laser direct writing relies on the use of absorbed laser energy to create localized regions of modified material that has different optical, chemical, or structural properties relative to the surrounding host material. The difference in the properties of these locally modified zones can then be exploited to form functional devices. For example, the modification of the refractive index through FLDW can be exploited to form diffraction gratings by fabricating a spatially periodic refractive index structure, Fresnel-type lenses through a through the formation of appropriately spaced concentric rings of periodic refractive index, or optical waveguides in the shape of continuous lines. The modification of other physical and chemical properties gives rise to a modification a materials susceptibility to a particular etchant, which can be exploited for the fabrication of micro-channels. The reliance of FLDW on the creation of a localized modification of material implies that the initial state of the material is critical to determining the nature of the material's reaction to absorbed laser energy. Micro-Raman spectroscopy along with a calculation of the number of available modifiable bonds in each of the films were used as the baseline for understanding the photosensitivity of the TE and PLD films to femtosecond laser pulses. The Raman spectra of these un-irradiated TE and PLD films are shown in Figure 6.3.

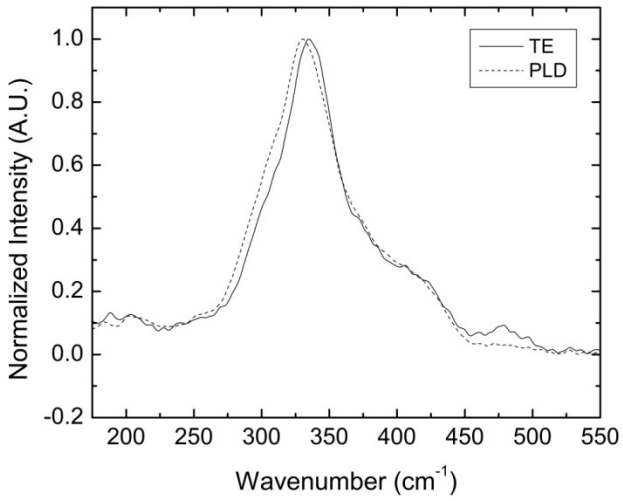

Figure 6.3: Raman spectra of as-deposited films fabricated by thermal evaporation (TE) and pulsed laser deposition (PLD). [59]

A difference in the bond structure as well as the thickness of the films gives rise to a difference in the number of available bonds to be modified within the focal volume of the writing laser. The total number of Ge-S bonds present in the laser local focal volume is calculated using the following equation:

$$\#(Ge-S) = 4 \cdot Ge_{At\%} \cdot \frac{N_A \rho}{M} V \tag{29}$$

where $Ge_{At\%}$ is the atomic fraction of Ge in the glass network (0.23), N_A is Avogadro's number, ρ is the density of the film, M the molecular weight of the glass, V the volume of the glass within focal region of the laser, and the factor of 4 results from the four-fold coordination of Ge atoms in the glass network. As the Ge-based molecules are the primary species in the glass and constitute most of the Raman spectrum, monitoring the relative fractions of these molecules before and after irradiation will provide insight into the physical mechanisms of photosensitivity

in this glass. Furthermore, only Ge-S bonds are considered as the absence of a Raman peak at 260cm^{-1} indicates that no homopolar Ge-Ge bonds are present in either glass film. The volume of glass within the focal region of the laser is calculated using the formula $V = \pi\omega_0^2 T$ to be 1.8x10^{11} and 1.3x10^{11} cm^3 for the TE and PLD films, where T, the film thickness, is 1.4±0.1 and 1.0±0.1 μm, respectively. It is assumed that the entire thickness of the film is affected by the laser irradiation as the film thickness is smaller than the focal depth of the focusing laser. The densities of the films have been estimated using the Lorentz-Lorenz equation

$$\frac{n^2-1}{n^2+2} = \frac{4\pi}{3}\frac{N_A\rho}{M}\alpha \qquad (30)$$

which relates the refractive index (n), density (ρ), and mean polarizability (α) [156, 157]. It is assumed that the mean polarizability of the films is equal to that of the bulk material of the same composition, though some slight density variation will be expected due to thermal history (and energy) associated with the two deposition techniques. Using a refractive index at λ = 1μm of 2.14±0.02 and a measured density of 2.94±0.02 g/cm^3 for the bulk glass, the mean polarizability for glasses of this composition at 1 μm has been estimated to be (3.5±0.06)x10^{-24} cm^3. Substituting measured refractive indices at λ = 1μm for the TE (2.26±0.02) and PLD (2.30±0.02) films into Eq. (3), the resulting densities of the films were determined to be 3.12±0.06 g/cm^3 and 3.17±0.06 g/cm^3, respectively. The slight variation of the film densities is expected due to the different thermal histories and energy associated with the two techniques and the higher density of the glass fabricated using pulsed laser deposition confirms the validity of the calculation. The

total number of Ge-S bonds estimated to be in the focal volume of the laser using equation (29) was then calculated to be 6.38±0.01 $x10^{11}$ for the TE film and 4.63±0.01 $x10^{11}$ for the PLD film.

Table 6.1 contains the total number of Ge-S bonds in 5 primary Ge-based molecules along with their relative percentage of each bond-type within one focal volume of the irradiating laser. These values were calculated using the total number of bonds along with a deconvolution of the Raman spectra in Figure 6.3 into the individual bands of the constituent vibrational modes of the molecules in the glass

Table 6.1: Number of bonds in one focal volume of 5 primary Ge-based molecules in the un-irradiated TE and PLD films. The relative percentages of each band is in parenthesis.

	Raman Band				
	$GeS_{4/2}$ 325cm^{-1}	**GeS_4 338cm^{-1}**	**$GeS_4S_{2/2}$ 370cm^{-1}**	**$GeS_{4/2}$ 400cm^{-1}**	**S_3Ge-S-GeS_3 425cm-1**
TE Film	$1.3x10^{11}$ (21%)	$2.6x10^{11}$ (41%)	$1.3x10^{11}$ (20%)	$7.3x10^{10}$ (11%)	$4.4x10^{10}$ (7%)
PLD Film	$5.8x10^{10}$ (13%)	$2.3x10^{11}$ (50%)	$8.2x10^{10}$ (18%)	$5.3x10^{10}$ (11%)	$3.6x10^{10}$ (8%)

These spectra have been deconvolved using the same method for bulk glasses in the Ge-Sb-S-Se family [61]. The measurement and deconvolution of the spectra were done in collaboration with Clemson University. The Raman spectrum of the as-deposited films consists of a broad band from 275-450cm^{-1} and two low-amplitude bands in the 200-250 and 450-550 cm^{-1} range where the primary band is formed by overlapping Raman bands of Sb_2S_3, GeS_2 and S_n structural units. The weak band near 450-500 cm^{-1} has been assigned to vibration modes of sulfur.

The structure of the as-deposited TE film is interpreted to be more connected through a larger number of $GeS_{4/2}$ units compared to the structure of the PLD film Thus, the TE film contains not

only a more connected network but also a larger number of Ge-S bonds within the laser focal volume, indicating a higher susceptibility for bond modification through exposure to the femtosecond laser pulses than an identical exposure to the corresponding PLD film. This understanding will assist in the interpretation of the photosensitivity measured in the following sections.

6.1.4. Ablation Threshold

The ablation threshold was determined in these glass films by fabricating a spatial two dimensional map on the film surface consisting of a series of photo-written lines with increasing irradiance. The calculated number of laser pulses per focal spot on the samples was 198 and $4x10^6$ for the kHz and MHz lasers respectively. This approach to measuring the threshold using photo-written lines differed from the method used on the bulk glass and was chosen here as it defined the practical boundary between ablation and sub-threshold photo-modification of these films for the conditions used in this experiment. The ablation threshold was here considered to be the lowest laser irradiance that induced ejection of material from the film surface to form a trench. A measurement of the surface profile of the film using a Zygo NewView 6300 3D Optical Profiler was used to determine the ablation threshold.

The ablation thresholds of the two films in both the kHz and MHz irradiation regimes are shown in Table 6.2. Although the compositions of the two films are equivalent, there is a clearly observable difference in the ablation thresholds of these films in both repetition rate irradiation regimes.

Table 6.2: Ablation threshold of the TE and PLD films with 1kHz and 80MHz repetition rate pulses

Film deposition technique	198 Pulses per focal spot (1 kHz)	$4x10^6$ Pulses per focal spot (80 MHz)
TE	103.2 ± 0.9 TW/cm^2	40.7 ± 3.7 GW/cm^2
PLD	87.2 ± 0.9 TW/cm^2	54.3 ± 4.8 GW/cm^2

Considering first the MHz interaction regime, the thresholds for the TE and PLD film are 40.7±3.7 GW/cm^2 and 54.3±4.8 GW/cm^2, respectively. The TE film is more photosensitive and has a 25% lower ablation threshold than the PLD film. The slightly larger free volume in the TE structure may accommodate thermal-induced local distortion during the high repetition rate irradiation due to a limited ability to dissipating thermal energy between shots. Additionally, the larger thickness and thermal mass of the TE film results in a larger number of bonds within the focal volume available to be modified (as calculated in 6.1.3), which means the effective absorption of laser energy as heat would be larger for this film than the PLD film. This increased trapping of heat within the film may contribute to a relatively lower ablation threshold.

The ablation threshold of the two films are about three orders of magnitude higher when exposed to kHz repetition rate pulses, increasing to 103.2±0.9 TW/cm^2 and 87.2±0.9 TW/cm^2, for the TE and PLD films, respectively. This increased ablation threshold for low-repetition rate irradiation is consistent with the response of the bulk material. Under these conditions, the thermal diffusion of heat from the focal volume is on the same timescale as the time separation between pulses. Comparing the two films, the ablation threshold for the TE film is larger than for the PLD film, a reversal relative to MHz irradiation. The smaller free volume of the PLD film

makes the glass matrix more responsive to the high pulse energies required for ablation without the presence of thermal effects and bond distortion that is present with MHz repetition rate irradiation. In addition, the slight red-shift of the bandgap of the TE film relative to the PLD film (see Figure 6.4) may allow for an increased amount of linear absorption on the tail of the absorption curve.

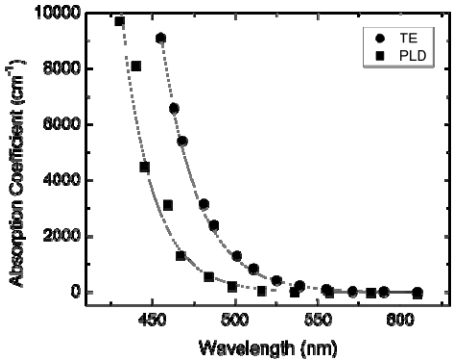

Figure 6.4: Absorption spectra of the films deposited by Thermal Evaporation (TE) and Pulsed Laser Deposition (PLD) techniques. [59]

6.1.5. Photo-expansion

Photo-expansion is a common result of laser irradiation in many chalcogenides. We have observed this phenomena for bulk $Ge_{23}Sb_7S_{70}$ glass [61] and for both bulk and thin film As_2S_3 glasses under NIR femtosecond laser exposure [51, 52]. Messaddeq et al have also observed an increase of the film thickness in the Ge-Ga-S and Ge-Ga-As-S glass systems with an increase of the exposure time for all powers when exposed to UV light at 351 nm [158].

The effect of femtosecond laser irradiation on the surface morphology of the films was studied as a function of the laser irradiance, the number of pulses per spot and the laser repetition rate. With both the high and low repetition rate lasers described in section 6.1.2, two series of photo-

written lines with varying laser parameters were fabricated. In one series, the laser irradiance was varied while the number of pulses per focal spot was varied. In a second series, the number of pulses per focal spot was varied while the laser irradiance was kept constant. A 0.25NA (10X) microscope objective was used to focus the femtosecond laser for all of the irradiations. The surface profile of the photo-written features was then measured with the Zygo NewView 6300 3D Optical Profiler and verified with a μTA-2990 from TA Instruments used as an AFM. The measurements using the two instruments were found to be in agreement within the accuracy of the measurements, ±0.7 nm.

A measurement of the surface profiles of the irradiations revealed that both the TE and PLD films exhibited a photo-expansion upon irradiation with kHz and MHz repetition rate pulses. The magnitude of the photo-expansion of the films as a function of laser irradiance and the number of pulses per focal spot is depicted in Figure 6.5 and Figure 6.6, respectively. The absolute magnitude of the photo-expansion is plotted with closed symbols and the open symbols represent the photo-expansion normalized to the film thickness (T). Pulses with the 80MHz repetition rate induce a photo-expansion on the order of tens of nanometers, whereas 1kHz repetition rate pulses induce a smaller (<10nm) photo-expansion. This increased photo-expansion and photo-sensitivity upon MHz repetition rate irradiation is similar to the photo-response of the bulk glass of the same composition described in section 5.2.2. However, both the TE and PLD films are photosensitive to kHz repetition rate pulses, whereas the bulk film did not exhibit any observable photo-expansion. This is the first demonstration of the impact of the initial bond state of a glass impacting the photosensitivity of a glass composition to femtosecond laser irradiation. The highly interconnected glass matrix of the films is more responsive to

athermal processing of the glass with low heat accumulation. Additionally, the differences in the bond configurations of the two films of the same composition fabricated using different techniques also affect the photo-response. While both films exhibit a photo-expansion of ~3% for MHz repetition rate pulses that saturates with increasing laser dose, the PLD exhibits a photo-expansion that is 2-3 times larger than that of the TE film for kHz repetition rate pulses.

Furthermore, the photo-expansion of the films resulting from kHz repetition rate irradiation does not saturate within the range of conditions observed here as seen for MHz repetition rate irradiation. For MHz exposure, local distortion of bonds and bond reconfiguration associated with laser exposure saturates after the local bonds have been fully modified. Conversely, while similar modification is thought to occur in the kHz case, the absence of heat accumulation between successive pulses limits the number of bonds modified by any given pulse. This could explain the observation that kHz irradiation results in a generally lower magnitude of photo-expansion observed by kHz irradiation that has not yet saturated within this dose regime.

6.1.5.1 Dependence on Laser Irradiance

Figure 6.5(a) and (b) highlight the influence of the laser irradiance on photosensitivity of the TE and PLD glass films for kHz and MHz repetition rate pulses, respectively. The number of pulses per focal spot was fixed at 198 for the kHz repetition rate and $4x10^6$ for the MHz repetition rate. The ablation thresholds of the two films are indicated on the plots by vertical lines.

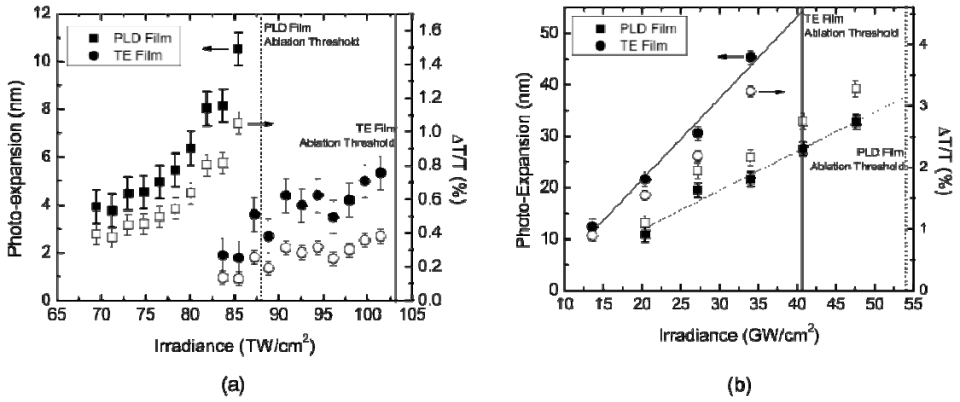

Figure 6.5: Absolute (closed symbols) and relative (open symbols) photo-expansion of the investigated films when irradiated with kHz (a) and MHz (b) repetition rate pulses as a function of the irradiance. The number of pulses was fixed at 197.6 (a) and $4x10^6$ (b). [59]

In all cases, the magnitude of the photo-expansion increases with increasing irradiance up to the ablation threshold with the highest measured photo-expansion occurring for laser irradiances just below this threshold. The maximum measured photo-expansion for the films using kHz irradiation was 5.5 ± 0.7 nm and 10.6±0.7 nm, corresponding to a film thickness increase of 0.4±0.01% and 1.1±0.01%, for the TE and PLD films, respectively. The larger photo-expansion of the PLD film compared to the TE film is consistent with the relatively lower ablation threshold under these conditions. The photo-expansion of the two films when exposed to MHz repetition rate pulses is shown in Figure 6.5(b). The magnitude of the photo-expansion is enhanced by incubation effects in the focal region of the laser, resulting in a larger photo-response that increases linearly with increasing laser irradiance until the ablation threshold. Under these conditions, the TE film exhibited the larger photo-expansion of the two films. Indeed, this is also consistent with the lower ablation threshold of the TE film for high repetition rate pulses. The maximum possible photo-expansion of these TE and PLD films with $4x10^6$

pulses has been estimated to be 54.4±0.7 nm and 37.8±0.7 nm, corresponding to 3.9±0.01% and 3.7±0.01%, using a linear regression of the data in Figure 6.5(b).

6.1.5.2 Dependence on Number of Pulses per Focal Spot

The role of laser dose at a fixed irradiance, measured in terms of the number of pulses incident on the films in one focal spot of the laser is highlighted in Figure 6.6. Photo-written lines on the TE and PLD films were fabricated with similar irradiance values of 83.6 TW/cm^2 and 85.4 TW/cm^2.

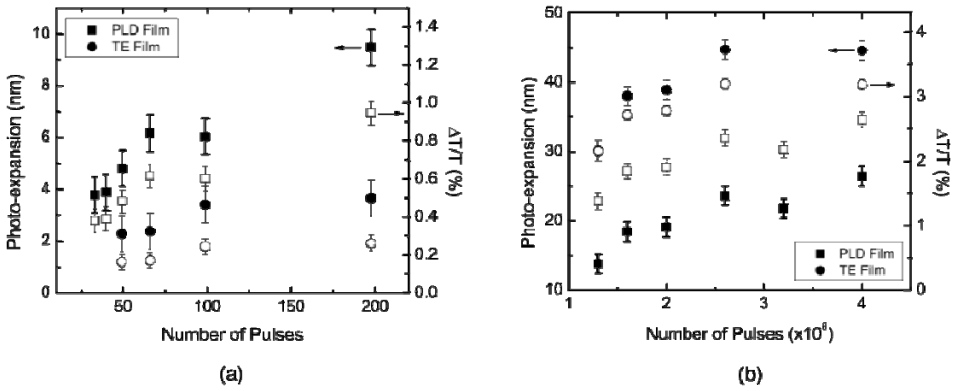

Figure 6.6: Absolute (closed symbols) and relative (open symbols) photo-expansion of the investigated films when irradiated with kHz (a) MHz (b) repetition rate pulses in function of the number of pulses. The irradiance was fixed at 83.6 and 85.4 TW/cm^2 (a) and at 33.9 and 40.7 GW/cm^2 (b) for the film deposited by thermal evaporation (TE) and pulsed laser deposition (PLD), respectively. [59]

As seen in Figure 6.5, the magnitude of the photo-expansion shown in Figure 6.6 is dependent on the laser dose. An increase in the number of laser pulses per spot results in an increase in the height of the photo-expansion. For both films, this dose-dependent modification reaches a saturation point after which further increasing the dose does not further increase the photo-expansion of the material. This type of saturation has been observed previously for another

chalcogenide glass, arsenic trisulfide [51]. It is thought that this saturation point is influenced by several factors including a saturation of the number of free electrons created in the focal region of the laser by the femtosecond pulse as well as a saturation of the available bonds to be modified within the focal volume. Although a photo-expansion was seen in both chalcogenide glasses, Micro-Raman spectra of the two different glass compositions have revealed different photo-response mechanisms for the two glasses. The photo-response of arsenic trisulfide has been characterized by a breaking of bonds and the formation of homopolar As-As and S-S bonds. [51, 54] while this Ge-based composition has been characterized by a more subtle modification of the bond structure [59, 61].

In response to kHz repetition rate pulses, the maximum observed photo-expansion under these conditions is 9.5±0.7 nm (a 1.0±0.01% film thickness increase) and 3.7±0.7 nm (a 0.3±0.01% film thickness increase for the PLD and TE films, respectively. The photo-written lines on the TE and PLD films were fabricated with similar irradiance values of 83.6 TW/cm^2 and 85.4 TW/cm^2. The observation that the PLD film has a higher photo-sensitivity and photo-expansion in response to kHz repetition rate pulses is consistent with the result in Figure 6.5(a). In addition, Figure 6.5 demonstrated that the photo-expansion of the films is largest when the laser irradiance is near the ablation threshold. Indeed, although the two films here were irradiated with similar irradiances, the ablation threshold of the PLD film was much lower and therefore much closer to the irradiance used in this experiment. It is expected that irradiating the TE film with an irradiance closer to the ablation threshold would increase the maximum photo-expansion of the film in response to kHz repetition rate pulses.

In response to the MHz repetition rate pulses, the films demonstrated an increased photo-expansion. In this case, the laser irradiance values used were of 33.9 GW/cm^2 and 40.7 GW/cm^2 for the TE and PLD films, respectively. After approximately 2.6x10^6 pulses, the response of both films begins to saturate with maximum observed photo-expansions of 44.6±0.7 nm for the TE film, corresponding to a film thickness increase of 2.7±0.08%, and 26.4±0.7 nm for the PLD film, corresponding to a film thickness increase of 2.4±0.08%. The relatively higher photo-response of the TE film as a function of the number of pulses per focal spot is in complete agreement with the data in Figure 6.5.

6.1.6. Correlation Between Free Electron Density and Photosensitivity

Photo-expansion is a result of the transfer of energy from the electron plasma generated through absorption of laser light to the glass matrix and thus the observable dependence of the magnitude of the photo-expansion of $Ge_{23}Sb_7S_{70}$ glass on the laser irradiation conditions can be understood by modeling the free electron density generated during femtosecond laser irradiation.

From section 3.1.3, the free electron density generated during femtosecond laser irradiation of a transparent material with sub-bandgap light can be described by the following rate equation:

$$\frac{\partial N}{\partial t} = \eta I(t) N + \sigma_n I(t)^n \tag{31}$$

where N is the number of free electrons, η is the avalanche ionization coefficient, k is the number of photons participating in MPI, σ_k is the k-photon absorption coefficient, and $I(t)$ is the laser intensity [107]. For chalcogenide glasses, Zoubir introduced a saturation term associated with the number of electrons available for this process [51]. Applying this to the model in

equation (31), results in the following model for the electron density generated by a single laser pulse:

$$\frac{\partial N}{\partial t} = (\eta I(t) N + \sigma_n I(t)^n) \cdot \frac{N_0 - N}{N_0} \tag{32}$$

where N_0 is the saturation parameter. Using this model with k=2, the free electron density associated with the irradiance-dependent photo-expansion shown in Figure 6.5(a) was calculated by integrating equation (32) with k=2. The values for η and σ_2 were used as fitting parameters in a least-squares algorithm since the values for these glasses under these irradiation conditions have not been reported. The data associated with kHz irradiation was used because cumulative thermal effects are negligible and most closely approximates single shot irradiation. The data is fit by postulating that the electron density associated with ablation is 1.7e21cm^{-3}. This is the electron density for which the plasma frequency is equal to the laser oscillation frequency, leading to strong absorption of the laser energy by the plasma [105, 111, 115, 152]. The calculations of the electron densities for the TE and PLD films are shown in Figure 6.7(a) and (b), respectively. The two films were fit independently. The model is able to predict the trend of the photo-expansion of both films and validates a correlation between the generated free electron density and the photo-response of the glasses.

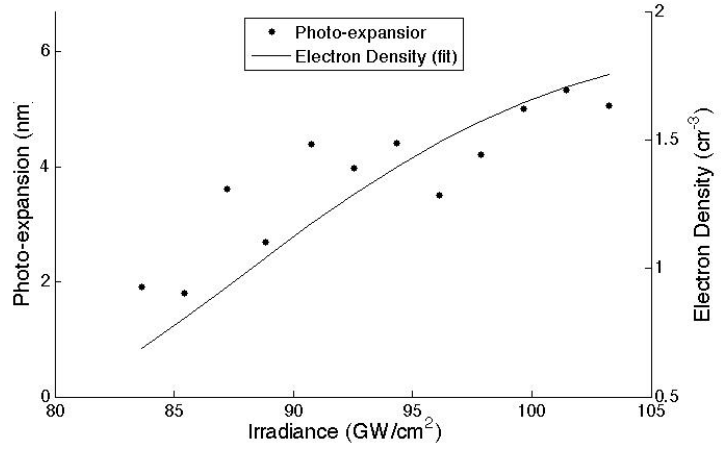

(a)

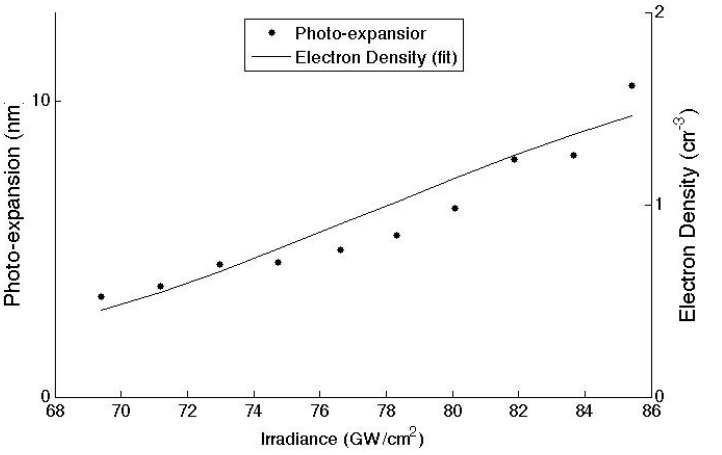

(b)

Figure 6.7: Free electron density of the TE (a) and PLD (b) films that give rise to the photo-expansion data in Figure 6.5(a)

The values of the avalanche and two-photon absorption coefficients for the two films are given in Table 6.3. The value for the TPA coefficient is presented as β with units of cm/GW, which is commonly reported in the literature. The resulting avalanche ionization coefficient that minimized the least squares error is the same for both films: 821 cm^2/J. The values of the two-photon absorption coefficients differed, however, with the value for the PLD film 5.6 times

larger than the value for the TE film. This larger TPA coefficient for the PLD film is consistent with the lower ablation threshold relative to the TE film as shown in Table 6.2. These results are the first reported values of the TPA coefficient at 800nm for this composition and are consistent with the findings of collaborators Petit *et al* who reported that the TPA coefficient was less than 0.1 cm/GW at 1064nm (an exact value was not reported).

Table 6.3: Values of the avalanche ionization and two-photon absorption coefficients for the TE and PLD films

Film	Avalanche Ionization Coefficient (η) (cm^2/J)	Two-Photon Absorption Coefficient (β) (cm/GW)
TE	821	0.05
PLD	821	0.28

The magnitude of the avalanche ionization coefficient reported here is up to two orders of magnitude larger than reported values for fused silica [105, 152] or arsenic trisulfide [51]. This is due to the low values of the TPA coefficient which force avalanche ionization to be a more dominant mechanism of nonlinear absorption under these irradiation conditions. In addition, the 120fs pulses used for this experiment are sufficiently long to allow for significant free electron growth through avalanche ionization, which was not the case for the 25fs pulses used by Zoubir *et* al for arsenic trisulfide[51].

6.1.7. Refractive Index Modification

The photo-induced refractive index modification associated with femtosecond laser irradiation was measured on both the TE and PLD films for the same laser conditions for which the photo-

expansion was measured. The photo-induced refractive index shift is the most critical parameter for determining the feasibility of this material as a substrate for femtosecond laser direct writing. Two methods have been used to measure the refractive index modification in these Ge-based chalcogenide films. The first method is through an analysis of the transmission spectra of the pre-and post-irradiated films using the Swanepoel method [159]. The second method was to measure the refractive index corresponding to the photo-expansion data provided in Figure 6.5 and Figure 6.6 through white light interferometry [51]. The use of these two measurement methods provided different insights into the refractive index change in the material.

The Swanepoel analysis was used to determine the induced refractive index modification as a function of wavelength in the transparent spectral region. A description of this method for the determination of the refractive index is given in section 4.2.2. The photo-modified area for this measurement was a 1.2 mm x 1.2 mm square region consisting of parallel lines separated by 2 μm. A large irradiated area was necessary for this measurement to ensure that the entire probe beam of the spectrometer was completely covered. The transmission spectra of the films in the range of 800nm to 1500nm before and after irradiation were measured using a Cary 500 spectrophotometer from Varian.

The refractive index measurement using white light interferometry had a much higher resolution (~2μm) and was used to determine the induced refractive index modification associated with the photo-expansion measured previously. The interferometer used for the measurement was a Zygo NewView 6300 3D Optical Profiler. The white light source had a bandwidth of 100nm centered

at 550n, Thus, the refractive index obtained using this method is averaged over the spectrum of the light source.

6.1.7.1 Transmission Spectrum Analysis Using Swanepoel's Method

The Swanepoel method was used to investigate the induced refractive index modifications of regions modified by both kHz and MHz repetition rate pulses. For the kHz experiment, large areas of the TE and PLD films were exposed to laser irradiances of 81.9 and 94.3 TW/cm^2 (corresponding to 5.3 and 8.9 TW/cm^2 below the ablation thresholds). The translation speed of the sample through the focal volume of the femtosecond laser was adjusted such that the films were exposed to 50 pulses per focal spot. Although the laser irradiance was near the ablation threshold in both films and a small photo-expansion was seen as described previously, no observable refractive index change was measured for either film.

A large refractive index modification was observed for both films after irradiation to MHz repetition rate pulses. The TE and PLD films were exposed to laser irradiances of 34 GW/cm^2 and 40.7GW/cm^2, respectively. The number of pulses per focal spot was set to 1.3x10^6. Figure 6.8 depicts the transmission spectra of the TE film before and after irradiation (a) as well as the calculated normalized refractive index ($\Delta n/n$), as a function of wavelength.

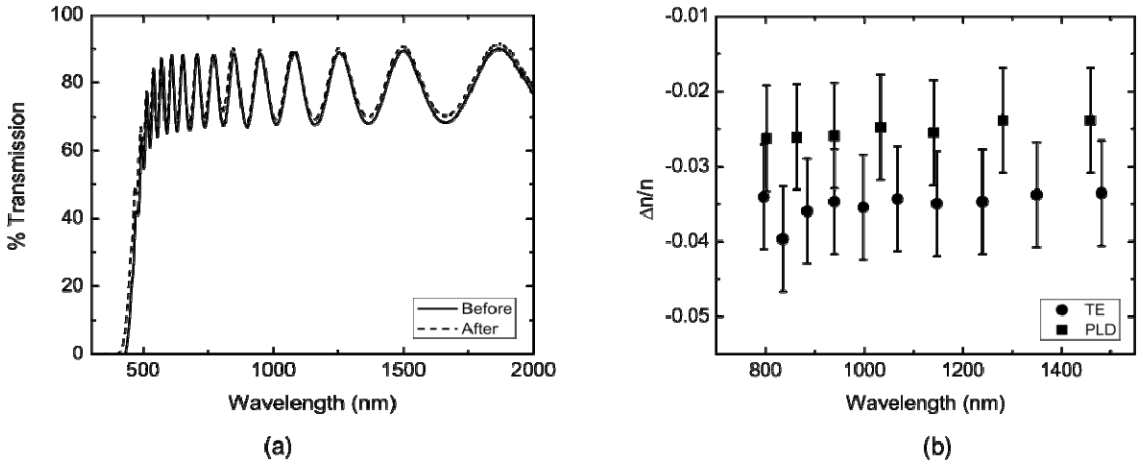

Figure 6.8: (a) Transmission spectrum of the TE film before and after irradiation indicating an induced bandgap shift and a modification of the interference pattern. The laser irradiance on the sample was 34.0 GW/cm^2 (6.7 GW/cm^2 below threshold) and the number of pulses per laser spot was $1.3 \cdot 10^6$. (b) $\Delta n/n$ of the investigated films deposited by thermal evaporation (TE) and pulsed laser deposition (PLD) as a function of wavelength. [59]

Looking at Figure 6.8(a), a clear modification of the interference fringes is observed as a result of the photo-modification. Through the Swanepoel analysis, it was determined that the induced refractive index of the photo-modified regions were lower than the surrounding unmodified film for both the TE and PLD films. The negative sign of the induced refractive index shift is opposite to that seen in similarly irradiated As-based chalcogenide bulk and film glasses and justifies the observation that the photo-response of any given glass is highly dependent on the composition and can differ significantly from otherwise similar glasses. The magnitude of the induced refractive index shift was large, reaching -0.08±0.02 at 1μm for the TE film and 0.06±0.02 at 1μm for the PLD film. As seen in Figure 6.8(b), this induced was seen to be constant at -3.5% and -2.5% for the TE and PLD films over the entire measured spectrum of the glass from 800nm to 1500nm. The absolute value of the induced change was not constant, and followed the dispersion curve of the material.

6.1.7.2 Analysis of the Optical Path Changes Using White Light Interferometry

The photo-modified lines that were measured for photo-expansion in section 6.1.5 were analyzed using white light interferometry for the induced refractive index modification. Since the bandwidth of the white light source is centered at 550nm, the wavelength results are reported for this wavelength. However, it should be understood that the refractive index measurements are an average of the changes as measured by a 100nm bandwidth.

When the samples irradiated with kHz irradiation were measured, no observable refractive index modification was seen for either film. Just as seen through the Swanepoel analysis, although a slight photo-expansion was measured, any modification of the refractive index was negligible.

The refractive index modification of the photo-written lines from MHz repetition rate pulses was is shown in Figure 6.9. The dependence on the laser irradiance and the number of pulses per focal spot are shown in parts (a) and (b), respectively.

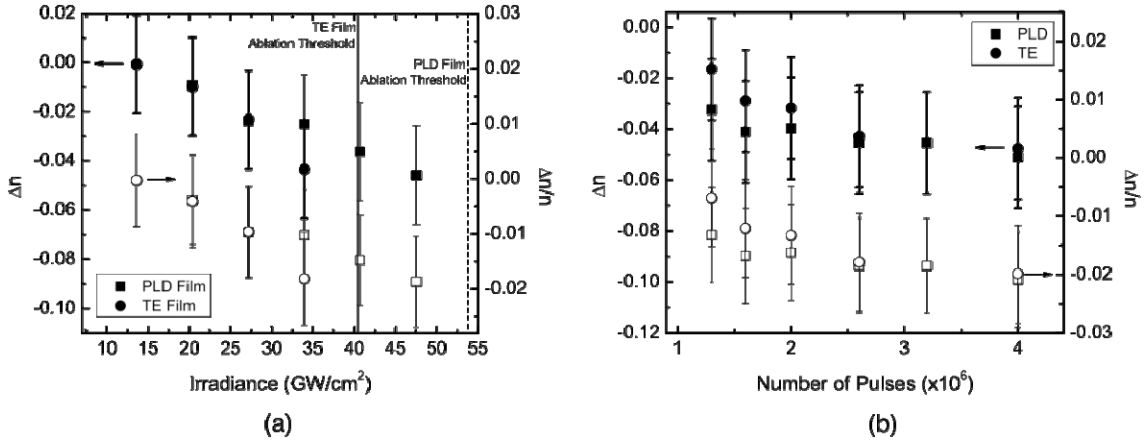

Figure 6.9: Absolute (closed symbols) and relative (open symbols) refractive index modification at 550 nm of the investigated films deposited by thermal evaporation (TE) and pulsed laser deposition (PLD) techniques as a function of laser irradiance (a) and the number of pulses per focal area (b). In (a), the number of pulses per focal area was held constant at $4 \cdot 10^6$ for both films. In (b), the laser intensity was held constant at 40.7 GW/cm^2 (13.6 GW/cm^2 below threshold) for the PLD film and 34.0 GW/cm^2 (6.7 GW/cm^2 below threshold) for the TE film. [59]

In a manner similar to the photo-expansion, the magnitude of the refractive index modification is seen to be a function of the laser dose and increases with both the laser irradiance and the number of pulses per focal spot. The maximum observed index decrease was -0.05±0.02, corresponding to a $\Delta n/n$ of 2% for both films when irradiated with 4×10^6 pulses with an irradiance near the ablation threshold of the film.

The Lorentz-Lorenz equation describes the refractive index as being a function of both the density and the mean polarizability of the glass. In order to understand specifically the relationship between the induced refractive index and volume modifications within the glass as a result of femtosecond laser modification, the absolute magnitude of the refractive index modification ( ) was plotted as a function of photo-expansion for the two films and is shown in Figure 6.10.

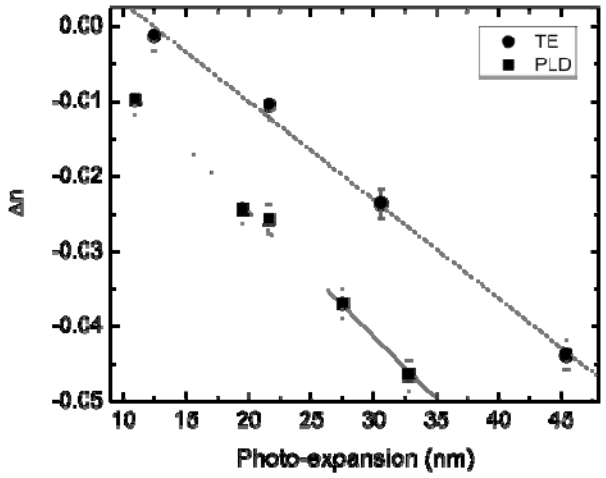

Figure 6.10: Δn as a function of photo-expansion for the films deposited by thermal evaporation (TE) and pulsed laser deposition (PLD) with varying laser irradiance. [59]

A linear relationship exists between the photo-expansion and the induced refractive index change in both films, which suggests that the same physical mechanisms are responsible for both types of material modification. Using the linear regression in Figure 6.10, the maximum obtainable refractive index modification under optimum laser irradiation conditions is was estimated to be of -0.066±0.02 for the TE film and 0.061 ± 0.02 for the PLD film. The PLD film is expected to have a lower optimum photo-response relative to the TE film as is consistent with previous discussions. However, the similarity between these estimates suggests that the underlying physical mechanisms responsible for the photo-response are quite similar for the two films and the observable differences are due to more subtle differences in initial bond configurations and densities of the two films.

6.1.8. Nonlinear Refractive Index Modification

The femtosecond laser-induced modification of the nonlinear refractive index can be found by measuring third harmonic generation at the film/air interface for both exposed and unexposed materials[34, 160-163]. A schematic of the experimental setup is shown in Figure 6.11. The excitation laser was an optical parametric oscillator system (Spectra-Physics, Tsunami-Opal System) that produces 130fs pulses at 1.5μm at a repetition rate of 80MHz. The excitation laser is focused onto the surface of the film using a 0.2NA microscope objective. The emitted third harmonic beam was filtered from the excitation beam and measured using a photo-multiplier tube (Hammamatsu R5700). The signal from the PMT was amplified using a current amplifier and a lock-in amplifier that was tuned to the laser repetition rate.

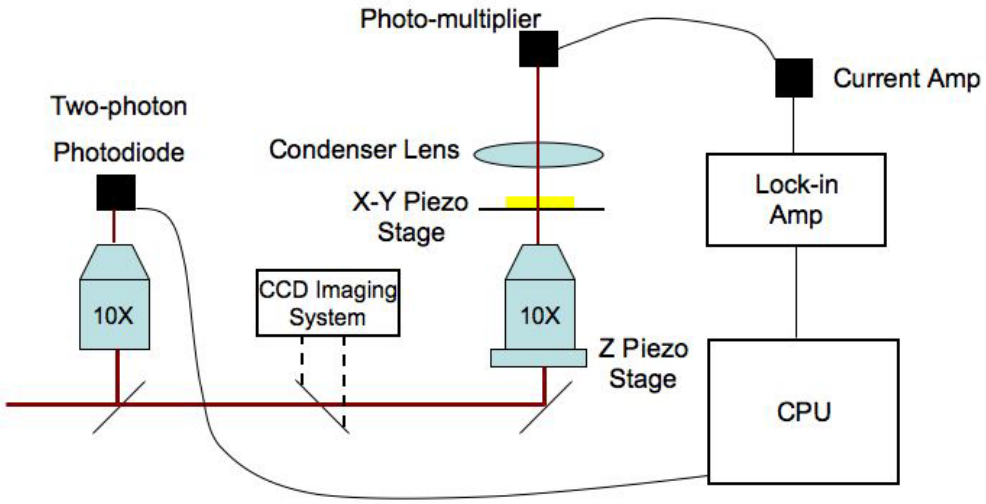

Figure 6.11: Schematic of experimental setup to measure the third harmonic generation of thin films.

The intensity of the THG signal generated at the interface of a glass film and air is described by

$$I_{3\omega} = \left(\frac{\chi^{(3)}}{\lambda}\right)^2 \left(\frac{1}{\pi c \epsilon_0 F}\right)^3 \frac{P_\omega^3}{3w^4\tau_p^3}|J|^2 \quad (33)$$

where $\chi^{(3)}$ is the third-order susceptibility,λ is the excitation wavelength, F is the repetition rate of the laser, P_ω and $\tau_p$are the power and pulse length of the excitation beam, w is the beam waist at focus, and J is the third-harmonic interaction length [161]. Using this expression, the laser-induced modification of the third-order susceptibility can be calculated through a ratio of the THG intensity of laser-modified material ($I_{IRR}^{3\omega}$) to unexposed material ($I_{UNIRR}^{3\omega}$) [34]:

$$\frac{\Delta\chi^{(3)}}{\chi^{(3)}} = \sqrt{\frac{I_{IRR}^{3\omega}}{I_{UNIRR}^{3\omega}}} - 1 \quad (34)$$

Furthermore, the third-order susceptibility can be related to the nonlinear refractive index by the relation:

$$n_2 = \frac{3\chi^{(3)}}{4n_0^2 c\epsilon_0} \quad (35)$$

Square regions of femtosecond laser-irradiated material measuring 50μm per side, which is considerably larger than the ~7um spot diameter, were fabricated on each film in order to ensure a reliable measurement of exposed material. The translation speed during fabrication was 20μm/s. The femtosecond laser induced variation of the nonlinear refractive index for the two films is described in Table 6.4. The values of $\Delta n_2/n_2$ were calculated using equations (34) and (35) and the value for Δn_2 was calculated with using the value $n_2 = 1.66x10^{-18}\, m^2/W$ that was measured for the bulk glass of the same composition as reported by Petit *et al* [164]. Given that the values for the TPA coefficient differed (by a factor of ~5) for the TE and PLD films

(see Table 6.3), it is likely that the value of n_2 also differs slightly for these two films. The value of Δn_2 presented here is meant to provide an estimate for comparative purposes.

Table 6.4: Modification of the nonlinear characteristics of TE and PLD films as a function of femtosecond laser irradiance. The value of Δn_2 is calculated based the reported value for bulk glass of the same composition: $n_2 = 1.66x10^{-18}\, m^2/W$ [164].

	Photo-modification		
Film	**Irradiance** $\left[\frac{GW}{cm^2}\right]$	$\frac{\Delta n_2}{n_2}$	$\Delta n_2 \left[\frac{cm^2}{W}\right]$
TE	28.1	0.81	$1.34x10^{-14}$
	31.6	1.04	$1.73x10^{-14}$
PLD	50.0	0.18	$2.99x10^{-15}$
	53.0	0.65	$1.08x10^{-14}$

Femtosecond laser irradiation is seen to have a strong impact on the nonlinear properties of these chalcogenide glass films. Similar to the induced photo-expansion and linear refractive index modification, the magnitude of the induced modification is dependent on the laser irradiance. The magnitude of the induced modification of the nonlinear refractive index was larger for the TE film than for the PLD film, which is consistent with the observations for both the photo-expansion and the linear refractive index. For both films, femtosecond laser irradiation induced a positive Δn_2 associated with a negative Δn. In addition, the value of $\Delta n_2/n_2$ is up to 50 times larger than the value of $\Delta n/n$. These patterns are consistent with reported results of femtosecond laser modification fused silica, for which Δn_2 is negative and Δn is positive [34, 165]. Thus, the nonlinear optical properties of the glass is more strongly dependent on the structural modifications of the glass matrix associated with the glass matrix associated with laser

processing than the linear optical properties. Indeed, Petit *et al* have shown that the nonlinear refractive index of the similar chalcogenide glasses is partially a function of the bandgap and the density of lone pair electrons [164].

6.1.9. Glass Matrix Reorganization

Several physical mechanisms associated with photo-sensitivity and photo-expansion in chalcogenide glasses as a result of laser modification have been proposed including local atomic changes [153], photo-induced fluidity causing a reduction of local stress in the glass [166], intramolecular and intermolecular bond breaking and reformation [167, 168], the movement of chalcogen atoms into the irradiated area [158], and oxygen incorporation [169].

Micro-Raman spectroscopy was used to provide insight into the physical mechanisms associated with photo-sensitivity in the TE and PLD glass films studied here. The spectra were measured using a Kaiser Hololab 5000R Raman spectrometer with a resolution of 2-3 cm^{-1} at room temperature. The spectra were measured and decomposed into constituent Raman bands by Dr. Richardson and collaborators at Clemson University. The spectra presented here were further analyzed to include a calculation of the number of bonds modified during the irradiation process and the physical mechanisms associated with the photosensitivity are discussed in terms of the feasibility of these glasses to be used as a substrate for femtosecond laser direct write fabrication.

The femtosecond laser photo-response of the two glass films here is similar to the previous study on bulk glasses described in section 5.2.3 and is characterized by a modification and reconfiguration of the bond configuration of the glass by progressively decreasing the connectivity between the Ge-based tetrahedral units in the glass matrix [61].

The Micro-Raman spectra of the TE and PLD films in response to kHz repetition rate laser modification are shown in Figure 6.12(a) and (b), respectively. The number of pulses per focal spot for both films was ~198.

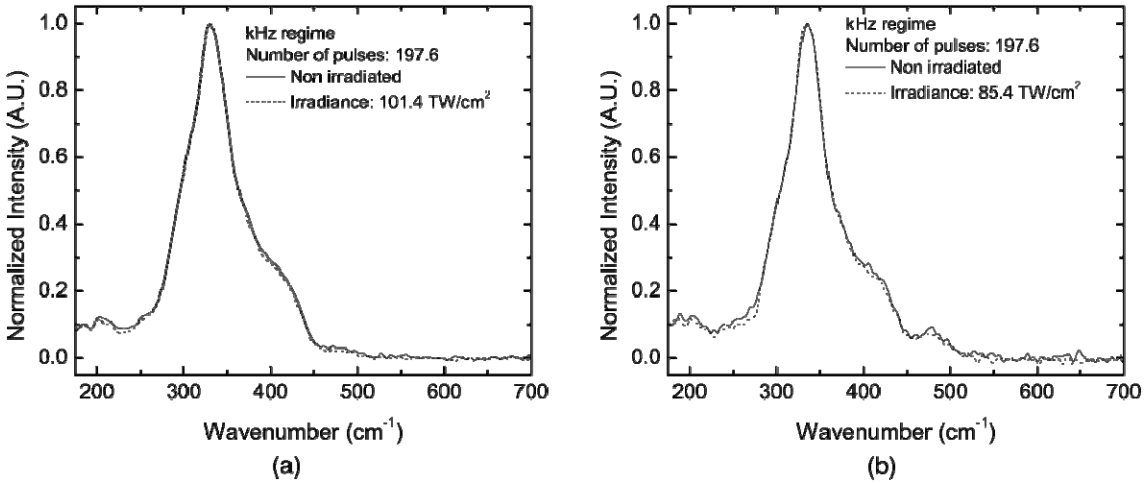

Figure 6.12: Raman spectra of the films deposited by (a) thermal evaporation (TE) and (b) pulsed laser deposition (PLD) techniques before and after irradiation using kHz repetition rate pulses (λ_{exc}=785nm). [59]

The only observed modification of the bond structure of either film was a subtle decrease in the shoulder of the main band near 400cm^{-1}. This change suggests a small, but measurable, shift of the concentration of corner-sharing $GeS_{4/2}$ molecules to edge-shared molecule [170]. This minor modification of the glass matrix results in a low (<2%) volume change (photo-expansion) and negligible refractive index modification as observed in previous sections.

The Micro-Raman spectra of the TE and PLD films as a function of laser irradiance are shown in Figure 6.13 (a) and (b), respectively. The translation speed of the samples was adjusted for a large dose with 4x10^6 pulses per focal spot incident on the samples.

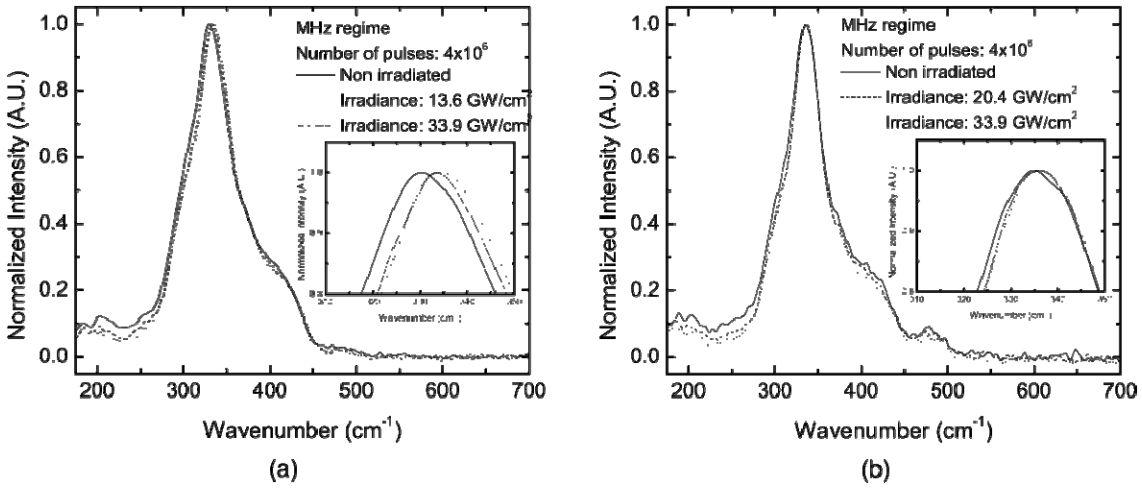

Figure 6.13: Raman spectra of the film deposited by (a) thermal evaporation (TE) and (b) pulsed laser deposition (PLD) before and after irradiation using MHz repetition rate pulses with $4x10^6$ pulses incident on the sample per focal spot (λ_{exc}=785nm). [59]

The spectra indicate that the effect of femtosecond laser irradiation on the structure of the two films is similar, which is consistent with the discussion in section 6.1.7. An increase in the irradiance results in a shift of the main Raman peak to a higher wavenumber accompanied by a slight decrease in the width of the main band. Through a deconvolution of the spectra to constituent Raman bands, this shift is caused by a decrease of the shoulders at 325cm^{-1} and 400cm^{-1} as well as an increase of the band at 338cm^{-1}. The amplitudes of the outer bands in the ranges of 175-225cm^{-1} and 450-550cm^{-1} also decrease. Taken together, these Raman modifications signify a progressive shift from corner-sharing $GeS_{4/2}$ units and Ge-S-Ge linkages (main band modification) to more isolated units [170] accompanied by a decrease in homopolar S-S bonds (450-550cm^{-1} bands). Thus, the impact of irradiation is to reduce the connectivity of the existing glass network and forming a higher percentage of isolated GeS_4 tetrahedra. Considering the results of the irradiation of the bulk material of the same composition, this subtle reorganization of the glass matrix upon laser irradiation is characteristic of this glass composition

in all forms. The observable results of these structural changes on a larger scale are then a photo-expansion of the material accompanied by a decrease of the refractive index.

The differences in the Raman spectra of the TE and PLD films are caused by differences in the initial bond configuration as seen in Figure 6.3 caused by differences in the thermal histories associated with different deposition techniques. Perhaps the most significant difference between the initial structure of the two films is the higher percentage of S-S linkages as measured by the bands in the 450-550cm^{-1} range. Indeed, a calculation of the area of these Raman bands in the PLD film reveals a ~26% decrease as a result of laser irradiation. The decreased S-S linkages in the glass matrix frees up the sulfur to bond directly to Ge atoms in isolated groups.

To further quantify the interpretation of the Raman spectra, the number of the primary Ge-based units within the focal volume of the femtosecond laser was estimated as a function of laser irradiance. This was calculated by measuring the areas beneath the deconvolved peaks of the Raman spectra in Figure 6.13 corresponding to vibrational modes of Ge-S units in the same way as described in section 6.1.3. Table 6.5 summarizes the results.

Table 6.5: Total number of Ge-S bonds in different GeS_4-based structural units within the focal volume of the laser in TE and PLD films associated with Raman modifications in Figure 6.13. The percentage of Ge-S bonds associated with the Raman bands is shown in parenthesis.

	TE film			PLD film		
Raman Wave-number (cm^{-1})	Un-irradiated	Irradiance: 13.6GW/cm^2	Irradiance: 33.9GW/cm^2	Un-irradiated	Irradiance: 20.4GW/cm^2	Irradiance: 33.9GW/cm^2
325	1.3 x10^{11} (21%)	9.3 x10^{10} (15%)	7.3 x10^{10} (11%)	5.8 x10^{10} (13%)	4.6 x10^{10} (10%)	4.5 x10^{10} (10%)
338	2.6 x10^{11} (41%)	3.0 x10^{11} (46%)	3.1 x10^{11} (49%)	2.3 x10^{11} (50%)	2.5 x10^{11} (53%)	2.5 x10^{11} (53%)
370	1.3 x10^{11} (20%)	1.3 x10^{11} (20%)	1.3 x10^{11} (20%)	8.2 x10^{10} (18%)	7.9 x10^{10} (17%)	8.0 x10^{10} (17%)
400	7.3 x10^{10} (11%)	7.3 x10^{10} (11%)	6.8 x10^{10} (11%)	5.3 x10^{10} (11%)	5.4 x10^{10} (12%)	5.0 x10^{10} (11%)
425	4.4 x10^{10} (7%)	5.0 x10^{10} (8%)	5.4 x10^{10} (9%)	3.6 x10^{9} (8%)	3.8 x10^{10} (8%)	4.1 x10^{10} (9%)

This table clearly depicts the variations of the Micro-Raman spectra as a function of laser irradiance. For both films, laser irradiation induces a decrease in the Raman peaks at 325cm^{-1} corresponding to $GeS_{4/2}$ units accompanied by an increase of the Raman peaks at 328cm^{-1} and 425cm^{-1} corresponding to GeS_4 and S_3Ge-S-GeS_3 units. This shift results in a modification of the glass volume as the GeS_4 and S_3Ge-S-GeS_3 units are physically larger than the $GeS_{4/2}$ units and thus a photo-expansion is a clear result of the laser irradiation.

In addition, Table 6.5 depicts clearly the differences in the photo-response of the two films and the nature of the relatively higher photo-sensitivity of the TE film compared to the PLD film. The photo-sensitivity of this glass composition is closely linked to a shift from $GeS_{4/2}$ units to

isolated GeS_4 units. This is clearly seen in the TE film as a decrease of the relative fraction of $GeS_{4/2}$ units from 21% to 11% and an increase of the relative fraction of GeS_4 units from 41% to 49%. However, the initial structure of the PLD film contains a large percentage of the isolated GeS_4 units (50%) with only a 3% increase (and a corresponding 3% decrease in $GeS_{4/2}$ units) induced by irradiation. Thus, although the two glasses react in the same manner, the differences in initial structure have clear influences on the ability of the glass matrix to reorganize upon irradiation and thus also on the induced photo-expansion and refractive index modifications.

The conclusion of this study of Ge-based chalcogenide glasses described here and in CHAPTER 5 is that these glasses are highly photo-sensitive to femtosecond laser irradiation and are well suited for use as a substrate material for devices fabricated using the femtosecond laser direct write fabrication technique. The magnitude of the photo-response (including volumetric and refractive index modifications) can be tailored for the needs of the application in many ways. On a structural level, the fabrication method of the glass will impact the maximum magnitude of the photo-structural modifications. On the laser processing side, heat plays a critical role in the photo-sensitivity of the materials and thus high repetition femtosecond rate lasers should be used to induce thermal accumulation either on the surface or below. During fabrication, the relative magnitude of any photo-structural modifications can be controlled through the laser dose on the material, which can be modified through either laser irradiance or the number of pulses per focal spot (related to the translation speed of the material through the focal volume of the laser). The relative magnitude of the photo-structural changes can be dynamically controlled during the fabrication process, which enables the fabrication of position-dependent features or active feedback during fabrication. Because laser processing induces a negative modification in the

refractive index, the material is not well suited for direct fabrication of optical waveguides. However, the large magnitude of the change makes this substrate material well suited for use in diffractive optical applications as it is only a periodic modification of the refractive index that is of interest.

6.2. As/S/Se Films

In this section, a new family of chalcogenide glasses based on As_2S_3 and incorporating antimony and germanium are discussed. These glasses are of interest for the specific application of optofluidic circuits. Although the Ge-based glasses studied in previous sections have a high photo-sensitivity to femtosecond laser irradiation, the negative photo-induced refractive index modification is inappropriate for the application to optofluidic circuits as it is desirable to directly fabricate optical waveguides in the material.

Arsenic trisulfide has been well studied as a substrate for the laser fabrication of optical waveguides [51, 54, 55, 171-175]. In addition, As-based glasses have been shown to be stable against crystallization [53, 176]. In the present study, the femtosecond laser photo-response of glass films of the composition $As_{42}S_{58}$, $As_{36}Ge_6S_{58}$, and $As_{36}Sb_6S_{58}$ are studied in order to understand the effects of the incorporation of antimony and germanium on the laser photo-response. The incorporation of these two elements into an As-based chalcogenide serves to modify the connectivity of the glass matrix and further enhance the stability and performance of the glasses. An understanding of the femtosecond laser photo-response of these materials is necessary to determine the optimum material for use as a substrate for optofluidic devices in

which both optical waveguides and micro-channels are fabricated through femtosecond laser processing. This set of experiments thus served to select the appropriate material for the micro-channel experiments described in CHAPTER 7. The glasses used in the experiment were all fabricated using Thermal Evaporation and had a thickness of ~1μm.

6.2.1. Femtosecond Laser Sources

The femtosecond laser source used for this experiment was a home-built Ti:Sapphire oscillator with a repetition rate of 26MHz. A MHz repetition rate laser was chosen specifically to induce heat accumulation within the focal volume of the laser since previous studies demonstrated a strong dependence on thermal effects on the photo-sensitivity of Chalcogenide glasses. The laser was focused onto the film surface using a 0.25NA (10X) microscope objective lens and the sample was placed on a computer-controlled 3D translation stage (Newport, VP-25XA).

The sample was characterized in terms of its photo-sensitivity by fabricating a series of photo-written lines with varying laser parameters in the same way as for the Ge-based films described in section 6.1.5. The laser irradiance was set to 90% of the ablation threshold for each of the samples so that the photo-sensitivity of the different samples could be compared [59, 61, 62]. The influence of the laser dose on the photo-sensitivity was then measured by varying the number of pulses per focal spot on the sample. Additionally, by irradiating the samples under the same relative conditions, the effect of composition on the photo-sensitivity was also measured.

6.2.2. Photo-expansion

The laser-induced volume change was observed through a measurement of the surface profiles of the glass surfaces after irradiation. The Zygo NewView 6300 3D Optical Profiler was used to obtain the surface profiles with a height resolution of 0.1nm and the results are shown in Figure 6.14. The error bars on the graph represent the extent of spatial variations of the measured photo-expansion across the length of the photo-written line. Because the overall photo-expansion of the films is relatively low (<10nm), these small variations are thought to be due to slight variations of the translation stage and the laser power during the irradiation.

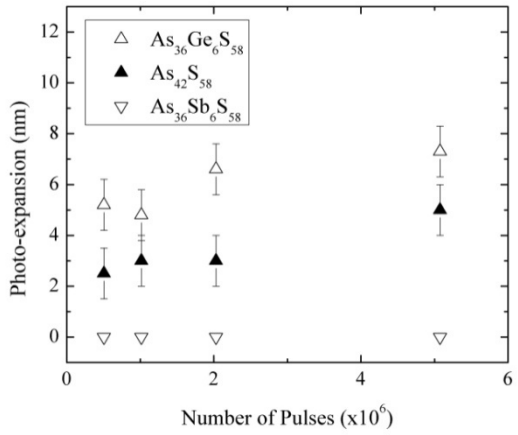

Figure 6.14: Change in surface profile (photo-expansion) of laser-written lines in as-deposited As36Ge6S58, As42S58, and As36Sb6S58 normalized to film thickness. Each film was irradiated at 90% of its ablation threshold. [177]

From the figure, it is clear that the glass composition had a significant effect on the photo-response of these glasses. A clear dose-dependent photo-expansion was seen for the $As_{42}S_{58}$ and $As_{36}Ge_6S_{58}$ compositions, which is consistent with the photo-response of many other chalcogenide glasses [51, 58, 59]. The maximum observed photo-expansion was measured to be

5 nm corresponding to an increase of the film thickness of 1.2% for $As_{42}S_{58}$ and 7nm corresponding to an increase of 0.8% for the $As_{36}Ge_6S_{58}$ composition. The addition of the germanium into the glass network provided a more open network that was more responsive to the absorbed laser energy. The photo-response of the $As_{36}Sb_6S_{58}$ composition was markedly different from the other two, however, with no observable photo-expansion upon irradiation. Therefore, any photo-modification in this material did not affect the density or volume of the glass.

6.2.3. Refractive Index

The photo-induced refractive index modification of the samples associated with the photo-expansion was measured with the white light interferometric technique described in section 4.2.1 and is shown in Figure 6.15.

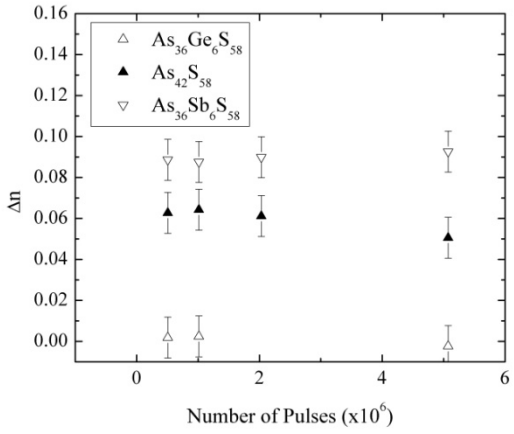

Figure 6.15: Refractive index change for as-deposited samples of (a) As36Ge6S58, (b) As42S58, and (c) As36Sb6S58 [177]

The photo-induced refractive index of these As-based chalcogenide glasses was positive. However, the magnitude was significantly affected by the composition. The composition $As_{36}Sb_6S_{58}$ displayed the largest induced refractive index change of 0.09 with the photo-expansion of the $As_{42}S_{58}$ reaching 0.06 for the same irradiation conditions. The composition $As_{36}Ge_6S_{58}$ displayed a negligible refractive index modification. It should be noted that these results are quite surprising in that the photo-expansion and the photo-induced refractive index modification do not coincide for all of the compositions. The composition $As_{36}Ge_6S_{58}$ had the largest refractive index modification but a negligible photo-expansion. Conversely, the composition $As_{36}Sb_6S_{58}$ displayed a negligible photo-expansion but a large refractive index modification. These observations indicate that the physical mechanisms of the laser-induced modification of the photo-expansion and refractive index are separate in these materials. Although this result is counter-intuitive, the Lorentz-Lorenz equation (equation (30)) [156] indicates that the density, refractive index, and material polarizability are all linked and allows for separate modification of both parameters. A more detailed study of these interactions would be a valuable study that could help shed light on a more universal theory to model and predict the photo-response of materials to femtosecond laser irradiation.

The composition $As_{42}S_{58}$ displayed a mid-range photo-sensitivity with both a photo-expansion and a photo-induced refractive index modification and was thus selected for further experiments on the fabrication of integrated optofluidic structures through femtosecond laser processing. Indeed, a photo-induced expansion or density modification indicates a significant change in the material bond structure as a result of femtosecond laser interaction, which has been previously characterized by bond breaking and the formation of homopolar bonds [51, 53, 54].

Furthermore, a positive refractive index change in laser-modified regions allows for the direct fabrication of optical waveguides.

$As_{36}Sb_6S_{58}$ was selected for studies involving direct ablation as this composition did not display a photo-induced density modification that could compete with ablation.

6.3. Summary

In this chapter, the photo-response of gernanium- and arsenic-based chalcogenide films was discussed. These films are of interest for use in integrated, planar, on-chip opto-fluidic sensors. There are several important outcomes of these studies. On an exploratory level, these studies served to expand the understanding of the photo-modifications induced in the germanium-based chalcogenide glass composition $Ge_{23}Sb_7S_{70}$ by femtosecond laser irradiation. This composition was the thin-film form of the composition whose bulk displayed the highest photo-sensitivity of the glass family $Ge_{23}Sb_7S_{70-X}Se_X$. The thin-film form of the glass enabled the measurement of laser-induced photo-expansion, linear and nonlinear refractive indices, and the modification of the glass matrix. It was determined that the photo-response of the thin films is characterized by a modest photo-expansion on the order of tens of nanometers, a negative refractive index modification of up to -0.05, and a large positive shift of the nonlinear refractive index $(\Delta n_2/n_2) = 1$. The physical mechanism associated with these observed modifications is a rearrangement of the glass network resulting in a shift from linked germanium-based units to isolated GeS_4 tetrahedra accompanied by a decrease in S-S units. This qualitative modification of the bond structure is substantiated by a calculation of the number of the various Ge-containing

bonds as a function of laser irradiation conditions. Through a study of two films of this same composition fabricated by different fabrication techniques, it was discovered that the initial configuration of the glass lattice before irradiation affects the magnitude of photo-induced effects. If the glass has a large number of isolated GeS_4 units, then there is difficult to further increase the density of these units during ablation. In addition, a model of the electron density was used to calculate for the first time the two-photon ionization and avalanche ionization coefficients at 800nm for this material. These studies represent the first published results of laser-induced modifications in this material.

The studies in this chapter also serve the practical purpose of identifying an appropriate substrate material for the first studies of the fabrication of micro-channels in chalcogenide glass by femtosecond laser processing. A desirable substrate exhibits a high photosensitivity characterized by a positive modification of the refractive index and a large density modification (photo-expansion). The positive Δn allows for the direct fabrication of optical waveguides and the density modification affects the etch rate of the material and can be exploited for the fabrication of fluidic structures. The germanium-based film is highly photo-sensitive, but the negative Δn restricts the devices fabricated in it to phase elements such as diffractive optical elements for which the sign of Δn is not important. Because of this, several arsenic-based compositions were characterized. It was determined that the substitution of 5% antimony or germanium in the place of arsenic in the composition As_2S_3 drastically affects the photo-sensitivity of the glass. The antimony-containing glass displayed a large photo-expansion and a negligible Δn, whereas the germanium-containing glass had the opposite trend. The composition

As_2S_3 exhibits a moderate photo-expansion and a positive Δn and was therefore chosen as the substrate material for micro-fluidic element fabrication experiments described in CHAPTER 7.

CHAPTER 7: TOWARDS OPTO-FLUIDIC DEVICE FABRICATION IN CHALCOGENIDE GLASS

This chapter describes the first experiments to our knowledge on the fabrication of micro-fluidic elements in chalcogenide glass using femtosecond laser processing. These studies drive towards the fabrication of an integrated evanescent-wave optofluidic sensor in chalcogenide glass that is functional at infrared wavelengths. Such a device integrates optical elements such as waveguides for light propagation and micro-channels for fluidic or gaseous transport onto a single portable platform to provide IR optical analysis to small sample volumes. A conceptual schematic of the desired device is in two geometries is shown in Figure 7.1.

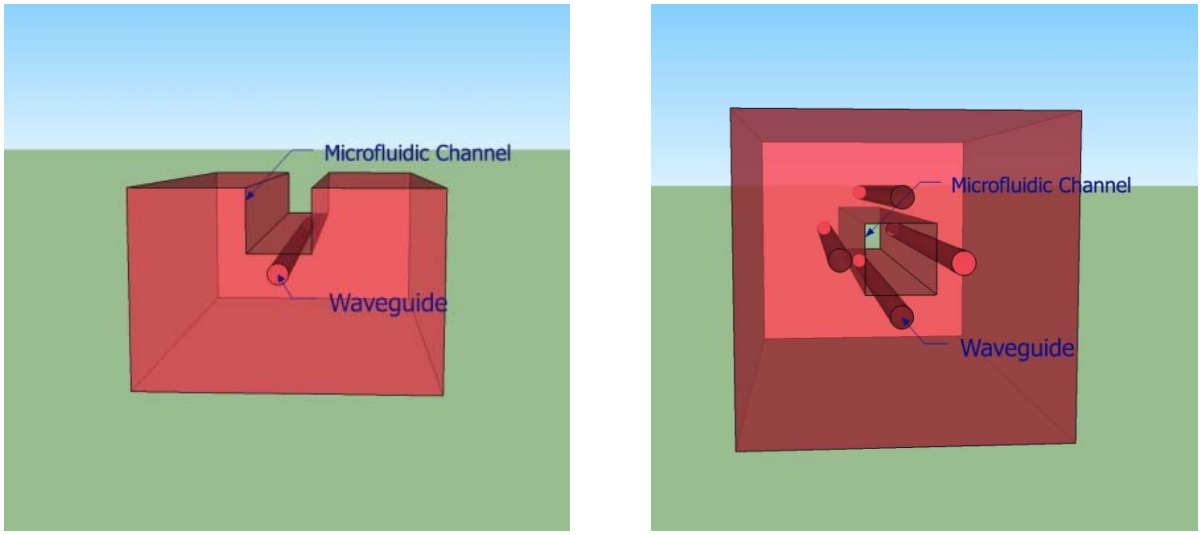

(a) (b)

Figure 7.1: Schematic of an evanescent wave optofluidic sensor consisting of optical waveguides in close proximity to a micro-fluidic channel allowing for evanescent-wave coupling between the optical and fluidic elements. The micro-fluidic channel is located on the surface in (a) and within the volume of the material in (b).

Figure 7.1(a) depicts a surface micro-channel fabricate above an optical waveguide. This geometry is similar to devices fabricated by lithographic methods, but can be fabricated using solely femtosecond laser processing technology. Furthermore, it is comprised of only one material and does not require the multiple processing steps associated with lithography. The surface micro-channel can be encapsulated and sealed by a cap layer in order to allow for the use of flowing fluids. This cap can be fabricated out of either a polymer such as PDMS and bonded to the surface of the bulk glass or out of glass of the same composition and sealed to the surface using femtosecond laser welding. The latter approach is a relatively new technique which would enable higher pressures and increased robustness over polymer cap layer. The device geometry depicted in Figure 7.1(b) is comprised of a buried micro-channel surrounded by buried optical waveguides. The fabrication of a buried channel enables a more efficient use of the substrate material with multiple waveguides simultaneously probing the micro-channel. 3D femtosecond laser processing is uniquely suited for the fabrication of such integrated structures in the volume of a transparent material.

In both device geometries, the microchannel and the optical waveguide are placed in close proximity such that the evanescent field of light propagating in the optical waveguide penetrates the microfluidic channel. By propagating laser light with a wavelength tuned to an absorption peak of a known analyte through the optical waveguide, the presence of the analyte in the microfluidic channel will directly affect the transmitted power of the laser light through the waveguide. In this modality, the absorption of light in the waveguide measured in dB (αL) induced by the presence of the analyte in the microchannel can be related to the transmitted power by[22]:

$$\alpha L = \log_{10} \frac{I_{analyte}}{I_{control}} \tag{36}$$

where $I_{analyte}$ is the transmitted power of the waveguide when the microchannel is filled with the solution under test and $I_{control}$ is the transmitted power of the waveguide when the microchannel is filled with a control solution without the analyte. Sensors of this type are versatile and can be used to detect virtually any analyte with a known well-defined absorption peak using a laser tuned to the appropriate wavelength so long as the analyte is in a gaseous or fluidic form that can flow through the channel.

This chapter contains four sections. The first provides a theoretical description of evanescent fields in optical waveguides and the physical dimensions necessary to fabricate this device in chalcogenide glass. Sections two and three describe the fabrication of micro-fluidic elements using direct laser ablation and selective etching of photo-modified material. The final section describes the fabrication of both an optical waveguide and a surface micro-channel in the same substrate.

7.1. Evanescent Fields in Optical Waveguides

The propagation of an optical mode through a waveguide gives rise to an evanescent field in the cladding layer of the waveguide. This evanescent field exists along the entire length of the waveguide, which can interact with any adjacent element such as a fluidic channel. The amount of power associated with evanescent field is related to the wavelength of light propagating through the waveguide as well as physical properties of the waveguide including the size and Δn.

Two waveguide geometries are discussed: rectangular slab waveguides and circularly symmetric waveguides.

7.1.1. Slab-Type Waveguides

The shape of a waveguide fabricated by femtosecond direct writing is dependent on the focusing optic used during processing. The use of low numerical apertures can lead to waveguides of narrow width (<10μm) and large depth (>75μm), which can be approximated by slab waveguides. Consider the planar slab waveguide structure shown in Figure 7.2.

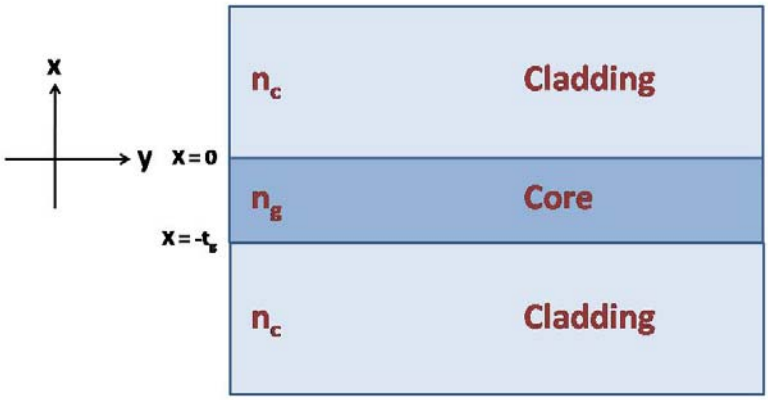

Figure 7.2: Schematic of a slab optical waveguide waveguide

This planar waveguide structure can support two types of fields that satisfy the wave equation: transverse electric (TE) waves in which the electric field normal to the plane of incidence, and transverse magnetic (TM) waves in which the magnetic field lies normal to the plane of incidence. Propagation of either polarization will lead to the formation of an evanescent field.

For TE waves, the wave equation can be written as [178]

$$\frac{d^2E_y}{dx^2} + \left(k_0^2 n_g^2 - k_0^2 n_{eff}^2\right)E_y = 0 \tag{37}$$

in the core region of the waveguide and as

$$\frac{d^2E_y}{dx^2} + \left(k_0^2 n_g^2 - k_0^2 n_{eff}^2\right)E_y = 0 \tag{38}$$

in the cladding region of the waveguide, where n_g is the refractive index of the core, n_c is the refractive index of the cladding, and n_{eff} is the effective refractive index of the guided wave. Although the guided wave exists in regions with different refractive indices, the wave propagates with one common phase constant.

It can be seen that if n_{eff} is larger than the refractive index of the region of interest, than the solution for the electric field is an exponential. Conversely, if the effective index is lower than the refractive index of the region of interest, than the solution for the electric field is sinusoidal. Therefore, in order to satisfy the boundary conditions of a wave at an interface that the component of the electric field tangential to the interface must be continuous, guided modes exist only for $n_g > n_{eff} > n_c$. Thus, the core of the waveguide must have a larger refractive index than the cladding and the propogating modes will experience effective refractive indices in between the two values.

Therfore, the solutions to the wave equation can be written as[178]

$$E_y = Ae^{-k_0\sqrt{n_{eff}^2 - n_c^2}x} e^{-jk_0 n_{eff} z}, x \geq 0 \tag{39}$$

$$E_y = Bcos\left(k_0\sqrt{n_g^2 - n_{eff}^2}x + \phi\right)e^{-jk_0 n_{eff}z}, -t_g < x < 0 \quad (40)$$

$$E_y = Ce^{k_0\sqrt{n_{eff}^2 - n_c^2}(x+t_g)}, -\infty < x < -t_g \quad (41)$$

where A, B, and C are the amplitudes of the waves in each region and ϕ is a phase term, which can be obtained by solving the boundary conditions at $x = 0$ and $x = -t_g$. It is seen that the waves consist of a propagating term in the z-direction with an effective index of n_{eff} and a distribution in x (across the width of the waveguide) that is sinusoidal in the waveguide core and exponential in the cladding that falls off to either side of the waveguide. It is precisely this evanescent field in the cladding regions that is exploited in optofluidic sensors.

A similar approach can be used to solve for the fields of TM polarized waves. As the electric field has components in both the x and z directions, it is more convenient to solve for the magnetic field in the y direction. The allowed solutions for the magnetic field of TM waves through the waveguide are then:

$$H_y = Ae^{-k_0\sqrt{n_{eff}^2 - n_c^2}x}e^{-jk_0 n_{eff}z}, x \geq 0 \quad (42)$$

$$H_y = Bcos\left(k_0\sqrt{n_g^2 - n_{eff}^2}x + \phi\right)e^{-jk_0 n_{eff}z}, -t_g < x < 0 \quad (43)$$

$$H_y = Ce^{k_0\sqrt{n_{eff}^2 - n_c^2}(x+t_g)}, -\infty < x < -t_g \quad (44)$$

A similar evanescent field is seen in the cladding region.

Because waves propagating in an optical waveguide exist in multiple regions and are not completely confined within the core of the waveguide, a portion of the power is carried outside the waveguide core in the cladding region. The relative amount of power within the waveguide core is described by the confinement factor:

$$\Gamma = \frac{\int_{-t_g}^{0} |E|^2}{\int_{-\infty}^{\infty} |E|^2} \tag{45}$$

Alternatively, the power associated with the evanescent field in the waveguide cladding available for interaction with surrounding media can be described as $1 - \Gamma$.

7.1.2. Circularly Symmetric Waveguides

Optical waveguides fabricated by a focusing optic with either a high numerical apertures or a designed astigmatism can produce waveguides with a nearly circular profile that are more to an optical fiber than a slab waveguide. Consider an optical waveguide with a geometry described in Figure 7.3.

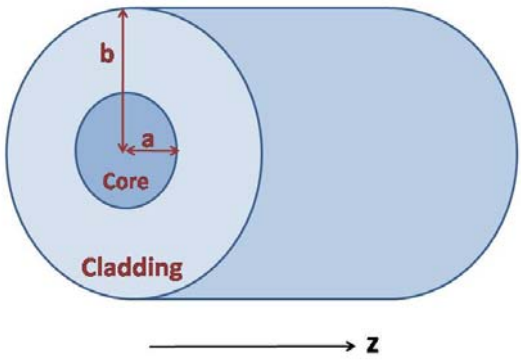

Figure 7.3: Schematic of a circularly symmetric optical waveguide

To describe the propagation of light through a circularly symmetric waveguide such as an optical fiber or a waveguide fabricated through femtosecond laser direct writing, it is easiest to consider first the wave equation in the z-direction and find the other field components in terms of E_z and H_z.

$$\nabla E_z + k^2 E_z = 0 \tag{46}$$

$$\nabla H_z + k^2 E_z = 0 \tag{47}$$

where the form of the wave propagating in the z-direction can be described as:

$$E = E(r, \phi) e^{-j\beta z} \tag{48}$$

$$H = H(r, \phi) e^{-j\beta z} \tag{49}$$

In cylindrical coordinates, the Laplacian operator takes the form:

$$\nabla^2 = \frac{\partial^2}{\partial r^2} + \frac{1}{r}\frac{\partial}{\partial r} + \frac{1}{r^2}\frac{\partial^2}{\partial \phi^2} + \frac{\partial^2}{\partial z^2} \tag{50}$$

It can then be shown that[179]:

$$\frac{\partial^2}{\partial r^2} E_z + \frac{1}{r}\frac{\partial E_z}{\partial r} + \left(k^2 - k_0^2 n_{eff}^2 - \frac{\ell^2}{r^2}\right) E_z = 0 \tag{51}$$

$$\frac{\partial^2}{\partial r^2} H_z + \frac{1}{r}\frac{\partial H_z}{\partial r} + \left(k^2 - k_0^2 n_{eff}^2 - \frac{\ell^2}{r^2}\right) H_z = 0 \tag{52}$$

These equations are Bessel differential equations and have solutions and the solutions are Bessel functions with order ℓ. Practically, the order ℓ relates to the mode propagating through the fiber.

Just as for slab waveguides shown in the previous section, the form of the solutions of these equations is dependent on the refractive index of the region of interest. If the refractive index of the region of interest is higher than the effective index of the mode, the term $k^2 - k_0^2 n_{eff}^2 > 0$ and the solutions to equation (51) are of the general form[179]:

$$\Psi = aJ_\ell\left(k_0\sqrt{n_g^2 - n_{eff}^2}r\right) + bY_\ell\left(k_0\sqrt{n_g^2 - n_{eff}^2}r\right)$$

where J_ℓ and Y_ℓ describe Bessel functions of the first and second kind with order ℓ and a and b are amplitude constants. The Bessel functions of the first and second kind oscillate and are similar to a damped sinusoidal function. Alternatively, if the refractive index of the region of interest is lower than the effective index, than the term $k^2 - k_0^2 n_{eff}^2 < 0$ and equation (51) has solutions of the form[179]:

$$\Psi = aI_\ell\left(k_0\sqrt{n_{eff}^2 - k^2}r\right) + bK_\ell\left(k_0\sqrt{n_{eff}^2 - k^2}r\right) \tag{53}$$

where I_ℓ and K_ℓ are modified Bessel functions of the first and second kind with order ℓ and a and b are amplitude constants. The modified Bessel functions are increasing and decreasing functions, respectively, that are similar to the exponential function.

Just as for slab waveguides, a guiding mode within the optical fiber must satisfy the boundary conditions for the interface between core and cladding. Thus, the conditions for a guided mode are $n_g > n_{eff} > n\_c$, which is the same as for slab waveguides, and only the Bessel functions that are defined at 0 are considered. The electric and magnetic fields are then described as[179]:

$$\mathrm{E_z} = AJ_\ell\left(k_0\sqrt{n_g^2 - n_{eff}^2}r\right)e^{-j(k_0 n_{eff}z-\ell\phi)} \tag{54}$$

$$\mathrm{H_z} = BJ_\ell\left(k_0\sqrt{n_g^2 - n_{eff}^2}r\right)e^{-j(k_0 n_{eff}z-\ell\phi)} \tag{55}$$

in the core region and

$$\mathrm{E_z} = CK_\ell\left(k_0\sqrt{n_{eff}^2 - k^2}r\right)e^{-j(k_0 n_{eff}z-\ell\phi)} \tag{56}$$

$$\mathrm{H_z} = DK_\ell\left(k_0\sqrt{n_{eff}^2 - k^2}r\right)e^{-j(k_0 n_{eff}z-\ell\phi)} \tag{57}$$

in the cladding region. This solution has the same general form as for slab waveguides with the addition of circular symmetry. The fields are oscillatory in the waveguide core and decaying in the cladding. The equations can be completely solved for the individual modes by applying the boundary conditions at the core/cladding interface.

Just as for the slab waveguides, the optical modes propagating through the fiber exist in both the core and cladding regions and thus a portion of the optical power is contained within the cladding region and the relative power confined within the core is a critical parameter. The confinement factor of optical fibers is described as[179]:

$$\Gamma = \frac{P_{core}}{P_{total}} = \frac{\int_0^{2\pi}\int_0^a S_z r dr d\phi}{\int_0^{2\pi}\int_0^\infty S_z r dr d\phi} = \left(\frac{n_{eff}^2 - n_c^2}{n_g^2 - n_c^2}\right)\left(1 - \frac{J_\ell^2\left(k_0\sqrt{n_g^2 - n_{eff}^2}a\right)}{J_{\ell-1}^2\left(k_0\sqrt{n_g^2 - n_{eff}^2}a\right) + J_{\ell+1}^2\left(k_0\sqrt{n_g^2 - n_{eff}^2}a\right)}\right) \tag{58}$$

The power confined in the cladding layer is described as $1 - \Gamma$.

7.1.3. Application to Opto-fluidics

The evanescent fields associated with light propagating through optical waveguides and the confinement factor describing the relative power affects the design requirements for the fabrication of the opto-fluidic sensor shown in Figure 7.1. The performance of such a sensor increases with increasing overlap of optical power in the micro-fluidic channel and thus the fabrication challenge is to fabricate the optical and fluidic components such that this overlap is maximized. This involves maximizing the power associated with evanescent fields while maintaining low-loss propagation of the light (characterized by the value $1 - \Gamma$). The confinement factor, shown in equations (45) and (58), is reduced by minimizing the waveguide size as well as the refractive index step between the core and cladding (Δn). Figure 7.4 and Figure 7.5 show the dependence of $1 - \Gamma$ as a function of the waveguide size and Δn, respectively. The substrate glass used in these calculations is arsenic trisulfide, which is the composition used for experimental investigations of micro-channels via femtosecond laser processing throughout this chapter. The laser wavelength used in the calculation is 1.5μm.

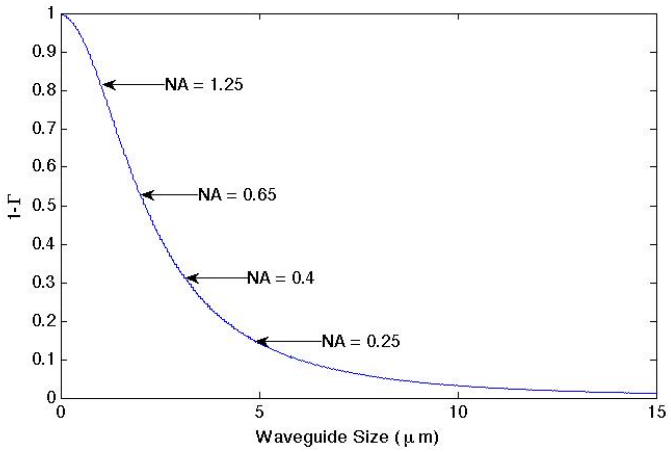

Figure 7.4: Calculation of $1-\Gamma$ for an optical waveguide in arsenic trisulfide with $\Delta n = 5x10^{-3}$as a function of the waveguide size. The spot sizes of microscope objectives with varying numerical apertures calculated for $\lambda = 1043nm$ are identified on the plot.

The value of $1-\Gamma$ rapidly decreases with increasing waveguide size, reaching values of less than 10% for waveguides larger than 5μm. The dimension of waveguides fabricated using femtosecond laser processing is generally equal to the size of the focal volume since this is the region of highest irradiance and thus the strongest nonlinear absorption of laser light. For transverse writing, where the sample is translated orthogonally to the direction of the beam, the width of the waveguide is approximately equal to the spot size of the focused beam. The values of spot sizes calculated for different numerical apertures ($\lambda = 1043nm$) are shown in Figure 7.4. For a waveguide with $\Delta n = 5x10^{-3}$, a numerical aperture greater than 0.65 is necessary to produce a value of $1-\Gamma > 0.5$. The use of lower numerical apertures results in high confinement of 1.5μm light.

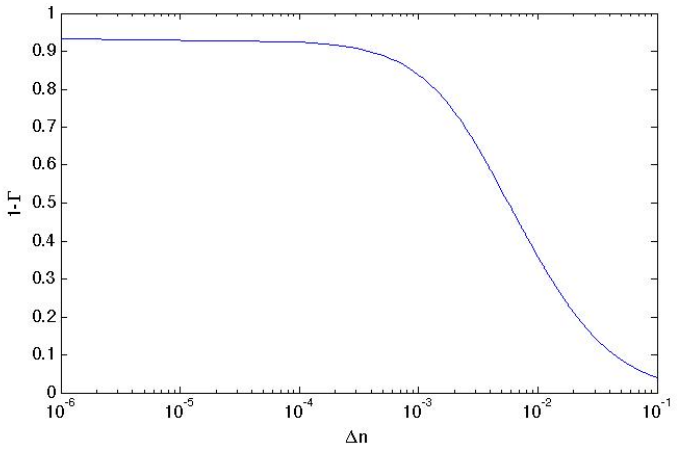

Figure 7.5: Calculation of $1-\Gamma$ for a 2µm optical waveguide in arsenic trisulfide as a function of Δn

The value of $1-\Gamma$ has a sharp dependence on the Δn of the waveguide. Considering a 2µm waveguide, which is fabricated using a 0.65NA microscope objective, $1-\Gamma$ is larger than 0.9 for $\Delta n < 10^{-3}$, but decreases to 0.3 for $\Delta n = 10^{-2}$. For this composition, $\Delta n = 10^{-3}$ is ideal as it provides a large value of $1-\Gamma$ yet is still large enough to produce a high-quality waveguide.

In addition to the value of $1-\Gamma$, the separation of the waveguide and the micro-channel affects the percentage of the power that overlaps the microchannel (see Figure 7.6). The waveguide parameters associated with this calculation was 2µm wide with a $\Delta n = 1e^{-3}$, which are practical values that achieve a high performance. Under these conditions, the power in the channel decreases by roughly 5% per micron of separation.

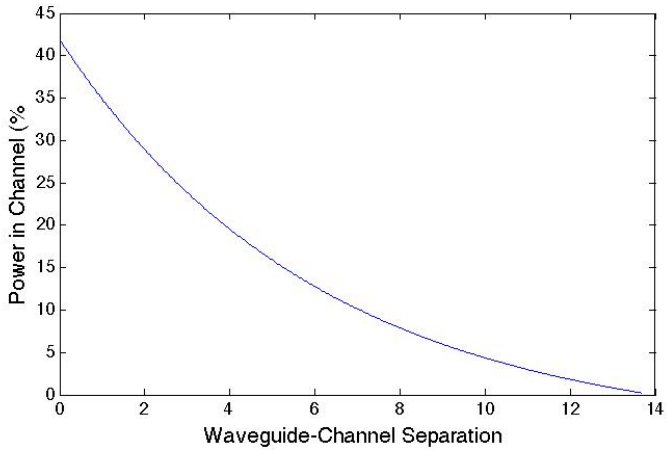

Figure 7.6: Calculation of the percentage of power overlapping a waveguide parallel to a 2μm waveguide with $\Delta n = 5x10^{-3}$ as a function of the separation distance

7.2. Micro-fluidic Channel Fabrication by Direct Ablation

The first technique explored for the fabrication of micro-channels was through direct ablation of the material surface. The composition $As_{36}Sb_6S_{58}$ was chosen for this portion of the study as this glass displayed a minimal photo-expansion upon exposure to femtosecond laser pulses, which is preferable as a large photo-expansion would interfere with the ablation profile. The laser used for the fabrication of the micro-channels is a fiber-based Yb:YAG laser from IMRA Corporation described in section 3.4.3 with a repetition rate of 4MHz. The 4MHz repetition rate was chosen as a minimal pulse energy was desired. The laser was focused to a spot size of 5μm on the surface of the sample with a 0.25NA (10X) microscope objective. Patterning was achieved by mounting the sample on a computer-controlled 3D translation stage (VP-25XA, Newport).

Before fabricating micro-channels, it is necessary to determine the threshold for surface laser ablation at the appropriate number of pulses per laser spot. The ablation threshold was

determined by fabricating a series of lines of varying intensity, each with the number of pulses per focal spot held constant at $2.6x10^5$. The ablation threshold defined for the purpose of this study was the laser irradiance at which material was ejected resulting in a trench and was determined by measuring the surface profile of the films after irradiation using the Zygo NewView 6300 3D Optical Profiler. For $As_{36}Sb_6S_{58}$, the ablation threshold was determined to be 61 GW/cm^2.

A channel width of 20μm was achieved by writing 20 parallel lines spaced 1μm apart, which was one fifth of the focused beam size and ensured a uniform irradiation along the entire width of the channel. The writing speed for all micro-channels was set to 100μm/s, which corresponds to $2.6x10^5$ pulses per laser focal spot and was the same speed used for the determination of the ablation threshold.

Figure 7.7 shows a contour map and a surface profile of a micro-channel fabricated as described above with 20 parallel lines spaced by 1μm. Each line was written 10 ten times over with the laser before a subsequent line was written to ensure uniform irradiation of each line and remove as much debris as possible from the irradiated region. The laser irradiance was set to 63.6GW/cm2 (7.2nJ), corresponding to 3% above the ablation threshold of the material. The surface profile of the micro-channel was measured using the Zygo 3D Optical Profiler.

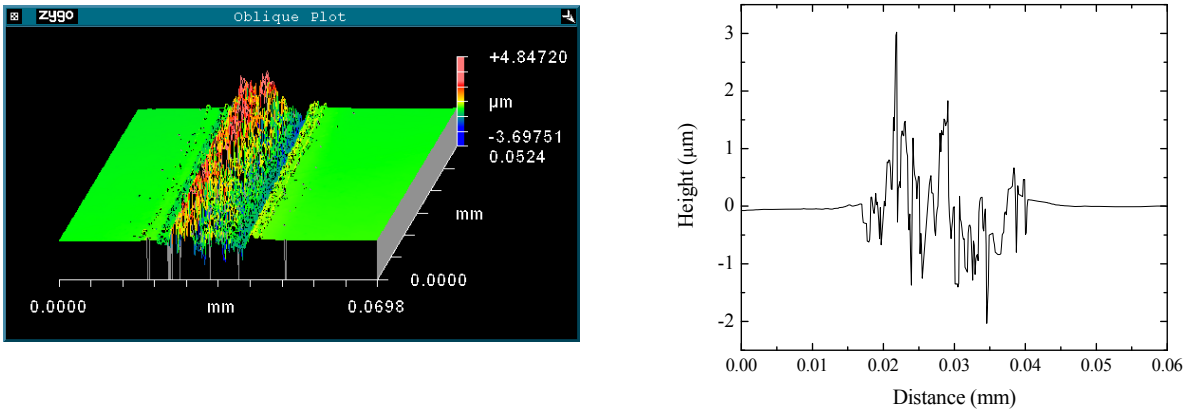

(a) (b)

Figure 7.7: Contour map (a) and surface profile (b) of surface micro-channel formed by 20 parallel lines spaced by 1µm taken with a Zygo 3D Optical Profiler.

This fabrication process resulted in a micro-channel with a severely non-uniform depth, varying from 2µm below the surface to 3µm above the surface. According to the orientation of the image, the first ablated line was on the right side of the micro-channel and the last was on the left. From both (a) and (b) of Figure 7.7, it is clear that the right half of the micro-channel is characterized by ablation, while the left half often rises above the sample surface. It is thought that debris from the initial ablated lines on undamaged material ejects debris that interferes with ablation in the second half of the micro-channel. However, the depth of the micro-channel on the right half is only roughly 1µm and is not deep enough to see a clear trend. Therefore, a second deeper micro-channel was fabricated.

To accomplish this, four layers of 20 parallel lines were written into the material with each layer 3µm deeper into the material than the previous layer. The laser irradiance was held to

63.6GW/cm^2 (7.6nJ), corresponding to 3% above the ablation threshold, and the number of laser passes per line was reduced to 6. The contour map and surface profile of the micro-channel is shown in Figure 7.8.

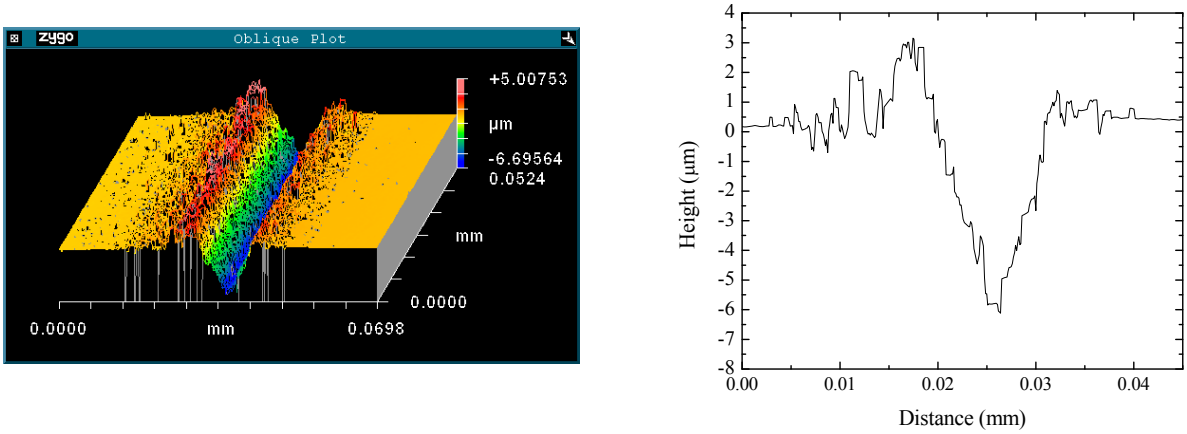

(a) (b)

Figure 7.8: Contour map (a) and surface profile (b) of surface micro-channel formed by 4 layers of 20 parallel lines spaced by 1µm taken with a Zygo 3D Optical Profiler. Each layer is spaced by 3µm.

A micro-channel with a maximum depth of 6µm can be seen. Considering that the laser was focused up to 12µm below the surface, the maximum depth of the channel is roughly half of the expected depth. Furthermore, as seen in Figure 4.1, the profile of the micro-channel is non-uniform with ablation on the right and increased material above the surface on the left. The width of the ablated region, measured at the point where the profile dips below the surface, is 10µm. In addition, debris is clearly visible both inside and outside of the micro-channel. These observations confirm that debris generated by the first lines on the undamaged surface impede subsequent ablation and limit the size of the micro-channel in both height and depth. However,

this micro-channel has a similar size and shape as surface channels fabricated in silica glass [70] and could be used to hold liquid via the capillary force.

Although this channel served as a proof of concept and a demonstration of the ability to fabricate a simple channel through direct ablation, the imperfect ablation led to a further investigation of the effect of increasing the laser irradiance. Figure 7.9 shows a micro-channel was fabricated with seven layers of 20 parallel lines with a decreased layer separation of 1μm and an irradiance of 66.6GW/cm2 (7.6nJ), corresponding to 8% above the ablation threshold. As before, each line was written six times over before proceeding to the subsequent line.

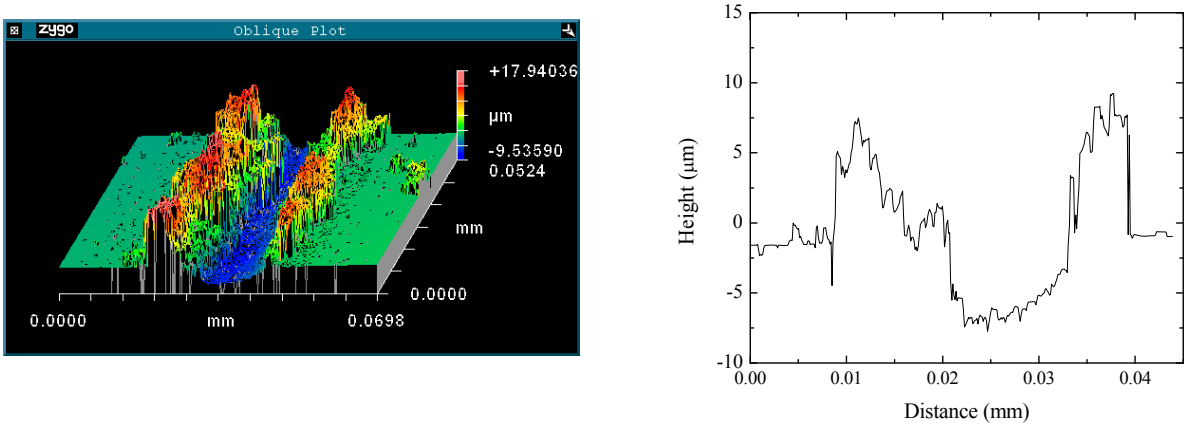

(a) (b)

Figure 7.9: Contour map (a) and surface profile (b) of surface micro-channel formed by 7 layers of 20 parallel lines spaced by 1μm taken with a Zygo 3D Optical Profiler. Each layer is spaced by 1μm.

The increased irradiance and smaller layer spacing resulted in a wider micro-channel at the expected depth of ~8μm. However, a combination of photo-expansion and debris deposits on the sides of the channels result in an increased sidewall roughness and irregularity compared

to Figure 7.8. In addition, the height of the sidewalls is roughly 10μm above the surface and would impair the addition of a cover plate on top of the micro-fluidic channel.

The results of the fabrication of these wide channels with varying laser parameters indicate that a combination of the presence of a large photo-expansion adjacent to ablated regions and a large debris formation hinders the fabrication of wide microchannels through direct ablation. In order to isolate and investigate these issues without the cumulative effects of a wide channel, a series of single track channel arrays were written with varying number of laser passes per track. All of the channels in this series were fabricated using a laser irradiance of 63.6GW/cm^2 (8% above the ablation threshold) with the number of passes per line from 2 to 10. Figure 7.10 - Figure 7.12 shows the surface profiles of a series of micro-channel arrays written with 2, 6 and 10 number of passes per line, respectively. As with the wide micro-channels, the laser was focused with a 0.25NA objective and the number of pulses per focal spot was 2.6x10^5. In each array, the microchannels were separated by 20μm.

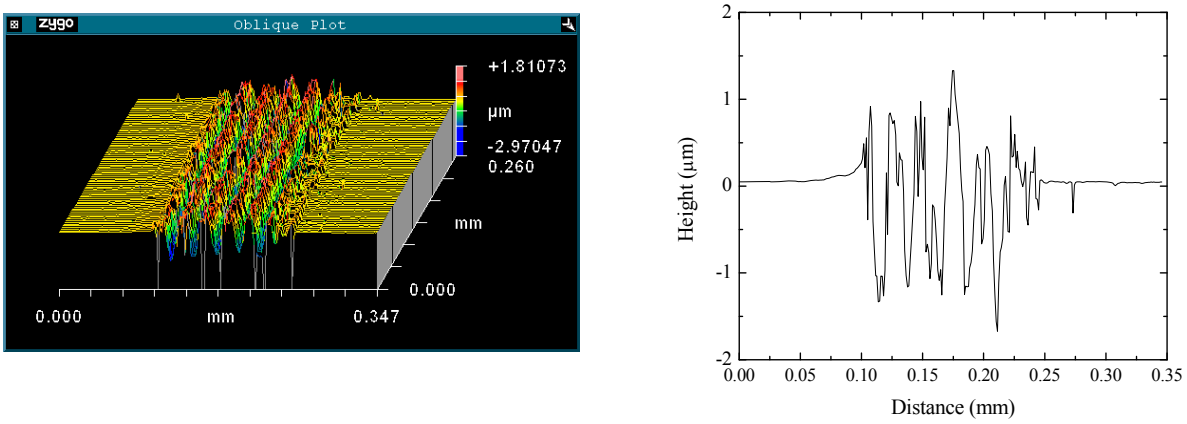

(a) (b)

Figure 7.10: Contour map (a) and surface profile (b) of parallel micro-channels spaced by 20µm taken with a Zygo 3D Optical Profiler. Each channel was formed by 2 passes of the laser.

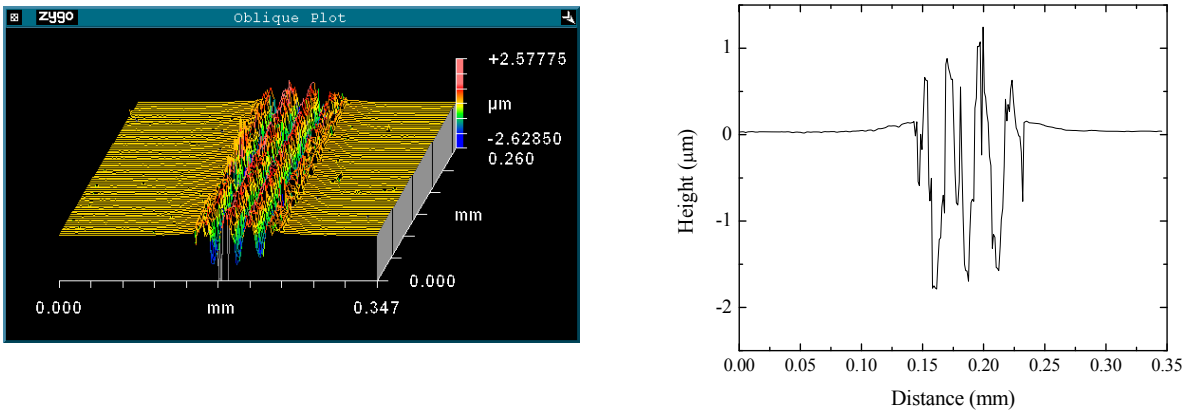

(a) (b)

Figure 7.11: Contour map (a) and surface profile (b) of parallel micro-channels spaced by 20µm taken with a Zygo 3D Optical Profiler. Each channel was formed by 6 passes of the laser.

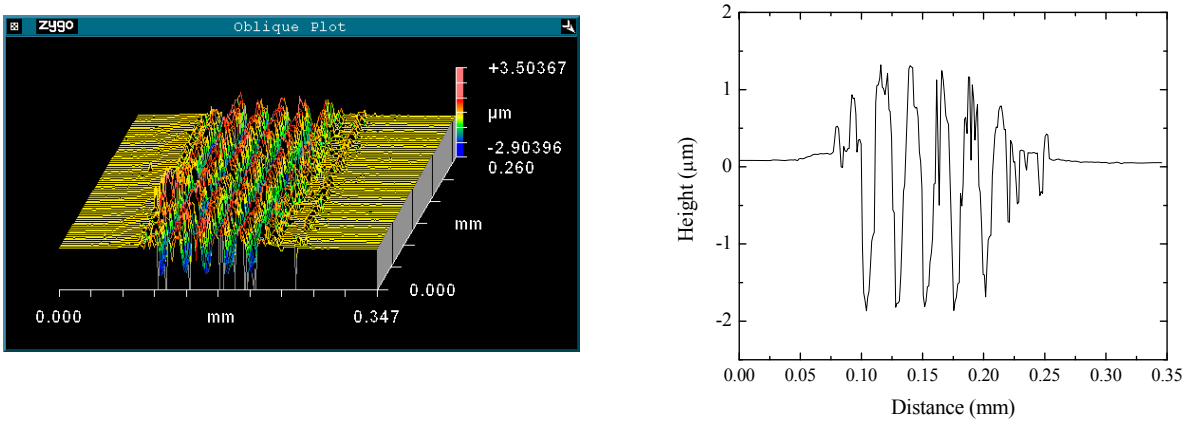

(a) (b)

Figure 7.12: Contour map (a) and surface profile (b) of parallel micro-channels spaced by 20µm taken with a Zygo 3D Optical Profiler. Each channel was formed by 10 passes of the laser.

There are several observations from Figure 7.10- Figure 7.12:

- The depth of ablation increases from ~1.25µm to ~2µm as the number of laser passes increases from 2 to 10.
- Increasing the number of laser passes also increases the consistency of the ablation depth for multiple channels. This suggests that passing the laser over the line several times indeed helps to clear debris formed by previous ablated lines and results in the optimum ablation depth.
- The height of the material between the ablated lines is seen to be higher than the surface for all three figures and is formed by a combination of photo-expansion and deposition of ablated material. The height of this photo-expansion increases from ~1µm to ~1.25µm and becomes increasingly repeatable with an increasing number of laser passes. It is thought that this photo-expansion is caused by the Gaussian spatial distribution of the laser. This spatial distribution results in a high irradiance in the center of the beam that causes ablation and a lower irradiance on the edge of the beam that induces photo-expansion. The observation of photo-expansion in chalcogenides induced by near-IR femtosecond laser irradiation with a laser irradiance below the ablation threshold is well documented [51, 59, 61].

Although the depth of ablation is made increasingly repeatable by increasing the number of laser passes, the surface profiles are not smooth and that the generation of debris is not yet optimized under these laser conditions. The optimal solution is to optimize the laser parameters such that the material is efficiently ionized during ablation and large debris particles are not formed. One way to do this is through a variation of the laser repetition rate, which determines the temporal separation between laser pulses. If the temporal separation between pulses is shorter than the timescale of the diffusion of heat from the laser focal volume, then energy accumulates within the laser focal volume as the number of pulses per focal spot increases. Thus, increasing the repetition rate of the laser increases the rate of energy accumulation in the focal volume and decreases the pulse energy of individual pulses necessary to induce ablation.

The significant debris formation in microchannels fabricated by direct ablation can be mitigated by reducing the pulse energy of the laser pulses accompanied by an increase of the laser repetition rate. Figure 7.13 shows the surface profile of a single micro-channel written with 61GW/cm^2 (0.3nJ) pulses with a 26MHz home-build Ti:Sapphire laser oscillator. The number of pulses per spot was 63x10^3.

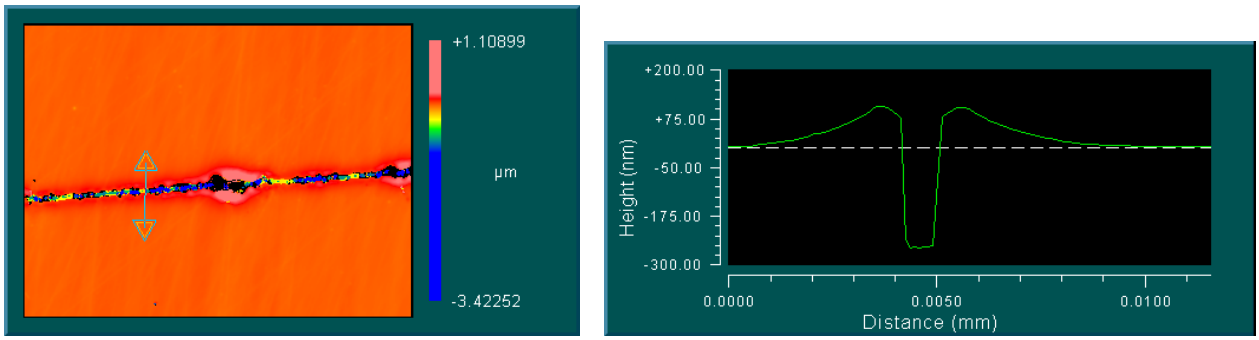

(a) (b)

Figure 7.13: Contour map (a) and surface profile (b) of surface micro-channel fabricated with 0.3nJ pulses at a repetition rate of 26MHz taken with a Zygo 3D Optical Profiler.

The micro-channel produced in this regime has a similar profile to the higher pulse energy regime, namely an ablated micro-channel surrounded by photo-expanded sidewalls. However, the lower pulse energy results in a cleaner ablation with less debris formation. This is a promising result towards the optimization of laser parameters for the direct ablation of micro-channels in $As_{36}Sb_6S_{58}$. It is interesting to note that the presence of photo-expansion on the edges of the ablated regions was not present in the thin film irradiation study described earlier. As stated previously, this composition, $As_{36}Sb_6S_{58}$, was specifically chosen for this experiment as there was no observable photo-expansion. This result points to the difference between the molecular bond structure of the bulk material relative to thin films.

7.3. Selective Etching of Laser Photo-modified Material

The selective etching of laser-modified material is an alternative technique for the fabrication of fluidic elements that eliminates complications due to ablation and the formation of debris. The most prominent application area to date for the use of selective etching of photo-modified

chalcogenide glasses has been for the development of chalcogenide photoresists (ChPs) for photo-lithography. Fabrication of ChPs in this manner consists of irradiating a thin film with either an Argon laser [180], a UV source[181], or a halogen lamp[182-184] and subsequent wet etching. Depending on the irradiation source, either laser direct writing or exposure through a mask can be used to pattern the film. Examples of optical elements fabricated using this technique include rib waveguides [174, 181, 185, 186], diffraction gratings [184, 187-189], crossed diffraction gratings or photonic crystal structures [188, 190, 191], microlens arrays [180, 182, 183, 192-194], and Fresnel lenses[188, 195]. This section describes efforts towards the fabrication of both surface and buried structures using this technique. Based on the study of the photo-response of various chalcogenide glass compositions described in section6.2, the composition $As_{42}S_{58}$ has been chosen for these initial investigations.

An appropriate choice of solvent is critical for obtaining a good contrast ratio for the developing process. Many solvents have been used to etch chalcogenide glasses including piranha solution (a mixture of hydrogen peroxide and sulfuric acid)[196], various amines[192, 195, 197, 198], sodium hydroxide[180, 199], potassium hydroxide[183], ammonium hydroxide[174], and ammonium sulfide[192, 199]. However, the dissolution contrast (defined as the ratio of the dissolution rates of exposed and unexposed regions of the sample) of any given solvent depends considerably on the exact molecular structure before and after irradiation, which is dependent on the composition as well as the film elaboration technique. For example, the dissolution contrast for As-rich films is higher for positive etching, whereas S or Se-rich films exhibit more selectivity in a negative etching process[188]. For arsenic-based glasses, amine-based solutions,

potassium hydroxide and ammonium sulfide are commonly used solvents. Solutions of KOH and propylamine were chosen as developers in this dissertation.

Two different material processing regimes are under investigation for the fabrication of fluidic elements: a low and high heat accumulation regime. In femtosecond laser machining, two laser parameters are critical in controlling thermal effects. The ultrashort pulse duration deposits energy into the material through the generation of a plasma on a timescale shorter than the electron-phonon interaction time. This results in a very low heat affected zone (HAZ), which is exploited in the fabrication of precise features. The time separation between pulses is associated with the degree of heat accumulation within the focal region of the beam. When the time separation between pulses is shorter than the thermal diffusion time of heat from the focal volume, then the focal volume will be a heat source within the material. Investigations of low (kHz) and high (MHz) repetition rate processing in previous chapters indicate that the induced photo-modification of chalcogenide glasses differs greatly between these two regimes. Specifically, little or no observable photo-modification of the material is seen for irradiation with kHz repetition rate pulses, while a large photo-modification evidenced by a volume change and a refractive index change is seen for irradiation with MHz repetition rate pulses. In this section, the role of these photo-modifications on the selective etch rate of photo-modified material is discussed.

7.3.1. Low Repetition Rate Processing

The laser used for low heat accumulation processing was the IMRA μ-Jewel system described in section 3.4.3.

7.3.1.1 Surface Relief Structures

The laser was focused on to the surface of the sample using a 0.3NA microscope objective. Large area square-shaped features with side dimensions of 200 μm were fabricated on the material using pulse energies varying from 20-30nJ. The large are was formed by scanning a series of parallel lines separated by 2μm. The translation speed of the stage was set to 500μm/s for all irradiations in this study. The material ablation threshold, defined as the pulse energy at which direct ablation occurs at this speed under these focusing conditions, was 30nJ. Thus, physical damage was seen for the square written with 30nJ. Surface relief features of this shape act as fluid reservoirs in the microfluidic circuit.

As expected, irradiation of this material with a 100kHz repetition rate resulted in a very small photo-expansion of the surface. For a pulse energy of 27.5 nJ, a photo-expansion of 15nm was observed. For smaller pulse energies, no photo-expansion was observed.

The bulk glass was immersed in a 1 mol% solution of Diisopentylamine in Dimethylsulfoxide as described in previous works [200, 201]. In the previous work, this solvent was used to as a negative developer for a thin film of As_2S_3. The effect of femtosecond irradiation (also using low repetition rate pulses) in these films was primarily to rearrange the As_6S_6 cage molecules found primarily in films to a structure more similar to the original bulk glass. As the study presented here is on the bulk glass, we were primarily interested in directly comparing the response of the irradiated bulk to the irradiated film under similar exposure conditions. However, no change in surface topology was observable with a Zygo 3D Optical Profiler after 35 minutes of etching. The sample was then placed in a 2mol% solution for 30 additional minutes,

also with no observable change of the surface profile. Since no observable change could be seen in the bulk material after 65 minutes in this solvent and 20 minutes was sufficient to completely selectively etch the photonic crystal in a thin film, it was concluded that the weak amine molecule used is not appropriate bulk etching. Therefore, potassium hydroxide, a much more aggressive base, was used as a developer. As seen with thin film chalcogenide photoresists, the KOH acted as a positive developer for this bulk material and selectively etched the irradiated regions. A plot of the etch depth as a function of time in the solution of a reservoir fabricated with 27.5 nJ pulses is given in Figure 7.14. This pulse energy is about 92% of the ablation threshold and is practically the maximum pulse energy that can be reliably used to induce photo-modified material without any ablation since surface or material inhomogeneities will tend to ablate for higher pulse energies.

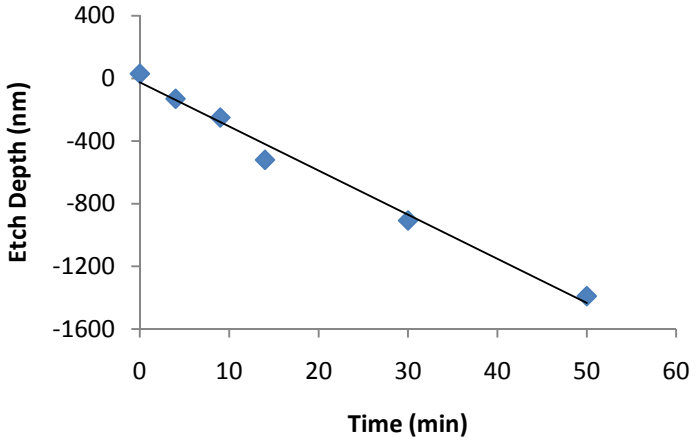

Figure 7.14: Etch depth as a function of time for microfluidic reservoir fabricated with 27.5nJ pulses at a 100kHz repetition rate. The solvent is 0.1M KOH.

The differential etch depth as a function of time is 24nm/min under these conditions. While this is not a description of the actual dissolution contrast (the ratio of the actual etch rate of the

irradiated zone to the un-irradiated area), it does provide a measure of the final channel dimension, which is the most important diagnostic. The etch depth for several other channels fabricated with different pulse energies below the ablation threshold is given in Table 7.1.

Table 7.1: Selective etch rate modification of surface reservoirs fabricated using kHz repetition rate pulses as a function of pulse energy.

Pulse Energy (nJ)	Selective Etch Rate (nm/min)
20	10
25	19
27.5	24

The dependence of the etch rate on the femtosecond laser pulse energy corresponds to the known relationship between pulse energy and the induced photo-modification. This data demonstrates for the first time the selective etching based on femtosecond laser photo-modification bulk chalcogenide glass. The surface profile of the reservoir fabricated with a pulse energy of 27.5nJ after 30 minutes of etching is shown in Figure 7.15.

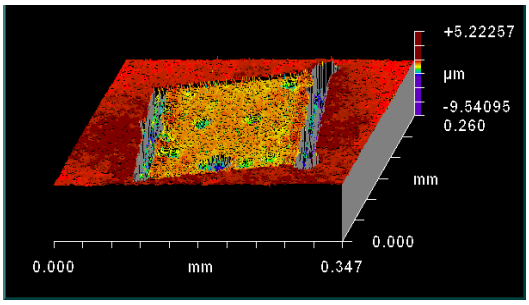

Figure 7.15: Surface Profile of 200µm x 200µm reservoir written with 27.5 nJ of pulse energy after being immersed in 0.1M KOH for 30min.

There are several different observations that we can make regarding the quality of the selective etching process. First, the horizontal transition between the top and bottom surface is ~800nmm,

indicating a sharp contrast between irradiated and un-irradiated regions. Second, the surface roughness of the etched trench as well as the unexposed material are on the order of 400nm, which is roughly ten times higher than the surface roughness before etching. Third, several pits with depths on the order of 2μm are present on the bottom surface of the reservoir. These pits may be due to either material inhomogeneities or variations in the material irradiation. Fourth, a deeper profile is seen on two edges of the structure where the stage slowed and changed direction during fabrication. This suggests a strong dependence of the etch rate on laser dose in addition to the pulse energy. The acceleration and deceleration of the stage during processing cannot be avoided, but cleaner structures could be fabricated by the use of a mechanical shutter to allow surface irradiation only when the translation stage is moving at the desired speed.

The structures fabricated with pulse energies above the ablation threshold displayed a notably different response to the solvent. For a pulse energy of 30 nJ, which is at the ablation threshold, the sample was physically damaged, but material was not ejected. A cross section of the surface profile of the square before etching (a), after 14 min in 0.1M KOH (b), and after 50 min in 0.1M KOH (c) is shown in Figure 7.16.

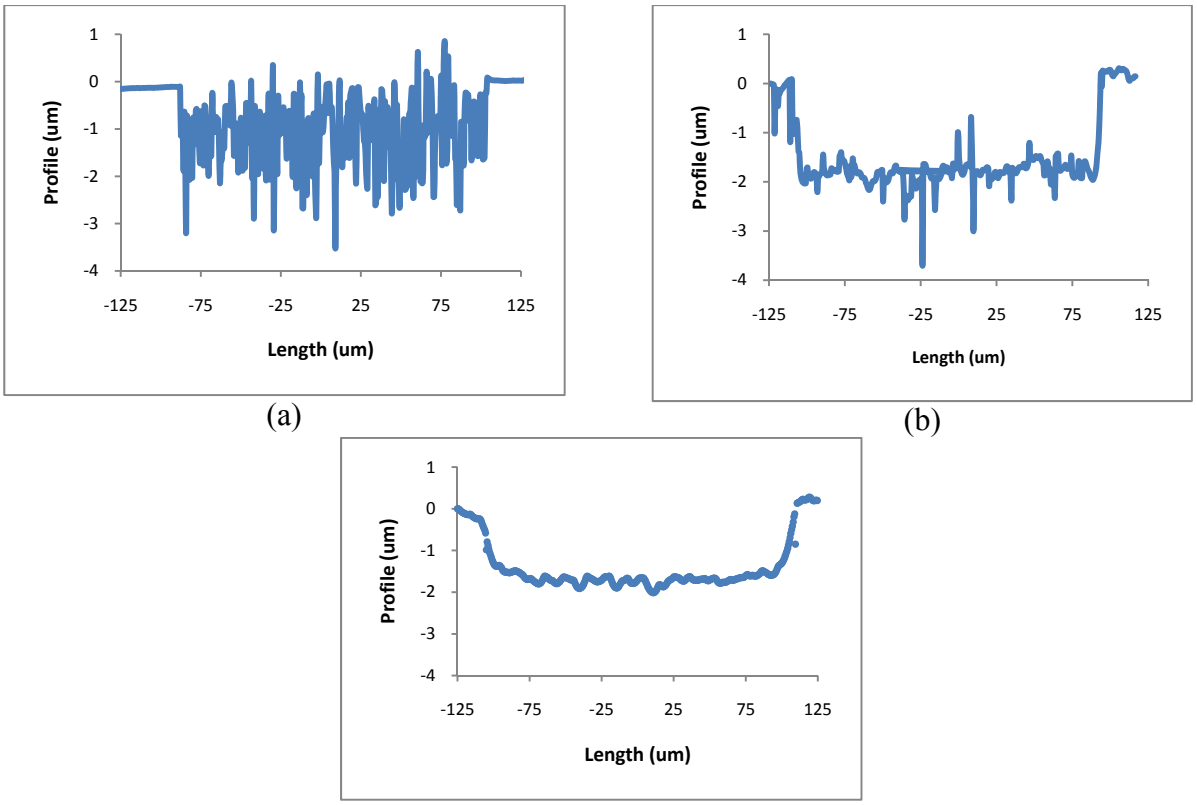

Figure 7.16: Surface profiles of square written with 30nJ pulses and etched for (a) 0 s, (b) 14 min, and (c) 50 min

Immersing the sample in the KOH etchant led to a "smoothing" of the damaged structure. Unlike irradiation below the threshold, the average depth of the ablated region did not change with increased etching time, but the bottom surface of the square was smoothed out to a roughness of ~200nm. The observation that the etch time did not affect the reservoir depth but only the smoothness suggests that this irradiation at the ablation threshold only produced physical damage and did not induce photo-modification of material. The selective etching of the damaged areas is thought to be due to the increased surface area in that region.

7.3.1.2 Buried Microchannels

The potential for the fabrication of buried microchannels was also investigate using 100kHz repetition rate pulses. In this experiment, longitudinal photo-modified lines were written through the ~2mm thickness of the glass with pulse energies ranging from 37.5 to 450 nJ. The translation speed of the stage was set to 500μm/s in all cases.

As seen with the surface reservoir fabrication, immersing of the glass in a 0.1M KOH solution resulted in differential etching of the longitudinal channels. For buried channels such as these, the ultimate goal is to maximize the aspect ratio, which is the ratio of the channel depth to the channel width, in order to fabricate long channels within the volume of the material. The etch depth of the channels as a function of the laser pulse energy is given in Figure 7.17.

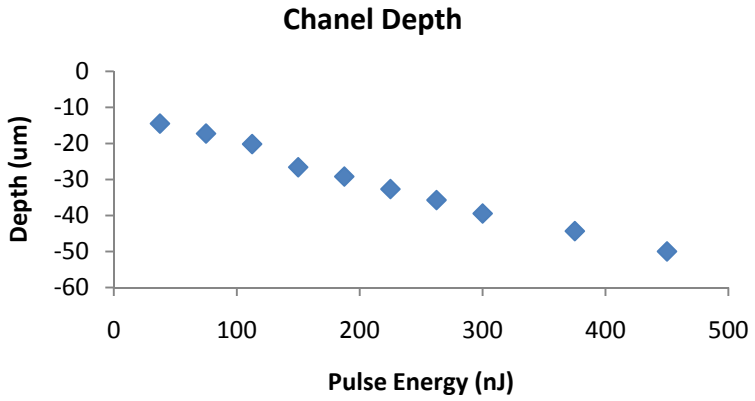

Figure 7.17: Etch depth of micro-channels as a function of pulse energy

The linear dependence of the etch depth on the pulse energy agrees with the results seen for the reservoirs and indicates that the femtosecond laser modification is directly modifying the etch

rate of the material. However, the aspect ratio of the channels was extremely poor, ranging from 0.3:1 to 0.35:1 for increasing pulse energy.

7.3.2. High Repetition Rate Structuring

Surface features and buried microchannels are investigated using MHz repetition rate pulses in order to investigate the effect of heat accumulation on the femtosecond laser induced modification of the etch rate of $As_{42}S_{58}$. Two different lasers have been used for MHz experiments, a 26MHz extended cavity Ti:Sapphire oscillator and a 1.5MHz fiber laser.

7.3.2.1 Surface Relief Features

Surface microchannels have been fabricated on bulk $As_{42}S_{58}$ using an extended cavity Ti:Sapphire oscillator. This laser produces 800nm pulses with a pulse duration of ~65 fs at a repetition rate of 26MHz. The laser was focused onto the surface of the sample using a 0.25NA (10X) microscope objective and a series of single track features were created at with a varying number of pulses per focal spot. The pulse energy used was 0.17nJ, which was ~90% of the ablation threshold under these conditions. After irradiation, the samples were placed in an aqueous solution of 62.5vol% Propylamine and etched for 80 seconds.

The surface profiles of three microchannels before and after the etching process are shown in Figure 7.18.

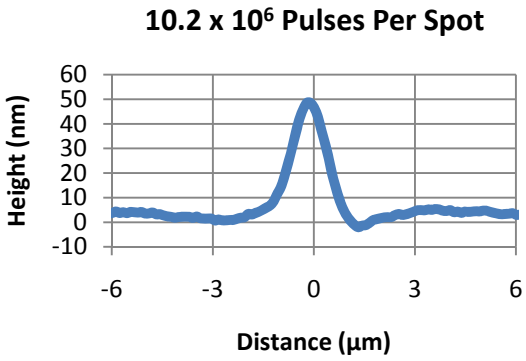

(a)

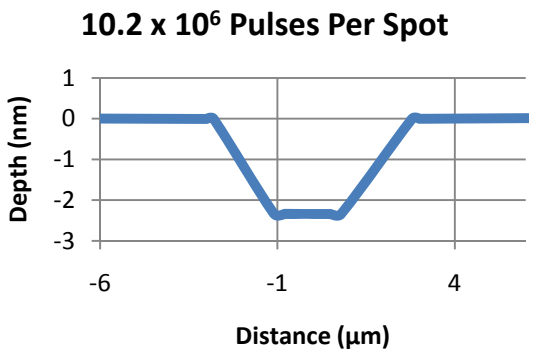

(b)

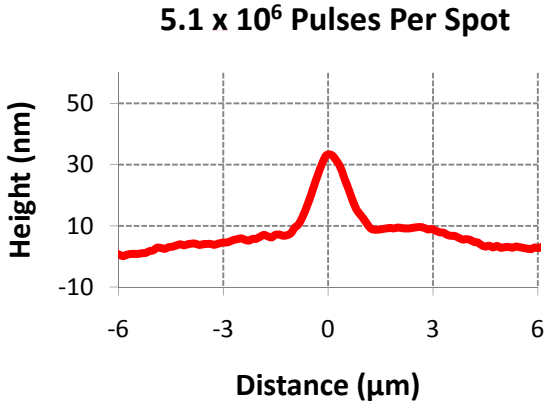

(c)

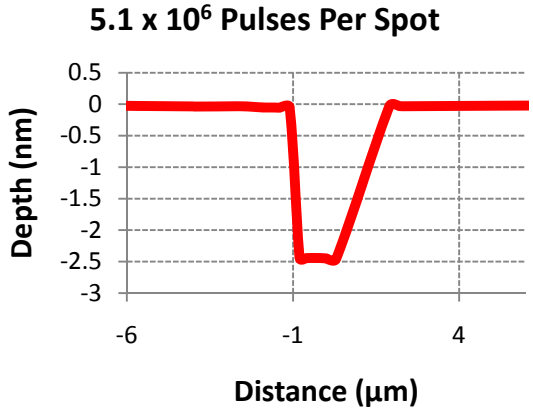

(d)

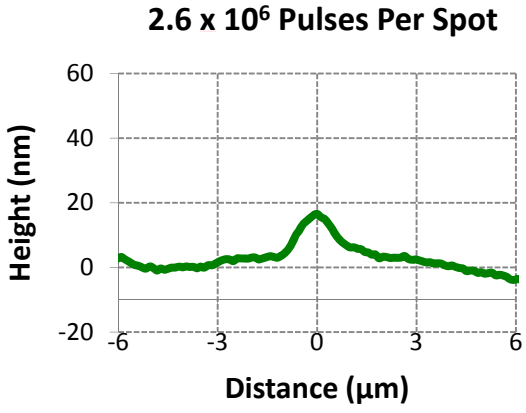

(e)

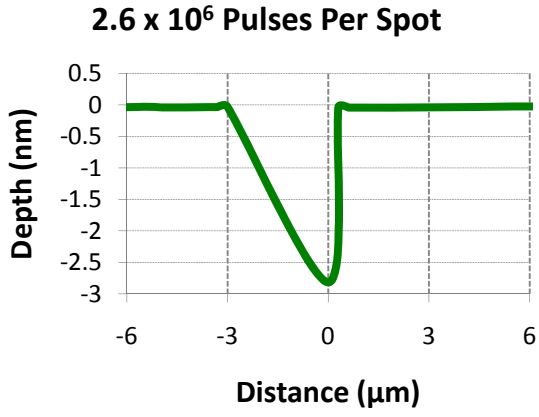

(f)

Figure 7.18: Surface profile of microchannels before (a,c,e) and after (b,d,f) etching. The number of pulses per spot was 10.2x106 (a,b), 5.1x106 (c,d), and 2.6x106 (e,f). The pulse energy for all cases was 0.17nJ.

Irradiation with 26MHz pulses provides a surface photo-expansion of 20-50nm with the highest expansion associated with the highest number of pulses per spot on the sample. The magnitude of this photo-expansion is about 5 times higher than the photo-expansion induced in the film sample under the same irradiation conditions as discussed earlier. This effect is due to both an increased amount of material within the focal region available to absorb energy in the bulk relative to the film as well as different initial bond structure configurations. The concentrated propylamine solution acts as a positive developer in this bulk glass and selectively etched the irradiated area. Table 7.2 lists several attributes of the surface profiles of the channels.

Table 7.2: Surface channel depth and aspect ratio as a function of the number of pulses per focal spot

Number of Pulses per Spot Incident on Sample ($x10^6$)	**Initial Photo-expansion (nm)**	**Final Etch Depth (nm)**	**Channel Aspect Ratio (Depth vs. Width)**
10.2	48.5	2340	0.48:1
5.1	24	2450	1.30:1
2.6	14.9	2810	0.94:1

Although a clear selective etching process is seen through the formation of the channels, we do not have a clear understanding of the mechanism of channel formation under these conditions. The final channel depth was found to increase with a decreasing number of pulses per focal spot. This is contrary to other findings with kHz repetition rate pulses where increasing dose led to an increased etch depth. Furthermore, the aspect ratio shows no dependence on the number of pulses per focal spot. It should be noted that due to the small channel width, there was a considerable amount of noise in the surface profile plots in some regions. The measurements listed here are exemplary values taken from regions of good signal to noise ratio but may not

reflect the entire microchannel. However, the observation of the channels and the etch depth provide clear evidence of positive selective etching using propylamine in this bulk material. It is interesting to note again that a weak amine solution of diisopentylamine was used as a negative developer for As_2S_3 films and had no observable effect on the bulk glass. The marked differences in etching behavior for these different amine-based solvents is not fully understood and warrants further investigation.

A separate set of experiments on the fabrication of surface reservoirs was made. The purpose of this experiment was to directly compare the photo-response and the selective etching of features fabricated using MHz pulses compared to kHz pulses. The laser used for irradiation was the same variable repetition rate fiber laser with a wavelength of 1043nm used for the kHz repetition rate experiments and was here set to 1.5MHz. The femtosecond laser focusing element was a 0.3NA (10X) microscope objective.

The reservoirs were fabricated using the same procedure as was used with 100kHz pulses. Squares with a side length of 200μm were scanned on the surface by creating a series of parallel lines separated by 2μm. The calculated size of the focal spot using the 0.3NA objective is 4.2μm, resulting in a ~50% overlap between parallel irradiated lines. The speed of the translation stage was 500μm/s, which corresponds to 1.27×10^4 pulses per focal spot. Multiple squares were fabricated with pulse energies ranging from 5.3-7.5 nJ, with 8nJ being the ablation threshold for the glass under these conditions.

As a result of the laser irradiation, the surface of the films exhibited a photo-expansion of up to 120nm for a pulse energy of 7.5nJ. The features were then immersed in a 0.1M solution of KOH for 45 minutes and the etch depth as a function of time is shown in Figure 7.19.

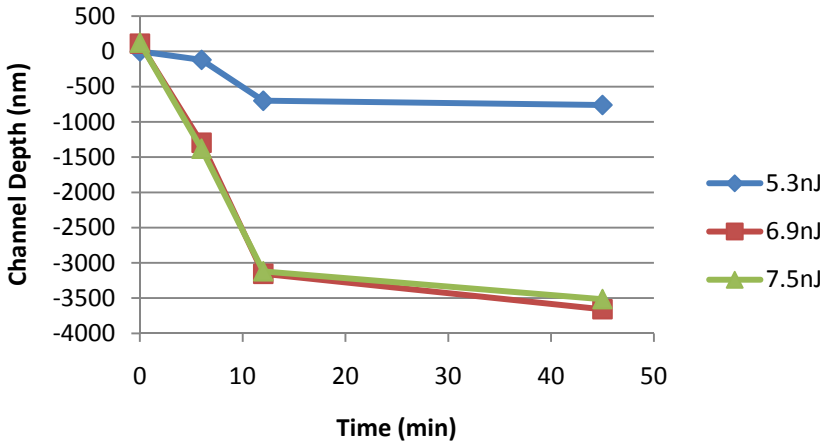

Figure 7.19: Etch depth of surface reservoirs fabricated with MHz repetition rate pulses as a function of etch time

As with the reservoirs fabricated with kHz pulses, the KOH solution acted as a positive developer and selectively etched the irradiated regions. The channel depth saturates at around 12-13 minutes as the photo-modified region is completely etched away. After this time, the entire sample is etched the same rate and the channel depth does not change.

The selective etch rate of the reservoirs are listed in Table 7.3.

Table 7.3: Selective etch rate of surface reservoirs fabricated with MHz pulses as a function of pulse energy

Pulse Energy (nJ)	**Selective Etch rate (nm/min)**
5.3	58
6.9	272
7.5	270

The two reservoirs fabricated with 6.9 and 7.5 nJ pulses exhibited basically the same response and had a notably higher etch rate than seen for the reservoir fabricated at 5.3nJ. Comparing the optimum cases for both kHz and MHz repetition rates where the pulse energy is near the ablation threshold, the photo-induced modification of the selective etch rate is over 11 times higher for MHz irradiation than seen for kHz irradiation (compare Table 7.3 to Table 7.1). This significant improvement is believed to be due to the increased magnitude of the photo-modification based on heat accumulation within the focal volume of the laser. Furthermore, the relative photo-expansion of the glass associated with laser irradiation appears to be a strong indicator of the degree to which selective etching will take place.

A side effect of the enhanced selectivity to etching is that the overall etch time is correspondingly reduced. Because the surface roughness generally increases with etch time, the reservoirs fabricated with MHz repetition rate pulses exhibited a decreased surface roughness relative to reservoirs fabricated with kHz pulses. The surface roughness of these reservoirs was ~35nm, compared to a ~10nm roughness for the un-irradiated sample before etching and ~400nm roughness for channels fabricated with kHz pulses and etched for 30min. A contour map and a surface profile of the fabricated reservoirs are shown in Figure 7.20.

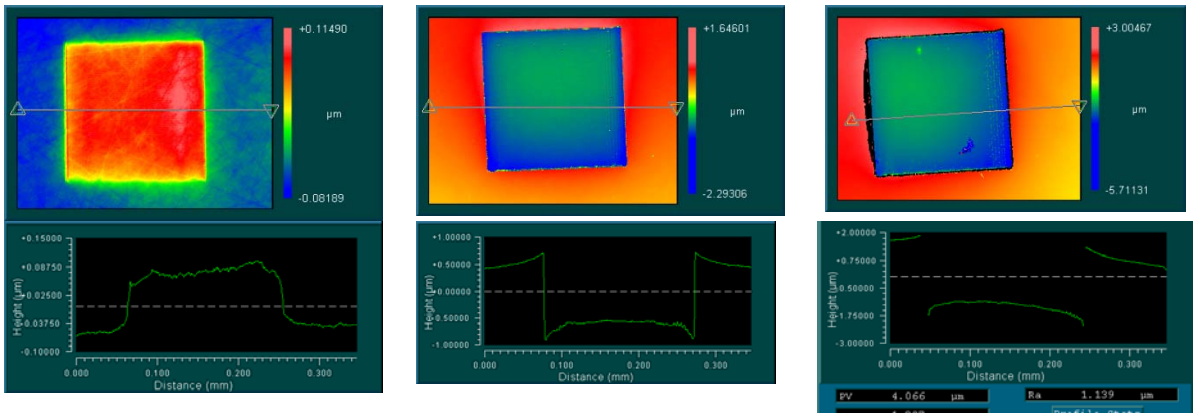

(a) (b) (c)

Figure 7.20: Contour map (above) and cross sectional surface profile (below) of 200 µm square features on the surface bulk As42S58 after etching for 0min (a), 6min (b), and 12min (c)

A second side effect and advantage of using MHz repetition rate pulses over kHz pulses is that the large number of pulses incident per focal spot is large enough that the additional dose on two sides of the reservoir associated with the translation stage decelerating and turning around does not significantly affect the profile of the reservoir. This eliminates the need to use a fast mechanical shutter to remove the large dips in the profile of the kHz reservoirs (see Figure 7.15). As a note, surface profiles in Figure 7.20 indicate that the center of the reservoir is larger than the regions close to the sidewall on all four sides. The mechanism responsible for this is not yet understood, but may be associated with the original shape of the photo-expanded material. This experiment was a significant advance in the selective etching of laser modified bulk chalcogenide glass.

Ablative processing accompanied by selective etching was also demonstrated in the MHz repetition rate regime. A series of connected microchannels 20µm wide by 2µm deep were fabricated using 10.7nJ pulses (33% above the ablation threshold) and selective etching for 6 minutes. A contour map and surface profile are shown in Figure 7.21.

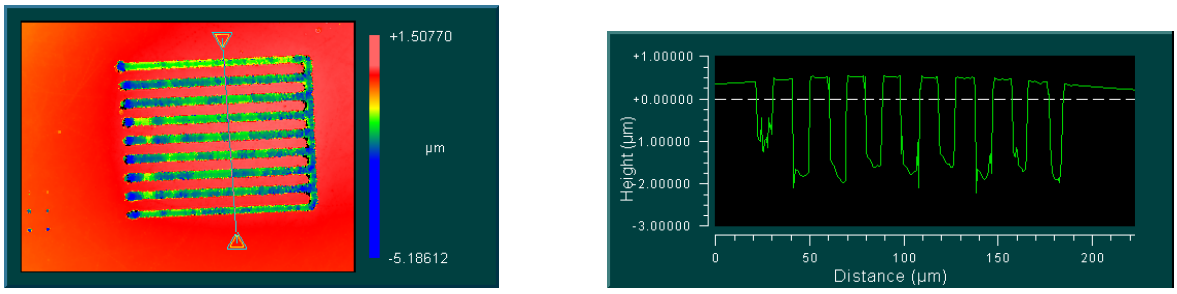

(a) (b)

Figure 7.21: Contour map (a) and surface profile (b) of connected series of 20µm x 2µm surface channels fabricated through ablative processing followed by immersion in 0.1M KOH for 6 minutes.

Due to the explosive nature of the processes, the floors of these channels have a significantly higher roughness (>500nm) than the channels fabricated through the selective etching of photo-modified regions. However, the problems associated with debris removal and photo-expansion of sidewalls associated with the fabrication of wide trenches through direct ablation are resolved in this approach due to the presence of the solvent (see Figure 7.7 - Figure 7.13).

7.3.2.2 Buried Microchannels

The fabrication of buried waveguides in the bulk glass using the same 1.5MHz repetition rate laser has also been investigated. For this test, large 25µm x 25µmx2mm volumes of photo-modified material were fabricated by scanning arrays of closely packed (2µm separation) photo-modified lines using the longitudinal writing geometry. This is similar to the channels produced with KHz pulses, but the area of the modified zone has been increased to appropriate dimensions for a practical channel. The increased area was intended to facilitate debris removal and flow of fresh solvent to the channel during etching. The pulse energies used ranged from 5.3-26.7nJ.

After irradiation, the sample was ground and polished to remove the surface ablation resulting from pulse energies higher than the 8nJ ablation threshold. Then the sample was placed in a

solution of 0.05M KOH for 80 minutes and then a solution of 0.1M KOH for an additional 50 minutes. The channel depth as a function of etch time for channels with pulse energies from 5.3-10.7nJ are shown in Figure 7.22. For higher pulse energies (>33% of the ablation threshold), the channel formation was nonuniform. It is thought that the presence of large ablation at the surface hindered the proper formation of the channel within the volume of the glass.

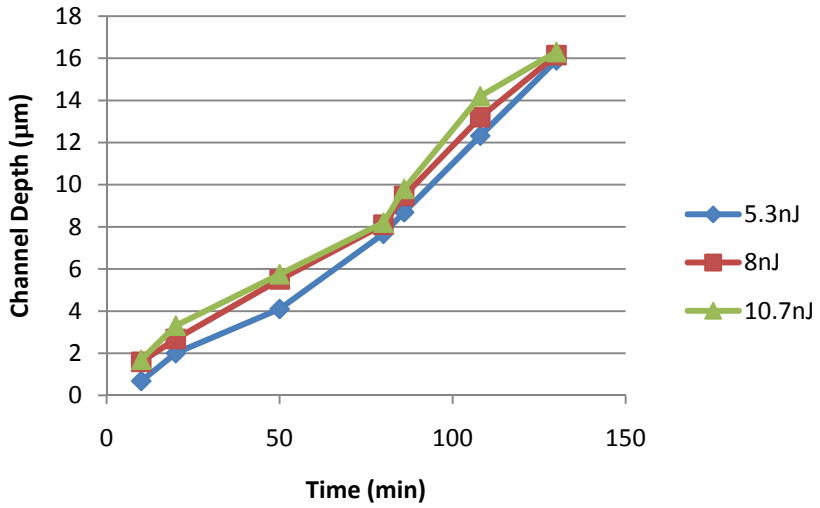

Figure 7.22: Channel depth as a function of etch time for buried microchannels fabricated using MHz repetition rate pulses as a function of etch time

For these three pulse energies spanning from 33% below the ablation threshold to 33% above it, the etch profile was essentially the same. Only a slight dependence (on the order of hundreds of nanometers) on the depth as a function of pulse energy was seen. The selective etch rate for the first 80 minutes when the sample was in the 0.05M KOH solution was ~100nm/min. This is slightly lower than the expected 135nm/min (half of the etch rate for 0.1M solution at the surface from Table 7.3). The etch rate for the remaining 50 minutes in the 0.1M solution was

~150nm/min, which is much lower than the expected 270nm/min seen previously. This may be due to an inability for fresh solvent to reach the channels as etching progresses.

7.4. Fabrication of Integrated Optical and Fluidic Elements

Utilizing the same approach as the described in section 7.3.2, evanescent-field sensors with a surface relief micro-structure for fluid containment and a buried optical waveguide situated below the fluid reservoir were fabricated (see Figure 7.1) with 1.5MHz pulses at a wavelength of 1043nm (μJewel, IMRA). A 0.65NA (40X) microscope objective was used to focus the femtosecond beam onto the surface of the sample. A series of devices with varying separation distances between the fluid reservoir and the optical waveguide as well as pulse energies used to fabricate the waveguide were fabricated to investigate the coupling of the waveguide and channel.

For each device, the optical waveguide was fabricated first by irradiating a single-pass line over the length of the 9mm long substrate. The pulse energy was varied from 0.9-3.5nJ, creating a series of waveguides with increasing refractive index and thus increasing confinement of light within the waveguide. The waveguide depth was varied from 2μm below the laser surface to 18μm below the laser surface as measured by the movement of the translation stage. An optical microscope image of the series of waveguides fabricated with a pulse energy of 2.6nJ is shown in Figure 7.23 with increasing depth from left to right in the image.

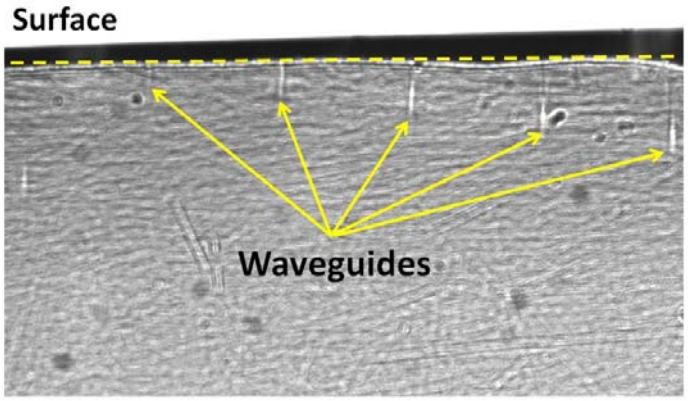

Figure 7.23: Optical microscope image of buried waveguides in bulk As_2S_3 fabricated with 2.6nJ pulses at a repetition rate of 1.5MHz. The six waveguides in the image are located between 2 and 18μ below the surface in 3μm increments (left to right).

The physical size of the waveguides is measured to be 2μm in width and 9μm in depth. This is indeed very similar to the size of the focal volume, which is calculated to be 2μm in width and 10μm in depth.

In a secondary step, the fluidic reservoirs were fabricated directly above the waveguides. The fabrication parameters for all of the reservoirs were the same. A single photo-modified line of glass was fabricated by two laser passes with 3.7nJ pulses (corresponding to 90% of the ablation threshold). The laser modified region was modified two times over to ensure a uniform modification as well as to achieve a high degree of material modification. After irradiation, the sample was placed in a 0.1M solution of KOH for 10 minutes. The resulting fluidic structures had a 1.8μm depth and a 3.5μm width. A contour map of the channels (a) and a cross-sectional surface profile (b) are given in Figure 7.24

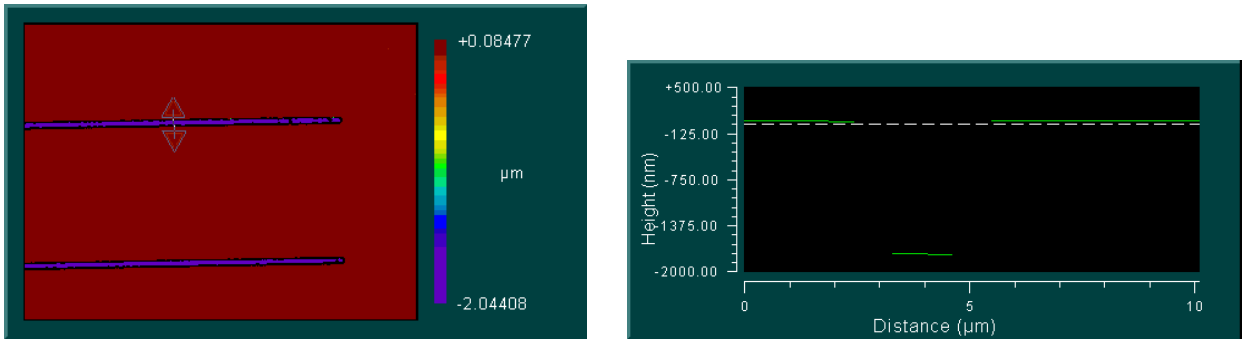

(a) (b)

Figure 7.24: Contour map (a) and cross-sectional surface profile (b) of surface relief micro-fluidic reservoirs fabricated in As_2S_3.

These surface profile measurements were taken with a Zygo NewView 6300 3D Optical Profiler and demonstrate the high quality of fabrication. The surface roughness of the channels was measured to be 17nm. During the etching process, the unmodified material was etched by 2µm, which revealed the first layer of waveguides. Thus, the smallest separation between a waveguide and fluidic reservoir was 1.2µm.

After fabrication, the optical waveguides were tested and confirmed to propagate both visible (632.8nm) and IR (1.5µm) light. An optical image of the output facet of the device fabricated with 0.8nJ pulses and a 4.2µm separation distance is shown in Figure 7.25. The bright white spot on the image is 632.8nm light exiting the output facet of the waveguide.

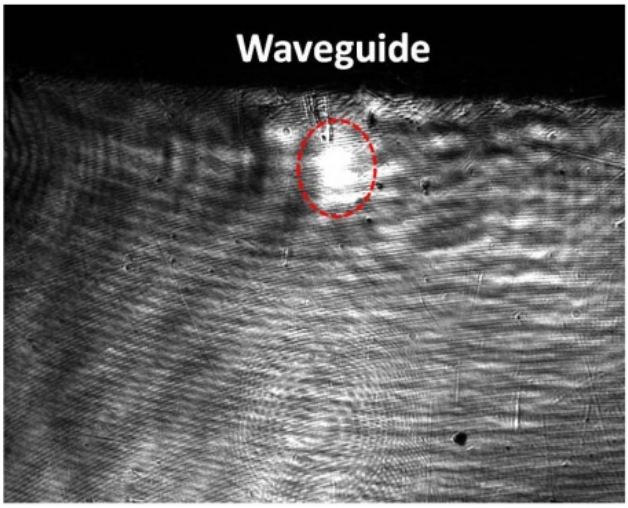

Figure 7.25: Optical microscope image of 632.8nm light propagating through an evanescent-field optofluidic sensor fabricated in As_2S_3

Figure 7.26 shows the calculated intensity distribution of the waveguide based on the measured size. The vertical lines represent the boundaries between core and cladding in the waveguide.

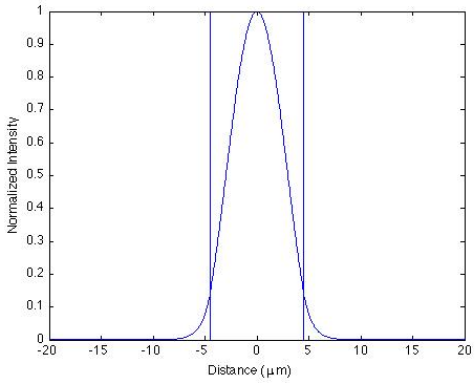

Figure 7.26: Cross-sectional plot of the intensity distribution of 1.5μm light through a 9μm waveguide in As_2S_3. The core and cladding are separated by vertical lines in the plot.

It is clear that most of the optical power of the propagating light is confined to the core of the waveguide. A calculation using equation (45) shows that the relative power of the evanescent

wave within the cladding of the waveguide is 4%. Therefore, although the waveguide and micro-fluidic reservoir have been fabricated within close proximity (<2μm) and the surface quality of the reservoir is high (<20nm roughness), the high confinement within the waveguide hinders the effective coupling of the two elements in this device. Indeed, the the devices were then tested as an optical sensor by propagating 1.5μm light through the optical waveguide and placing an absorbing solution of N-methylaniline, which has an absorption peak at 1.5μm in the fluidic reservoirs. However, the presence of the absorbing solution in the micro-channels did not affect the transmitted power through the waveguides as predicted by equation 134. Thus, no observable coupling between the waveguide and the micro-channel was observed for this fabricated device.

Although coupling has not been demonstrated using current fabrication techniques described in this dissertation in chalcogenide glasses, an unprecedented degree of machining precision of both optical and fluidic structures has been demonstrated. Furthermore, the realization of an optofluidic evanescent-wave sensor in As_2S_3 is feasible pending some additional improvements in fabrication technology. For example, the lateral dimension of the waveguides fabricated here is 2μm. The placement of a microfluidic element adjacent to the waveguide rather than above it would increase the power available in the evanescent field from 4% to 53%, which would enhance the coupling between the two elements. A further reduction of the waveguide size to 1μm using a higher numerical aperture focusing element would result in 82% of the optical power carried in the evanescent field available to interact with surrounding channels. This geometry is currently unrealizable as micro-channels are limited to a depth of several microns and surface defects inhibit the fabrication of waveguides this close to the surface. Thus, an

increased etch contrast ratio that enables deeper micro-channels or even buried micro-channels would enable the fabrication of this sensor.

CHAPTER 8: CONCLUSIONS AND PERSPECTIVES

This dissertation has described efforts towards the advancement of the femtosecond laser processing technique towards the fabrication of both optical and fluidic structures in Chalcogenide glasses. The work consisted of two parts. In the first part, emphasis was placed on the characterization and measurement of photo-induced modifications in Chalcogenide glasses under a variety of conditions. The investigation of the femtosecond laser photo-response of this family of glasses establishes this material family as a candidate for the fabrication of photonic elements in highly nonlinear materials through femtosecond laser direct writing. Since this fabrication technique relies on the response of the substrate material and the relative difference of optical or chemical properties between irradiated and untouched regions, a clear understanding of the photo-response of the substrate material is critical for the fabrication of optimized elements. In this dissertation, the photo-response of several glass families has been studied as a function of material composition and laser irradiation parameters. It was found that not only the composition of the glass, but also the state of the glass including the fabrication technique, physical geometry (bulk or film) and the thermal history of the glass all play critical roles in determining the extent to which a given Chalcogenide glass composition can be practically used as a substrate material for femtosecond laser processing. In addition, the role of laser parameters including laser repetition rate and laser dose on the magnitude of induced material modifications was discussed. For Chalcogenide glasses in particular, the photo-response is highly dependent on thermal processes and high temperatures caused by heat accumulation in the focal region using high repetition rate pulses provided the maximum photo-response. Furthermore, the magnitude of the photo-response could be controlled using the laser

dose by means of either the laser irradiance or the number of pulses per focal spot incident on the sample, which is effectively controlled by the translation speed of the material through the focal volume of the writing laser. A model of avalanche and multiphoton ionization was used to correlate the photo-induced modifications with the electron density generated during irradiation as well as described the contributions of linear and nonlinear absorption.

The second section of the dissertation deals with the fabrication of micro-fluidic elements in Chalcogenide glasses using femtosecond laser processing. Several techniques are discussed including direct ablation of surface features and the use of wet chemical etching to preferentially etch out photo-modified regions. Again, the role of laser parameters during fabrication such as laser repetition rate and laser dose was investigated. In a manner similar to the fabrication of optical features, the formation of micro-fluidic elements was enhanced by laser processing at MHz repetition rates. Finally, the use of femtosecond laser processing for the fabrication of both optical and fluidic elements together in a single substrate with a separation on the order of microns was demonstrated.

Considering the progress made during the work described in this dissertation, there exist several avenues for future work that remain unresolved. The physical mechanisms associated with femtosecond laser interaction with transparent media are still not yet fully understood. At this time, it is difficult to predict or model *a priori* the photo-response of an unstudied material to femtosecond laser exposure. As described in this dissertation, even within the Chalcogenide glass family, there exists significant differences in the nature of the photo-response of different materials. Furthermore, as described in section 6.2, the photo-induced density and refractive

index modifications are not always linked and continued investigations into the photo-response of transparent media are necessary. Additionally, there is need to investigate the preferential etching of photo-modified chalcogenide glasses using positive developers. To date, the fabrication of micro-fluidic elements is limited to surface relief features due to a limited contrast ratio between the etch rates of photo-modified and unexposed regions of the glass when a positive developer is used. Alternatively, the use of negative etching has been successfully used for the fabrication of photonic circuits in thin films of arsenic trisulfide [200, 201]. In this case, special care was taken during the glass elaboration to increase the number of As_4S_6 cage molecules. The function of the laser modification was then to polymerize the cage molecules to a state similar to the original bulk glass, which has a significantly higher etch resistance to the etching solvent. This method provided a significant improvement over previous photonic crystal fabrication processes involving layer-by-layer lithography [190]. While this technique provided a high dissolution contrast ratio and high quality photonic crystals, the negative development used is undesirable for the fabrication of microchannels within the volume of a bulk glass. Future studies towards this end will necessarily focus on the selection and evaluation of an appropriate solvent with a high positive dissolution contrast ratio for the stoichiometry of the bulk glass.

LIST OF REFERENCES

[1]. S. Haeberle and R. Zengerle, "Microfluidic platforms for lab-on-a-chip applications," *Lab Chip,* vol. 7, pp. 1094-1110, 2007.[2]. D. R. Reyes, D. Iossifidis, P. Auroux, and A. Manz, "Micro Total Analysis Systems. 1. Introduction, Theory, and Technology," *Anal Chem,* vol. 74, pp. 2653-2636, 2002.

[3]. P. Auroux, D. Iossifidis, D. R. Reyes, and A. Manz, "Micro Total Analysis Systems. 2. Analytical Standard Operations and Applications," *Anal Chem,* vol. 74, pp. 2637-2652, 2002.

[4]. H. Andersson, "Microfluidic devices for cellomics: a review," *Sensors and Actuators B: Chemical,* vol. 92, pp. 315-325, Jul 15 2003.

[5]. D. Psaltis, S. R. Quake, and C. Yang, "Developing optofluidic technology through the fusion of microfluidics and optics," *Nature,* vol. 442, p. 381, Jul 17 2006.

[6]. A. J. Demello and A. J. Demello, "Control and detection of chemical reactions in microfluidic systems," *Nature,* vol. 442, p. 394, Jul 26 2006.

[7]. G. Whitesides and G. Whitesides, "The origins and the future of microfluidics," *Nature,* vol. 442, p. 368, Jul 26 2006.

[8]. P. Yager, P. Yager, T. Edwards, T. Edwards, E. Fu, E. Fu, K. Helton, K. Helton, K. Nelson, K. Nelson, M. R. Tam, M. R. Tam, B. H. Weigl, and B. H. Weigl, "Microfluidic diagnostic technologies for global public health," *Nature,* vol. 442, p. 412, Jul 26 2006.

[9]. R. W. Applegate, D. N. Schafer, W. Amir, J. Squier, T. Vestad, J. Oakey, and D. W. M. Marr, "Optically integrated microfluidic systems for cellular characterization and manipulation," in *J Opt A-Pure Appl Op*. vol. 9, 2007, pp. S122-S128.

[10]. R. Applegate Jr., J. Squier, T. Vestad, J. Oakey, D. Marr, P. Bado, M. Dugan, and A. Said, "Microfluidic sorting system based on optical waveguide integration and diode laser bar trapping," *Lab Chip,* vol. 6, p. 422, Jan 1 2006.

[11]. Y. Hanada, K. Sugioka, H. Kawano, I. Ishikawa, A. Miyawaki, and K. Midorikawa, "Nano-aquarium for dynamic observation of living cells fabricated by femtosecond laser direct writing of photostructurable glass," *Biomed Microdevices,* vol. 10, pp. 403-410, Jun 12 2008.

[12]. R. Osellame, R. Martinez, P. Laporta, R. Ramponi, and G. Cerullo, "Integration of micro-optics and microfluidics in a glass chip by fs-laser for optofluidic applications," pp. 720202-720202-12, Jan 1 2009.

[13]. R. M. Vazquez, R. Osellame, D. Nolli, C. Dongre, H. Van Den Vlekkert, R. Ramponi, M. Pollnau, and G. Cerullo, "Integration of femtosecond laser written optical waveguides in a lab-on-chip," *Lab Chip,* vol. 9, p. 91, Jan 1 2009.

[14]. S. Sia and G. Whitesides, "Microfluidic devices fabricated in Poly(dimethylsiloxane) for biological studies," *Electrophoresis,* vol. 24, pp. 3563-3576, Nov 1 2003.

[15]. J. Suter, I. White, H. Zhu, H. Shi, C. Caldwell, and X. Fan, "Label-free quantitative DNA detection using the liquid core optical ring resonator," *Biosensors and Bioelectronics,* vol. 23, pp. 1003-1009, Feb 28 2008.

[16]. D. Huh, W. Gu, Y. Kamotani, J. Grotberg, and S. Takayama, "Microfluidics for flow cytometric analysis of cells and particles," *Physiol. Meas.,* vol. 26, pp. R73-R98, Feb 2 2005.
[17]. S. Quake, "From Micro- to Nanofabrication with Soft Materials," *Science,* vol. 290, pp. 1536-1540, Nov 24 2000.
[18]. A. Y. Fu, H. P. Chou, C. Spence, F. H. Arnold, and S. R. Quake, "An Integrated Microfabricated Cell Sorter," *ANALYTICAL CHEMISTRY-WASHINGTON DC-,* Jan 1 2002.
[19]. S. Bleil, D. Marr, and C. Bechinger, "Field-mediated self-assembly and actuation of highly parallel microfluidic devices," *Appl. Phys. Lett.,* vol. 88, p. 263515, Jan 1 2006.
[20]. J. Emmelkamp, F. Wolbers, H. Andersson, R. Dacosta, B. Wilson, I. Vermes, and A. Van Den Berg, "The potential of autofluorescence for the detection of single living cells for label-free cell sorting in microfluidic systems," *Electrophoresis,* vol. 25, pp. 3740-3745, Nov 1 2004.
[21]. J. Krüger, K. Singh, A. O'Neill, C. Jackson, A. Morrison, and P. O'Brien, "Development of a microfluidic device for fluorescence activated cell sorting," *J Micromech Microeng,* vol. 12, pp. 486-494, 2002.
[22]. J. Hu, V. Tarasov, A. Agarwal, L. Kimerling, N. Carlie, L. Petit, and K. C. Richardson, "Fabrication and testing of planar chalcogenide waveguide integrated microfluidic sensor," in *Opt Express*. vol. 15, 2007, pp. 2307-2314.
[23]. J. Hu, N. Carlie, L. Petit, A. Agarwal, K. C. Richardson, and L. Kimerling, "Demonstration of chalcogenide glass racetrack microresonators," *Optics Letters,* vol. 33, p. 761, Apr 15 2008.
[24]. T. N. Kim, K. Campbell, A. Groisman, D. Kleinfeld, and C. B. Schaffer, "Femtosecond laser-drilled capillary integrated into a microfluidic device," in *Appl Phys Lett*. vol. 86, 2005, pp. -.
[25]. A. Terray, J. Arnold, and S. J. Hart, "Enhanced optical chromatography in a PDMS microfluidic system," *Optics Express,* vol. 13, pp. 10406-10415, 2005.
[26]. Y. Tung, M. Zhang, C. T. Lin, and K. Kurabayashi, "PDMS-based opto-fluidic micro flow cytometer with two-color, multi-angle fluorescence detection …," *Sensors & Actuators: B. Chemical,* Jan 1 2004.
[27]. Z. Li, Z. Zhang, A. Scherer, and D. Psaltis, "Mechanically tunable optifluidic distributed feedback dye laser," *Opt. Exp.,* vol. 14, p. 10494, Oct 19 2006.
[28]. A. Zoubir, C. Lopez, M. C. Richardson, and K. C. Richardson, "Femtosecond laser fabrication of tubular waveguides in poly(methyl methacrylate)," in *Opt Lett*. vol. 29, 2004, pp. 1840-1842.
[29]. A. Szameit, F. Dreisow, T. Pertsch, S. Nolte, and A. Tuennermann, "Control of directional evanescent coupling in fs laser written waveguides," in *Optics Express*. vol. 15, 2007, pp. 1579-1587.
[30]. S. Nolte, G. Kamlage, F. Korte, T. Bauer, T. Wagner, A. Ostendorf, C. Fallnich, and H. Welling, "Microstructuring with femtosecond lasers," in *Adv Eng Mater*. vol. 2, 2000, pp. 23-27.

[31]. M. Watanabe, H. Sun, S. Juodkazis, T. Takahashi, S. Matsuo, Y. Suzuki, J. Nishii, and H. Misawa, "Three-Dimensional Optical Data Storage in Vitreous Silica," *Jpn. J. Appl. Phys.,* vol. 37, pp. L1527-L1530, Dec 15 1998.
[32]. M. Yamaji, H. Kawashima, J. Suzuki, and S. Tanaka, "Three dimensional micromachining inside a transparent material by single pulse femtosecond laser through a hologram," *Appl. Phys. Lett.,* vol. 93, p. 041116, Jan 1 2008.
[33]. A. Zoubir, C. Rivero, R. Grodsky, K. C. Richardson, M. C. Richardson, T. Cardinal, and M. Couzi, "Laser-induced defects in fused silica by femtosecond IR irradiation," *Phys. Rev. B,* vol. 73, p. 224117, Jan 1 2006.
[34]. A. Zoubir, M. C. Richardson, L. Canioni, A. Brocas, and L. Sarger, "Optical properties of infrared femtosecond laser-modified fused silica and application to waveguide fabrication," in *J Opt Soc Am B*. vol. 22, 2005, pp. 2138-2143.
[35]. K. M. Davis, K. Miura, N. Sugimoto, and K. Hirao, "Writing waveguides in glass with a femtosecond laser," in *Opt Lett*. vol. 21, 1996, pp. 1729-1731.
[36]. K. Miura, J. R. Qiu, H. Inouye, T. Mitsuyu, and K. Hirao, "Photowritten optical waveguides in various glasses with ultrashort pulse laser," in *Appl Phys Lett*. vol. 71, 1997, pp. 3329-3331.
[37]. P. G. Kazansky, W. Yang, E. Bricchi, J. Bovatsek, A. Arai, Y. Shimotsuma, K. Miura, and K. Hirao, ""Quill" writing with ultrashort light pulses in transparent materials," *Appl. Phys. Lett.,* vol. 90, p. 151120, Jul 13 2007.
[38]. M. Will, S. Nolte, B. N. Chichkov, and A. Tünnermann, "Optical properties of waveguides fabricated in fused silica by femtosecond laser pulses," *Appl. Opt,* Jan 1 2002.
[39]. A. M. Streltsov and N. F. Borrelli, "Study of femtosecond-laser-written waveguides in glasses," in *J Opt Soc Am B*. vol. 19, 2002, pp. 2496-2504.
[40]. M. Bellec, E. Riley, L. Canioni, B. Bousquet, F. Rocco, T. Cardinal, J. J. Videau, and M. Treguer, "Femtosecond irradiation of a zinc phosphate glass containing silver," Jan 17 2007.
[41]. J. W. Chan, T. R. Huser, S. H. Risbud, J. S. Hayden, and D. M. Krol, "Waveguide fabrication in phosphate glasses using femtosecond laser pulses," *Applied Physics Letters,* vol. 82, pp. 2371-2373, Jan 1 2003.
[42]. J. W. Chan, T. R. Huser, J. S. Hayden, S. H. Risbud, and D. M. Krol, "Fluorescence Spectroscopy of Color Centers Generated in Phosphate Glasses after Exposure to …," *Journal of the American Ceramic Society,* Jan 1 2002.
[43]. T. T. Fernandez, G. Della Valle, R. Osellame, G. Jose, N. Chiodo, A. Jha, and P. Laporta, "Active waveguides written by femtosecond laser irradiation in an erbium-doped phospho-tellurite glass," *Optics Express,* vol. 16, p. 15198, Jan 1 2008.
[44]. Y. Tokuda, M. Saito, M. Takahashi, K. Yamada, W. Watanabe, K. Itoh, and T. Yoko, "Waveguide formation in niobium tellurite glasses by pico-and femtosecond laser pulses," *Journal of Non-Crystalline Solids,* vol. 326&327, pp. 472-475, Jan 1 2003.
[45]. M. Shinoda, R. Gattass, and E. Mazur, "Femtosecond laser-induced formation of nanometer-width grooves on synthetic single-crystal diamond surfaces," *J. Appl. Phys.,* vol. 105, p. 053102, Jan 1 2009.

[46]. Y. Liao, J. Xu, Y. Cheng, Z. Zhou, F. He, H. Sun, J. Song, X. Wang, Z. Xu, K. Sugioka, and K. Midorikawa, "Electro-optic integration of embedded electrodes and waveguides in LiNbO_3 using a femtosecond laser," *Optics Letters,* vol. 33, p. 2281, Oct 1 2008.
[47]. R. R. Thomson, S. Campbell, I. J. Blewett, A. K. Kar, and D. T. Reid, "Optical waveguide fabrication in z-cut lithium niobate (LiNbO) using femtosecond pulses in the low …," *Applied Physics Letters,* vol. 88, p. 111109, Jan 1 2006.
[48]. A. H. Nejadmalayeri, P. R. Herman, J. Burghoff, M. Will, S. Nolte, and A. Tünnermann, "Inscription of optical waveguides in crystalline silicon by mid-infrared femtosecond laser pulses," *Optics Letters,* vol. 30, pp. 964-966, Jan 1 2005.
[49]. L. Gui, B. Xu, and T. C. Chong, "Microstructure in lithium niobate by use of focused femtosecond laser pulses," *Photonics Technology Letters,* vol. 16, pp. 1337-1339, Jan 1 2004.
[50]. T. Gorelik, M. Will, S. Nolte, A. Tuennermann, and e. al., "Transmission electron microscopy studies of femtosecond laser induced modifications in quartz," *Applied Physics A: Materials Science & Processing,* vol. 76, pp. 309-311, Jan 1 2003.
[51]. A. Zoubir, M. C. Richardson, C. Rivero, A. Schulte, C. Lopez, K. C. Richardson, N. Hô, and R. Vallée, "Direct femtosecond laser writing of waveguides in As2S3 thin films," *Optics Letters,* vol. 29, pp. 748-750, Jan 1 2004.
[52]. A. Zoubir, L. Shah, K. Richardson, and M. Richardson, "Practical uses of femtosecond laser micro-materials processing," *Applied Physics A: Materials Science & Processing,* vol. 77, pp. 311-315, 2003.
[53]. A. Zoubir, "Towards Direct Writing of 3-D Photonic Circuits Using Ultrafast Lasers," *Ph.D Thesis, College of Optics and Photonics at the University of Central Florida,* p. 185, Nov 12 2004.
[54]. O. M. Efimov, L. B. Glebov, K. C. Richardson, E. V. Styland, T. Cardinal, S. Park, M. Couzi, and J. Brunéel, "Waveguide writing in chalcogenide glasses by a train of femtosecond laser pulses," *Opt. Mat.,* vol. 17, pp. 379-386, Jan 1 2001.
[55]. S. Juodkazis, T. Kondo, H. Misawa, A. Rode, M. Samoc, and B. Luther-Davies, "Photo-structuring of As2S3 glass by femtosecond irradiation," in *Opt Express*. vol. 14, 2006, pp. 7751-7756.
[56]. S. Juodkazis, H. Misawa, O. Louchev, and K. Kitamura, "Femtosecond laser ablation of chalcogenide glass: explosive formation of nano-fibres against thermo-capillary growth of micro-spheres," *Nanotechnology,* vol. 17, pp. 4802-4805, Sep 7 2006.
[57]. M. Hughes, W. Yang, and D. Hewak, "Fabrication and characterization of femtosecond laser written waveguides in chalcogenide glass," *Appl. Phys. Lett.,* vol. 90, p. 131113, Jan 1 2007.
[58]. L. Petit, N. Carlie, T. Anderson, J. Choi, M. Richardson, and K. Richardson, "Progress on the Photoresponse of Chalcogenide Glasses and Films to Near-Infrared Femtosecond Laser Irradiation: A Review," *Ieee J Sel Top Quant,* vol. 14, pp. 1323-1334, 2008.
[59]. T. Anderson, L. Petit, N. Carlie, J. Choi, J. Hu, A. Agarwal, L. Kimerling, K. C. Richardson, and M. C. Richardson, "Femtosecond laser photo-response of Ge_<23>Sb_<7>S_<70> films," *Optics Express,* vol. 16, pp. 20081-20098, 2008.
[60]. T. Cardinal, K. C. Richardson, H. Shim, A. Schulte, A. A. Schulte, R. Beatty, K. L. Foulgoc, C. Meghini, J. Viens, and A. Villeneuve, "Non-linear optical properties of

chalcogenide glasses in the system As-S-Se," *Journal of Non-Crystalline Solids,* vol. 256&257, pp. 353-360, Jan 1 1999.
[61]. L. Petit, N. Carlie, T. Anderson, M. Couzi, J. Choi, M. C. Richardson, and K. C. Richardson, "Effect of IR femtosecond laser irradiation on the structure of new sulfo-selenide glasses," *Opt. Mat.,* vol. 29, pp. 1075-1083, Feb 11 2007.
[62]. L. Petit, J. Choi, T. Anderson, R. Villeneuve, J. Massera, N. Carle, M. Couzi, M. C. Richardson, and K. C. Richardson, "Effect of Ga and Se addition on the ‘‘near-surface” photo-response of new Ge-based chalcogenide glasses under IR femtosecond laser exposure," *Opt. Mat.,* vol. 31, pp. 965-969, Mar 20 2009.
[63]. K. C. Richardson, T. Cardinal, M. C. Richardson, A. Schulte, and S. Seal, "Engineering Glassy Chalcogenide Materials for Integrated Optics Applications," *Photo-Induced Metastability in Amorphous Semiconductors,* p. 383, Jan 22 2003.
[64]. A. Zoubir, M. C. Richardson, C. Lopez, L. Petit, K. C. Richardson, C. Rivero, and A. Schulte, "Femtosecond direct writing of waveguides in non-oxide glasses," *Photon Processing in Microelectronics and Photonics III, Proc. of SPIE,* vol. 5339, p. 175, Jan 22 2004.
[65]. O. Efimov, L. Glebov, S. Grantham, and M. Richardson, "Photoionization of silicate glasses exposed to IR femtosecond pulses," *Journal of Non-Crystalline Solids,* vol. 253, pp. 58-67, Aug 3 1999.
[66]. A. Zoubir, C. Rivero, R. Grodsky, K. Richardson, M. Richardson, T. Cardinal, and M. Couzi, "Laser-induced defects in fused silica by femtosecond IR irradiation," *Phys. Rev. B,* vol. 73, p. 224117, Jan 1 2006.
[67]. K. Tanaka, "Photoexpansion in As_{2}S_{3} glass," *Phys. Rev. B,* vol. 57, p. 5163, Feb 13 1998.
[68]. H. Hisakuni and K. Tanaka, "Giant photoexpansion in As[sub 2]S[sub 3] glass," *Applied Physics Letters,* vol. 65, pp. 2925-2927, 1994.
[69]. L. Calvez, Z. Yang, and P. Lucas, "Reversible giant photocontraction in chalcogenide glass," *Optics Express,* vol. 17, pp. 18581-18589, 2009.
[70]. H. Sun, F. He, Z. Zhou, Y. Cheng, Z. Xu, K. Sugioka, and K. Midorikawa, "Fabrication of microfluidic optical waveguides on glass chips with femtosecond laser pulses," in *Opt Lett*. vol. 32, 2007, pp. 1536-1538.
[71]. Y. Li, K. Itoh, W. Watanabe, K. Yamada, D. Kuroda, J. Nishii, and Y. Jiang, "Three-dimensional hole drilling of silica glass from the rear surface with femtosecond laser pulses," *Optics Letters,* vol. 26, pp. 1912-1914, Nov 15 2001.
[72]. R. An, Y. Li, Y. Dou, D. Liu, H. Yang, and Q. Gong, "Water-assisted drilling of microfluidic chambers inside silica glass with femtosecond laser pulses," in *Appl Phys A-Mater*. vol. 83, 2006, pp. 27-29.
[73]. A. Marcinkevicius, S. Juodkazis, M. Watanabe, M. Miwa, S. Matsuo, and H. Misawa, "Femtosecond laser-assisted three-dimensional microfabrication in silica," *Opt. Lett.,* vol. 26, p. 277, Feb 15 2001.
[74]. V. Maselli, R. Osellame, G. Cerullo, R. Ramponi, P. Laporta, L. Magagnin, and P. L. Cavallotti, "Fabrication of long microchannels with circular cross section using astigmatically shaped femtosecond laser pulses and chemical etching," in *Appl Phys Lett*. vol. 88, 2006, pp. -.

[75]. S. Matsuo, Y. Tabuchi, T. Okada, S. Juodkazis, and H. Misawa, "Femtosecond laser assisted etching of quartz: microstructuring from inside," *Applied Physics A: Materials Science & Processing,* vol. 84, pp. 99-102, 2006.
[76]. S. Juodkazis, Y. Nishi, and H. Misawa, "Femtosecond laser-assisted formation of channels in sapphire using KOH solution," *physica status solidi (RRL)-Rapid Research Letters,* vol. 2, 2008.
[77]. Y. Iga, T. Ishizuka, W. Watanabe, K. Itoh, Y. Li, and J. Nishii, "Characterization of Micro-Channels Fabricated by In-Water Ablation of Femtosecond Laser Pulses," *Jpn. J. Appl. Phys.,* vol. 43, pp. 4207-4211, Jul 7 2004.
[78]. K. Ke, E. F. Hasselbrink, and A. J. Hunt, "Rapidly prototyped three-dimensional nanofluidic channel networks in glass substrates," in *Anal Chem*. vol. 77, 2005, pp. 5083-5088.
[79]. J. Chan, T. Huser, S. Risbud, and D. M. Krol, "Modification of the fused silica glass network associated with waveguide fabrication using femtosecond laser pulses," *Applied Physics A: Materials Science & Processing,* vol. 76, pp. 367-372, Mar 1 2003.
[80]. J. W. Chan, T. Huser, S. Risbud, and D. M. Krol, "Structural changes in fused silica after exposure to focused femtosecond laser pulses," *Optics Letters, Vol. 26, Issue 21, pp. 1726-1728*.
[81]. R. Devine and J. Capponi, "Pressure-induced bond-angle variation in amorphous SiO 2," *Phys. Rev. B,* vol. 35, pp. 2560-2562, Feb 1 1987.
[82]. E. Bricchi, B. G. Klappauf, and P. G. Kazansky, "Form birefringence and negative index change created by femtosecond direct writing in transparent materials," *Opt. Lett.,* vol. 29, p. 119, Feb 15 2004.
[83]. L. Sudrie, M. Franco, B. Prade, and A. Mysyrowicz, "Study of damage in fused silica induced by ultra-short IR laser pulses," *Optics Communications,* vol. 191, pp. 333-339, Feb 12 2001.
[84]. V. Bhardwaj, E. Simova, P. Rajeev, C. Hnatovsky, R. Taylor, D. Rayner, and P. Corkum, "Optically Produced Arrays of Planar Nanostructures inside Fused Silica," *Physical Review Letters,* vol. 96, p. 057404, Jan 17 2006.
[85]. C. Hnatovsky, R. Taylor, P. Rajeev, E. Simova, V. Bhardwaj, D. Rayner, and P. Corkum, "Pulse duration dependence of femtosecond-laser-fabricated nanogratings in fused silica," *Appl. Phys. Lett.,* vol. 87, p. 014104, Jan 1 2005.
[86]. C. Hnatovsky, R. S. Taylor, R. Bhardwaj, E. Simova, D. M. Rayner, and P. B. Corkum, "Long-range periodic planar manostructures produced in glass by femtosecond laser dielectric modification," *CLEO Proceedings CThV1,* p. 1906, Aug 29 2005.
[87]. Y. Shimotsuma, P. G. Kazansky, J. Qiu, and K. Hirao, "Self-Organized Nanogratings in Glass Irradiated by Ultrashort Light Pulses," *Physical Review Letters,* vol. 91, p. 247405, 2003.
[88]. C. Hnatovsky, R. S. Taylor, E. Simova, V. R. Bhardwaj, D. M. Rayner, and P. B. Corkum, "Polarization-selective etching in femtosecond laser-assisted microfluidic channel fabrication in fused silica," in *Opt Lett*. vol. 30, 2005, pp. 1867-1869.
[89]. R. Osellame, V. Maselli, R. M. Vazquez, R. Ramponi, and G. Cerullo, "Integration of optical waveguides and microfluidic channels both fabricated by femtosecond laser irradiation," in *Appl Phys Lett*. vol. 90, 2007, p. 231118.

[90]. S. Matsuo, S. Kiyama, Y. Shichijo, T. Tomita, S. Hashimoto, Y. Hosokawa, and H. Masuhara, "Laser microfabrication and rotation of ship-in-a-bottle optical rotators," *Appl. Phys. Lett.,* vol. 93, p. 051107, Jan 1 2008.
[91]. H. Sun, F. He, Z. Zhou, Y. Cheng, Z. Xu, K. Sugioka, and K. Midorikawa, "Fabrication of microfluidic optical waveguides on glass chips with femtosecond laser pulses," *Opt. Lett.,* vol. 23, p. 1536, May 10 2007.
[92]. S. L. N. Ho, M. Eaton, S. M. Herman, and P. R. Aitchison, "Single and Multi-Scan Femtosecond Laser Writing for Selective Chemical Etching of Glass Micro- …," *Optical Society of America-CLEO/QELS Conference,* Jan 1 2007.
[93]. C. Hnatovsky, R. S. Taylor, E. Simova, and P. P. Rajeev, "Fabrication of microchannels in glass using focused femtosecond laser radiation and selective …," *Applied Physics A: Materials Science & Processing,* Jan 1 2006.
[94]. K. Vishnubhatla, J. Clark, G. Lanzani, R. Ramponi, R. Osellame, and T. Virgili, "Ultrafast optofluidic gain switch based on conjugated polymer in femtosecond laser fabricated microchannels," *Applied Physics Letters,* vol. 94, p. 041123, Jan 1 2009.
[95]. T. Chen, J. Si, X. Hou, S. Kanehira, K. Miura, and K. Hirao, "Photoinduced microchannels inside silicon by femtosecond pulses," *Appl. Phys. Lett.,* vol. 93, p. 051112, Jan 1 2008.
[96]. S. Juodkazis, K. Nishimura, H. Misawa, T. Ebisui, R. Waki, S. Matsuo, and T. Okada, "Control over the crystalline state of sapphire," *Adv. Mater.,* vol. 18, 2006.
[97]. S. Juodkazis and H. Misawa, "Laser processing of sapphire by strongly focused femtosecond pulses," *Appl. Phys. A,* Jul 3 2008.
[98]. S. Matsuo, Y. Shichijo, T. Tomita, and S. Hashimoto, "Laser fabrication of Ship-in-a-bottle Microstructures in Sapphire," *JLMN,* vol. 2, pp. 114-116, 2007.
[99]. S. Matsuo, K. Tokumi, T. Tomita, and S. Hashimoto, "Three-Dimensional Residue-Free Volume Removal inside Sapphire by High-Temperature Etching after Irradiation of Femtosecond Laser Pulses," *Laser Chem.,* vol. 2008, pp. 1-5, Jan 1 2008.
[100]. D. Wortmann, J. Gottmann, N. Brandt, and H. Horn-Solle, "Micro-and nanostructures inside sapphire by fs-laser irradiation and selective etching," *Optics Express,* vol. 16, pp. 1517-1522, 2008.
[101]. R. R. Gattass and E. Mazur, "Femtosecond laser micromachining in transparent materials," *Nature Photonics,* vol. 2, p. 219, Apr 1 2008.
[102]. S. K. Sundaram and E. Mazur, "Inducing and probing non-thermal transitions in semiconductors using femtosecond laser pulses," *Nature Materials,* vol. 1, p. 217, Dec 1 2002.
[103]. S. S. Mao, F. Quere, S. Guizard, X. Mao, R. E. Russo, G. Petite, and P. Martin, "Dynamics of femtosecond laser interactions with dielectrics," *Appl. Phys. A,* vol. 79, pp. 1695-1709, 2004.
[104]. F. Korte, S. Adams, A. Egbert, C. Fallnich, A. Ostendorf, S. Nolte, M. Will, J. P. Ruske, B. Chichkov, and A. Tuennermann, "Sub-diffraction limited structuring of solid targets with femtosecond laser pulses," *Optics Express,* vol. 7, pp. 41-49, 2000.
[105]. B. C. Stuart, M. D. Feit, A. M. Rubenchik, B. W. Shore, and M. D. Perry, "Laser-Induced Damage in Dielectrics with Nanosecond to Subpicosecond Pulses," *Physical Review Letters,* vol. 74, p. 2248, 1995.

[106]. S. Nolte, C. Momma, H. Jacobs, A. Tünnermann, B. N. Chichkov, B. Wellegehausen, and H. Welling, "Ablation of metals by ultrashort laser pulses," *J. Opt. Soc. Am. B,* vol. 14, pp. 2716–2722, 1997.
[107]. X. Liu, D. Du, and G. Mourou, "Laser ablation and micromachining with ultrashort laser pulses," *Quantum Electronics, IEEE Journal of,* vol. 33, pp. 1706-1716, 1997.
[108]. S. C. Jones, P. Braunlich, R. T. Casper, X. Shen, and P. Kelley, *Opt. Eng,* vol. 28, p. 1039, 1989.
[109]. C. Quoix, G. Grillon, A. Antonetti, J. P. Geindre, P. Audebert, and J. C. Gauthier, "Time-resolved studies of short pulse laser-produced plasmas in silicon dioxide near breakdown threshold," *Eur. Phys. J. AP,* vol. 5, pp. 163-169, 1999.
[110]. L. V. Keldysh, *Zh. Eksp. Teor. Fiz. ,* vol. 47, pp. 1945 [Engl. Trans: *Sov. Phys. - JETP* **20** 1307 (1965)], 1945.
[111]. C. B. Schaffer, A. Brodeur, and E. Mazur, "Laser-induced breakdown and damage in bulk transparent materials induced by tightly focused femtosecond laser pulses," *Measurement Science and Technology,* vol. 12, pp. 1784-1794, 2001.
[112]. C. B. Schaffer, A. Brodeur, and E. Mazur, "Laser-induced breakdown and damage in bulk transparent materials induced by tightly focused femtosecond laser pulses," in *Meas Sci Technol*. vol. 12, 2001, pp. 1784-1794.
[113]. R. W. Boyd, *Nonlinear Optics*, 2 ed. Amsterdam: Academic Press, 2003.
[114]. N. Bloembergen, "Laser-induced electric breakdown in solids," *Quantum Electronics, IEEE Journal of,* vol. 10, pp. 375-386, 1974.
[115]. B. C. Stuart, M. D. Feit, S. Herman, A. M. Rubenchik, B. W. Shore, and M. D. Perry, "Nanosecond-to-femtosecond laser-induced breakdown in dielectrics," *Physical Review B,* vol. 53, pp. 1749-1761, 1996.
[116]. A. Kaiser, B. Rethfeld, M. Vicanek, and G. Simon, "Microscopic processes in dielectrics under irradiation by subpicosecond laser pulses," *Physical Review B,* vol. 61, pp. 11437-11450, 2000.
[117]. M. Sparks, D. L. Mills, R. Warren, T. Holstein, A. A. Maradudin, L. J. Sham, E. Loh Jr, and D. F. King, "Theory of electron-avalanche breakdown in solids," *Physical Review B,* vol. 24, pp. 3519-3536, 1981.
[118]. D. Du, X. Liu, G. Korn, J. Squier, and G. Mourou, "Laser-induced breakdown by impact ionization in SiO2 with pulse widths from 7ns to 150fs," *Appl. Phys. Lett.,* vol. 64, pp. 3071-3073, 1994.
[119]. B. T. V. Vu, O. L. Landen, and A. Szoke, "Time-resolved backside optical probing of picosecond-laser-pulse-produced plasma in solid materials," *Physical Review E,* vol. 47, pp. 2768-2777, 1993.
[120]. X. A. Shen, S. C. Jones, and P. Braunlich, "Laser heating of free electrons in wide-gap optical materials at 1064 nm," *Physical Review Letters,* vol. 62, pp. 2711-2713, 1989.
[121]. M. Bass and H. H. Barrett, "Laser-induced damage probability at 1. 06 and 0. 69 micron(Ruby and Nd-YAG pulsed laser induced surface damage probability comparison at 1. 06 and 0. 69 micron wavelengths by breakdown starting time distribution measurement)," *Applied Optics,* vol. 12, pp. 690-699, 1973.

[122]. C. B. Schaffer, A. Brodeur, J. F. Garcia, and E. Mazur, "Micromachining bulk glass by use of femtosecond laser pulses with nanojoule energy," *Optics Letters,* vol. 26, pp. 93-95, 2001.
[123]. C. B. Schaffer, J. F. García, and E. Mazur, "Bulk heating of transparent materials using a high-repetition-rate femtosecond laser," *Applied Physics A: Materials Science & Processing,* vol. 76, pp. 351-354, Jan 1 2003.
[124]. J. W. Chan, T. Huser, S. Risbud, and D. M. Krol, "Structural changes in fused silica after exposure to focused femtosecond laser pulses," *Optics Letters,* vol. 26, pp. 1726-1728, 2001.
[125]. W. J. Reichman, J. W. Chan, C. W. Smelser, S. J. Mihailov, and D. M. Krol, "Spectroscopic characterization of different femtosecond laser modification regimes in fused silica," *JOSA B,* vol. 24, pp. 1627-1632, 2007.
[126]. W. Reichman, D. M. Krol, L. Shah, F. Yoshino, A. Arai, S. Eaton, and P. Herman, "A spectroscopic comparison of femtosecond-laser-modified fused silica using kilohertz and megahertz laser systems," *J. Appl. Phys.,* vol. 99, p. 123112, Jan 1 2006.
[127]. L. Sudrie, M. Franco, B. Prade, and A. Mysyrowicz, "Study of damage in fused silica induced by ultra-short IR laser pulses," *Optics Communications,* vol. 191, pp. 333-339, 2001.
[128]. E. Bricchi, B. G. Klappauf, and P. G. Kazansky, "Form birefringence and negative index change created by femtosecond direct writing in transparent materials," *Optics Letters,* vol. 29, pp. 119-121, 2004.
[129]. C. Hnatovsky, R. S. Taylor, R. Bhardwaj, E. Simova, D. M. Rayner, and P. B. Corkum, "Long-range periodic planar nanostructures produced in glass by femtosecond laser dielectric modification," *Lasers and Electro-Optics, 2005.(CLEO). Conference on,* vol. 3, 2005.
[130]. V. R. Bhardwaj, E. Simova, P. P. Rajeev, C. Hnatovsky, R. S. Taylor, D. M. Rayner, and P. B. Corkum, "Optically Produced Arrays of Planar Nanostructures inside Fused Silica," *Physical Review Letters,* vol. 96, p. 57404, 2006.
[131]. Q. Sun, F. Liang, R. Vallée, and S. L. Chin, "Nanograting formation on the surface of silica glass by scanning focused femtosecond laser pulses," *Optics Letters, Vol. 33, Issue 22, pp. 2713-2715*.
[132]. G. Miyaji and K. Miyazaki, "Origin of periodicity in nanostructuring on thin film surfaces ablated with femtosecond laser pulses," *Optics Express,* vol. 16, p. 16265, Sep 29 2008.
[133]. A. Royon, "Nonlinear Femtosecond Near Infrarad Laser Structuring in Oxide Glasses," pp. 1-167, Aug 27 2009.
[134]. B. C. Stuart, M. D. Feit, S. Herman, A. M. Rubenchik, B. W. Shore, and M. D. Perry, "Optical ablation by high-power short-pulse lasers," *J. Opt. Soc. Am. B,* vol. 13, pp. 459-468, 1996.
[135]. B. N. Chichkov, C. Momma, S. Nolte, F. von Alvensleben, and A. Tünnermann, "Femtosecond, picosecond and nanosecond laser ablation of solids," *Applied Physics A: Materials Science & Processing,* vol. 63, pp. 109-115, 1996.
[136]. G. Dumitru, V. Romano, H. P. Weber, M. Sentis, and W. Marine, "Femtosecond ablation of ultrahard materials," *Applied Physics A: Materials Science & Processing,* vol. 74, pp. 729-739, 2002.

[137]. M. D. Feit, A. M. Rubenchik, B. M. Kim, L. D. Da Silva, B. C. Stuart, and M. D. Perry, "Physical characterization of ultrashort laser pulse drilling of biological tissue," *COLA97: 4th international conference on laser ablation, Monterey, CA (United States), 21-25 Jul 1997,* 1997.
[138]. F. H. Loesel, J. P. Fischer, M. H. Götz, C. Horvath, T. Juhasz, F. Noack, N. Suhm, and J. F. Bille, "Non-thermal ablation of neural tissue with femtosecond laser pulses," *Applied Physics B: Lasers and Optics,* vol. 66, pp. 121-128, 1998.
[139]. L. Shah, J. Tawney, M. Richardson, and K. Richardson, "Femtosecond laser deep hole drilling of silicate glasses in air," *Appl. Surf. Sci,* vol. 183, pp. 151-164, 2001.
[140]. H. B. Sun, Y. Xu, S. Juodkazis, K. Sun, M. Watanabe, S. Matsuo, H. Misawa, and J. Nishii, "Arbitrary-lattice photonic crystals created by multiphoton microfabrication," *Opt. Lett,* vol. 26, pp. 325-327, 2001.
[141]. W. Watanabe, T. Toma, K. Yamada, J. Nishii, K. Hayashi, and K. Itoh, "Optical seizing and merging of voids in silica glass with infrared femtosecond laser pulses," *Opt. Lett,* vol. 25, p. 1669, 2000.
[142]. M. Takeda, H. Ina, and S. Kobayashi, "Fourier-transform method of fringe-pattern analysis for computer-based topography and interferometry," *J. Opt. Soc. Am.,* vol. 72, pp. 156-160, 1982.
[143]. K. Krishnaswami, B. E. Bernacki, N. Ho^, P. J. Allen, and N. C. Anheier, "Lateral shearing interferometer for measuring photoinduced refractive index change in As[sub 2]S[sub 3]," *Review of Scientific Instruments,* vol. 79, p. 095101, Jan 1 2008.
[144]. R. Vander, S. G. Lipson, and I. Leizerson, "Fourier Fringe Analysis with Improved Spatial Resolution," *Applied Optics,* vol. 42, p. 6830, Jan 1 2003.
[145]. S. Kostianovski, S. G. Lipson, and E. N. Ribak, "Interference microscopy and Fourier fringe analysis applied to measuring the spatial refractive-index distribution," *Applied Optics,* vol. 32, pp. 4744-4750, 1993.
[146]. R. Swanepoel, "Determination of the thickness and optical constants of amorphous silicon," *J. Phys. E: Sci. Instrum.,* vol. 16, p. 1214, Jan 23 1983.
[147]. D. W. Ball, "Theory of Raman Spectroscopy," *Spectroscopy,* vol. 16, pp. 32-34, Oct 24 2001.
[148]. E. S. a. G. Dent, *Modern Raman Spectroscopy: A Practical Approach*: Wiley, 2005.
[149]. B. G. Aitken and C. W. Ponader, "Physical properties and Raman spectroscopy of GeAs sulphide glasses," *Journal of Non-Crystalline Solids,* vol. 256&257, pp. 143-148, 1999.
[150]. D. V. d. Linde and H. Schueler, *J. Opt. Soc. Am. B,* vol. 13, p. 216, 1996.
[151]. C. Lopes, "Evaluation of the photo-induced structural mechanism in Chalcogenide glasses," in *School of Optics* Orlando: University of Central Florida, 2004.
[152]. M. Lenzner, J. Krüger, Z. Cheng, C. Spielmann, G. Mourou, W. Kautek, and F. Krausz, "Femtosecond Optical Breakdown in Dielectrics," *Physical Review Letters,* vol. 80, pp. 4076-4079, 1998.
[153]. K. Tanaka, "Spectral dependence of photoexpansion in As_{2}S_{3} glass," *Philos. Mag. Lett.,* vol. 79, pp. 25-30, 1999.
[154]. T. H. J.W. Chan, S. Risbud, J.S. Hayden, D.M. Krol, "Waveguide fabrication in phosphate glasses using femtosecond laser pulses," *Appl. Phys. Lett.,* vol. 82, pp. 2371-2373, 2003.

[155]. C. Julien, S. Barnier, M. Massot, N. Chbani, X. Cai, A. Loireau-Locac'h, and M. Guittard, "Raman and infraraed spectroscopic studies of Ge-Ga-Ag sulphide glasses," *Materials Science and Engineering B,* vol. 22, pp. 191-200, Jul 16 1994.
[156]. M. Born and E. Wolf, *Principles of Optics*, Seventh (Expanded) ed. Cambridge: Cambridge University, 1999.
[157]. C. Z. Tan and J. Arndt, "The mean polarizability and density of glasses," *Physica B,* vol. 229, pp. 217-224, 1997.
[158]. S. H. Messaddeq, M. S. Li, D. Lezal, S. J. L. Ribeiro, and Y. Massaddeq, "Above bandgap induced photoexpansion and photobleaching in Ga-Ge-S based glasses," *J. Non-Cryst. Solids,* vol. 284, pp. 282-287, 2001.
[159]. R. Swanepoel, "Determination of the thickness and optical constants of amorphous silicon," *J. Phys. E,* vol. 16, pp. 1214-1222, 1983.
[160]. A. Royon, B. Bousquet, L. Canioni, M. Treguer, T. Cardinal, E. Fargin, D.-G. Kim, and S.-H. Park, "Third-Harmonic Generation Microscopy for Material Characterization," *Journal of the Optical Society of Korea,* vol. 10, pp. 188-195, 2006.
[161]. A. Brocas, L. Canioni, and L. Sarger, "Efficient selection of focusing optics in non linear microscopy design through THG analysis," *Optics Express,* vol. 12, pp. 2317-2326, 2004.
[162]. R. Barille, L. Canioni, L. Sarger, and G. Rivoire, "Nonlinearity measurements of thin films by third-harmonic-generation microscopy," *Phys. Rev. E,* vol. 66, p. 067602, Dec 1 2002.
[163]. T. Y. Tsang, "Optical third-harmonic generation at interfaces," *Physical Review A,* vol. 52, pp. 4116-4125, Dec 31 1995.
[164]. L. Petit, N. Carlie, A. Humeau, G. Boudebs, H. Jain, A. C. Miller, and K. Richardson, "Correlation between the nonlinear refractive index and structure of germanium-based chalcogenide glasses," *Mater Res Bull,* vol. 42, pp. 2107-2116, 2007.
[165]. D. Blomer, A. Szameit, F. Dreisow, T. Schreiber, S. Nolte, and A. Tunnermann, "Nonlinear refractive index of fs-laser-written waveguides in fused silica," in *Optics Express*. vol. 14, 2006, pp. 2151-2157.
[166]. K. Tanaka and H. Hisakuni, "Photoinduced phenomena in As2S3 glass under sub-bandgap excitation," *J. Non-Cryst. Solids,* vol. 198-200, pp. 714-718, 1996.
[167]. S. R. Elliott, "A unified model for reversible photostructural effects in chalcogenide glasses," *J. Non-Cryst. Solids,* vol. 81, pp. 71-98, 1986.
[168]. P. Loeffler, T. Schwarz, H. Sautter, and D. Lezal, "Structural changes of GeGaS bulk glasses induced by UV exposure," *J. Non-Cryst. Solids,* vol. 232-234, pp. 526-531, 1998.
[169]. S. H. Messaddeq, V. R. Mastelaro, M. S. Li, M. Tabackniks, D. Lezal, A. Ramos, and Y. Messaddeq, "The infludence of oxygen in the photoexpansion of GaGeS glasses," *Appl. Surf. Sci.,* vol. 205, pp. 143-150, 2003.
[170]. Q. Mei, J. Saienga, J. Schrooten, B. Meyer, and S. W. Martin, "Preparation and characterization of glasses in the Ag_{2}S+B_{2}S_{3}+GeS_{2} system," *J. Non-Cryst. Solids,* vol. 324, pp. 264-276, 2003.
[171]. Q. Zhang, W. Liu, L. Liu, L. Xu, Y. Xu, and G. Chen, "Large and opposite changes of the third-order optical nonlinearities of chalcogenide glasses by femtosecond and continuous-wave laser irradiation," in *Appl Phys Lett*. vol. 91, 2007, pp. -.

[172]. N. Hô, J. M. Laniel, R. Vallee, and A. Villeneuve, "Creation of microchannels in a photosensitive As2S3 slab waveguide," in *J Opt Soc Am B*. vol. 19, 2002, pp. 875-880.
[173]. J. M. Laniel, N. Hô, R. Vallée, and A. Villeneuve, "Nonlinear-refractive-index measurement in As_{2}S_{3} channel waveguides by assymetric self-phase modulation," *Journal of the Optical Society of America B,* vol. 22, p. 437, Jan 22 2005.
[174]. J. Viens, C. Meneghini, A. Villeneuve, T. V. Galstian, E. J. Knystautas, M. Duguay, K. C. Richardson, and T. Cardinal, "Fabrication and Characterization of Integrated Optical Waeguides in Sulfide Chalcogenide Glasses," *Journal of Lightwave Technology,* vol. 17, p. 1184, 1999.
[175]. C. Meneghini and A. Villeneuve, "As2S3 photosensitivity by two-photon absorption: holographic gratings and self-written channel waveguides," *Journal of the Optical Society of America B,* vol. 15, p. 2946, Jan 22 1998.
[176]. C. Lopez, "Evaluation of the Photo-Induced Structural Mechanisms in Chalcogenide Glass," *Ph.D Thesis, College of Optics and Photonics at the University of Central Florida,* 2004.
[177]. T. Anderson, J. Hu, M. Ramme, J. Choi, C. Faris, N. Carlie, A. Agarwal, L. Petit, L. Kimerling, K. Richardson, and M. Richardson, "Integrating optics and micro-fluidic channels using femtosecond laser irradiation," *Proc. of SPIE. Photonics West,* pp. 72030I-72030I-9, Jan 1 2009.
[178]. K. J. Ebeling, *Integrated Optoelectronics*: Springer-Verlag, 1993.
[179]. F. d. Fornel, *Evanescent Waves: from Newtonian Optics to Atomic Optics*: Springer, 2001.
[180]. J. Orava, T. Wagner, M. Krbal, T. Kohoutek, M. Vlcek, and M. FRUMAR, "Selective wet-etching and characterization of chalcogenide thin films in inorganic alkaline solutions," *Journal of Non-Crystalline Solids,* vol. 353, pp. 1441-1445, May 15 2007.
[181]. N. Ponnampalam, R. Decorby, H. Nguyen, P. Dwivedi, C. Haugen, J. Mcmullin, and S. Kasap, "Small core rib waveguides with embedded gratings in As2Se3 glass," *Optics Express,* vol. 12, pp. 6270-6277, 2004.
[182]. A. Kovalskiy, M. Vlcek, H. Jain, A. Fiserova, C. Waits, and M. Dubey, "Development of chalcogenide glass photoresists for gray scale lithography," *Journal of Non-Crystalline Solids,* vol. 352, pp. 589-594, May 15 2006.
[183]. V. Lyubin, M. Klebanov, I. Bar, S. Rosenwaks, N. Eisenberg, and M. Manevich, "Novel effects in inorganic As50Se50 photoresists and their application in micro-optics," *Journal of Vacuum Science and Technology-Section B-Microelectronics Nanometer Structur,* vol. 15, pp. 823-827, 1997.
[184]. A. Stronski, "Application of As40S60$minus;xSex layers for high-efficiency grating production," *Journal of Non-Crystalline Solids,* vol. 266-269, pp. 973-978, May 1 2000.
[185]. R. G. DeCorby, M. M. Pai, H. T. Nguyen, P. K. Dwivedi, T. J. Clement, C. J. Haugen, J. N. McMullin, and S. O. Kasap, "High index contrast waveguides in chalcogenide glass and polymer," *Ieee J Sel Top Quant,* vol. 11, pp. 539-546, 2005.
[186]. M. Veinguer, A. Feigel, B. Sfez, M. Klebanov, and V. Lyubin, "New Application of Inorganic Chalcogenide Photoresists in Lift-off Photolitography," *J. Optoelectron. Adv. Mater,* vol. 5, pp. 1361-1364, 2003.

[187]. R. Dror, B. Sfez, S. Y. Goldin, and A. Cashingad, "Etching of photosensitive chalcogenide glasses:experiments and simulations," *Optics Express,* vol. 15, pp. 12539-12547, 2007.
[188]. M. Vlcek, "Selective etching of chalcogenides and its application for fabrication of diffractive optical elements," *Journal of Non-Crystalline Solids,* vol. 326-327, pp. 515-518, Oct 1 2003.
[189]. S. Kostyukevych, "Applications of chalcogenide glasses and structures on their base in microlithography," *Opto-electronics review,* vol. 6, pp. 273-278, 1998.
[190]. A. Feigel, Z. Kotler, B. Sfez, A. Arsh, M. Klebanov, and V. Lyubin, "Chalcogenide glass-based three-dimensional photonic crystals," *Applied Physics Letters,* vol. 77, p. 3221, Jan 1 2000.
[191]. R. Dror, A. Feigel, M. Veinguer, B. Sfez, and M. Klebanov …, "Submicron sculpturing on chalcogenide films," *Micromachining Technology for Micro-Optics and Nano-Optics ...,* Jan 1 2005.
[192]. J. Orava, T. Wagner, M. Krbal, T. Kohoutek, M. Vlcek, P. Klapetek, and M. FRUMAR, "Selective dissolution of Agx(As0.33S0.67−ySey)100−x chalcogenide thin films," *Journal of Non-Crystalline Solids,* vol. 354, pp. 533-539, Jan 15 2008.
[193]. N. Eisenberg, "New types of microlens arrays for the IR based on inorganic chalcogenide photoresists," *Materials Science in Semiconductor Processing,* vol. 3, pp. 443-448, Oct 1 2000.
[194]. N. Eisenberg, "Fabrication and testing of microlens arrays for the IR based on chalcogenide glassy resists," *Journal of Non-Crystalline Solids,* vol. 198-200, pp. 766-768, May 1 1996.
[195]. N. Eisenberg, M. Manevich, A. Arsh, M. Klebanov, and V. Lyubin, "New micro-optical devices for the IR based on three-component amorphous chalcogenide photoresists," *Journal of Non-Crystalline Solids,* vol. 352, pp. 1632-1636, Jun 15 2006.
[196]. M. Unger, D. Kossakivski, R. Kongovi, J. Beauchamp, J. Baldeschwieler, and D. Palanker, "Etched chalcogenide fibers for near-field infrared scanning microscopy," *Review of Scientific Instruments,* Jan 1 1998.
[197]. J. Gonzalez-Leal, R. Prieto-Alcon, M. Stuchlik, M. Vlcek, S. Elliott, and E. Marquez, "Determination of the surface roughness and refractive index of amorphous As40S60 films deposited by spin coating," *Opt. Mat.,* vol. 27, pp. 147-154, 2004.
[198]. T. Wagner, T. Kohoutek, M. Vlček, M. Vlček, M. Munzar, and M. FRUMAR, "Spin-coated Agx (As0. 33S0. 67) 100− x films: preparation and structure," *Journal of Non-Crystalline Solids,* vol. 326, pp. 165-169, 2003.
[199]. B. Riley, S. Sundaram, B. Johnson, and L. Saraf, "Differential etching of chalcogenides for infrared photonic waveguide structures," *Journal of Non-Crystalline Solids,* vol. 354, pp. 813-816, Feb 1 2008.
[200]. S. Wong, M. Deubel, F. Pérez-Willard, S. John, G. Ozin, M. Wegener, and G. Von Freymann, "Direct Laser Writing of Three- Dimensional Photonic Crystals with a Complete Photonic Bandgap in Chalcogenide Glasses," *Adv. Mater.,* vol. 18, pp. 265-269, Feb 3 2006.

[201]. E. Nicoletti, G. Zhou, B. Jia, M. Ventura, D. Bulla, B. Luther-Davies, and M. Gu, "Observation of multiple higher-order stopgaps from three-dimensional chalcogenide glass photonic crystals," *Optics Letters,* vol. 33, p. 2311, Oct 15 2008.